Université du Québec
Institut national de la recherche scientifique
Énergie Matériaux Télécommunications

Millimeter-wave Frequency Selective Surfaces for Reconfigurable Antenna Applications

Par

Arun Kesavan

Thèse présentée pour l'obtention du grade de
Philosophiae doctor, Ph.D.
en Télécommunications

Jury d'évaluation

Examinateur externe	Prof. Khelifa Hettak Communications Research Centre (CRC), Ottawa
Examinateur externe	Prof. Jean-François Frigon École Polytechnique de Montréal
Examinateur interne	Prof. Serioja O. Tatu INRS-EMT
Directeur de recherche	Prof. Tayeb A. Denidni INRS-EMT

To my family;
Achan,
amma,
thatan,
edathi
and kunjumol.

Acknowledgement

First I would like to express my sincere gratitude to my guide Prof. Tayeb A. Denidni for his continuous encouragement and support throughout my research. I really appreciate his guidance, insights and suggestions on this research.

I would like to express a deep sense of gratitude to family, my father Kesavan P, my mother G Chitra and my siblings Praveen K, Rajalakshmi K and Sreeranjini KS, whom I have dedicated this thesis. I am deeply indebted to their understanding and unforgettable support during my whole career life.

I am very much thankful to my colleagues at Institut national de la recherche scientifique (INRS-EMT), especially Dr. Mohamad Mantash, Dr. Gijo Augustin, Dr. Bybi P Chacko, Dr. Jinxin Li, Dr. Javad Pourahmadzar, Mohammadmahdi Farahani, Reza Karimian, Jamal Zaid, Mehri Borani Kakhki, Dr. Zahid Akthar, Sai Krishna Reddy and Saket Kaushal, for their immense motivations and constructive discussions which have encouraged me to finish my dissertation.

Also, I would like to thank my friends Dr. Vipin Velayudhan, Manesh KN, Lokesh Parapurath, Vinu Narayanan, Karthika K and Ghanshyam Mishra for their support and encouragement.

My sincere gratitude to my mentors and teachers, Prof. Mohanan Pezholil, Dr. Raveendranath U. Nair, Dr. Shiv Narayan, Dr. Mrudula G and Prof. Bratin Ghosh for their support and inspiration in my research career.

Finally, I would express my thanks to Institut national de la recherche scientifique (INRS-EMT) for providing me all the facilities for the completion of my PhD research.

Abstract

In this thesis, I have proposed two new types of millimeter-wave frequency selective surfaces, for shielding and reconfigurable antennas. A novel wideband FSS and a new class of reconfigurable FSS are introduced for shielding as well as mutual coupling reduction in antenna systems and beam-switching applications, respectively. Two beam-switching antennas using cantilever enabled reconfigurable FSS are designed and implemented at the 30 GHz millimeter-wave frequency band.

Initially, a wideband FSS for millimeter-wave applications at the 60 GHz band is investigated. The simulated results of the wideband FSS are validated by the free-space measurement of a fabricated FSS panel. Furthermore, the proposed wideband FSS is applied as a mutual-coupling reducing wall in a MIMO system of DRAs.

As a second objective, a new class of cantilever enabled FSS with frequency reconfigurability is designed. The method of fabrication and measurement of the FSS are described. For the validation of the cantilever-enabled FSS, panels of the proposed FSS are fabricated and measured.

Further, these FSS panels are integrated with a conventional monopole source, to provide a beam-switching antenna in the 30 GHz frequency band. The beam-switching in the azimuth plane of the center source antenna is controlled by the switching of the FSS panels arranged around the antenna. Another antenna using a similar kind of cantilever enabled FSS is demonstrated for dual-plane beam-switching application in the millimeter-wave frequency bands. The FSS panels arranged around the conventional DRA are divided both horizontally and vertically to obtain the concept of dual-plane beam-switching.Further, the prototypes of both single and dual-plane beam-switching antennas at 30 GHz are fabricated and measured to obtain the beam-switching radiation patterns.

Keywords FSS, beam-switching, millimeter-wave, DRA

Contents

List of Figures

List of Abbreviations

FSS	Frequency Selective Surfaces
MIMO	Multiple-input and multiple-output
DRA	Dielectric Resonator Antenna
EBG	Electromagnetic bandgap
EM	Electro Magnetic
TE	Transverse Electric
TM	Transverse Magnetic
RF	Radio Frequency
MEMS	Micro-Electro-Mechanical Systems
PIFA	planar inverted-F antenna
DC	Direct current
EMI	Electro Magnetic shielding
ECC	Envelop correlation coefficient
PMC	Perfect Magnetic conductor
PEC	Perfect Electrical Conductor
SIW	Substrate integrated waveguide
J-cross	Jerusalem cross
PNA	Programmable Network Analyzer
SE	Shielding effectiveness
W/O FSS	with-out frequency selective surfaces
WFSS	with frequency selective surfaces
mm-wave	millimeter-wave
SSF	Structures Sélectives en Fréquence
BIE	Bande interdite électromagnétique
AD	Antenne Diélectrique
J-Croix	Croix de Jérusalem
EB	Efficacité de blindage
CC	Courant continu

λ	Resonant wavelength
ϵ_r	Relative permittivity
S_{21}/S_{12}	Transmission coefficient
λ_g	Guided wavelength
ρ	Envelop correlation coefficient
S_{11}/S_{22}	Reflection coefficient
f_r	Resonant frequency
$epsilon$	Dielectric permittivity
ϕ	Elevation plane angle
θ	Azimuth plane angle

List of Tables

Chapter 1

Introduction

1.1 Motivation

As the advancement in the modern wireless communication systems, devices with diversified functionalities like high-data transmission, polarization or space diversity, multi-band operations, more versatilities and low-cost, confined into an individual unit, are available for our community. Along with the development of the various modern technologies added to the improvement of the quality of the communication systems. The confinement of all the single units makes the intelligent systems more suitable for the military and industrial applications. The intelligent communication systems include the development of both reception modules and processing units. As the antenna system plays an important role in the reception modules, it also get transformed to multi-functional configurations. In this regard, the integration of multiple antenna units provides better performance for the communication systems.

On account of the aforementioned facts, reconfigurable antennas have drawn much interest among the researchers since few decades for multi-functional configurations. Most common properties of this kind of antennas are the reconfigurability in frequency, polarization and radiation pattern, which can render multiple functions, improve the spectral efficiency and reduce channel deteriorations. Many electronical and mechanical approaches are used with these reconfigurable antennas to obtain various features.

In the recent years, millimeter-wave bands have gained much importance. They have the potential to meet the demands of the emerging communication systems and applications. Further, the high-speed, large bandwidth, high-capacity systems and applications, the ease in the integration of compact and high efficient antennas makes this band suitable choice for Gigabit wireless communications, imaging sensors, automotive radars and deep-space communications. However, there are some obstacles in the millimeter-wave technology while deploying it commercially. One is the high attenuation rate due to the path loss since the wavelength at the 60 GHz is the vicinity of 5mm. Attenuation due to the oxygen molecule's absorption is also significant in this frequency band. Due to the compactness of the millimeter-wave array systems, mutual coupling between the radiating elements can affect the antenna performance negatively. The reconfigurable antennas can be used to improve the system characteristics and reduce these issues.

Electromagnetic periodic structures have widely been used with the antennas for a variety of applications due to their typical EM characteristics. They are widely classified into metamaterials, electromagnetic bandgap structures (EBG) and frequency selective structures (FSS), where metamaterials are new materials with unusual electromagnetic properties and EBG and FSS structures are spatial filters for the incident waves. EBG structures work in all polarization angles of the wave incident while the FSS are limited to specific angles only. Furthermore, due to the electromagnetic band-gap property of EBG, it can direct waves through the periodic structures by which they are used for reducing the surface waves of antennas, and also used as a high impedance surface or an artificial magnetic conductor with ground plane for low profile antenna design.

As mentioned above, the frequency selective surfaces, reconfigurable antennas and millimeter-waves motivated us to perform an extensive research on the applications of FSS for millimeter-wave antennas. Accordingly, this thesis aims at the design, fabrication and measurement of novel wide-band FSS for shielding applications and reconfigurable FSS for beam-switching antenna applications. Furthermore, two beam-switching antennas are introduced using the reconfigurable FSS at 30 GHz.

1.2 Problem identification and research objectives

On account of the behavior of spatial filtering of electromagnetic waves incident on the surface, frequency selective surfaces have obtained immense attraction among the researchers in the antenna domain. Subsequently, they are being used in reconfigurable antennas as active surfaces for manipulating antenna beam direction and polarization. In this thesis, a wideband dual layer FSS is introduced for the mutual coupling reduction in millimeter-wave frequency band. Furthermore, a novel kind of reconfigurable FSS using cantilever based switches is designed at 30 GHz frequency band. This FSS is used to convert an omni-directional source to a directional beam-switching antenna. It is important to mention that the active switching structures used can be fabricated at low cost as compared with the expensive active components in the millimeter-wave frequency band.

More specifically, the objectives of this thesis are designing a wideband FSS for mutual coupling reduction in a DRA system and designing reconfigurable FSS using cantilever enabled switches for beam-switching antenna applications at millimeter-wave frequency band. The wideband FSS has achieved shielding effectiveness of above 16 dB and -20 dB isolation DRA MIMO system at 60 GHz frequency. Furthermore, two beam-switching antennas for a single plane and dual-plane operation are designed using cantilever enabled FSS panels at 30 GHz, which are essentially novel beam-switching antennas at millimeter-wave frequency band application.

1.3 Organization of dissertation

In this section of organization, a short summary of each chapter of the thesis is presented. In the foremost Chapter 2, a brief summary and literature survey about the reconfigurable antennas, their types, and applications are performed. Secondly, in Chapter 3, a brief study about FSS, their design concepts and their applications are done.

In Chapter 4, a frequency selective surface (FSS) with wideband frequency response in U- and V-bands is proposed. This FSS consists of a conventional Jerusalem cross and a FAN shape on both sides of a single-layered RO4003 substrate. It exhibits a wide stopband of 30 GHz with attenuation more than 16 dB for the normal incidence. The unit cell is symmetrical in nature, thereby giving similar results for TE and TM operation modes. A panel of this FSS is fabricated and measured using free-space measurement to validate the simulation results. Furthermore, as an application, a wall of proposed FSS is applied in a dielectric resonator antenna (DRA) millimeter-wave (*mm*-wave) multiple-input–multiple-output system for mutual coupling reduction. The results give a low correlation coefficient $< 5e^{-6}$ indicating that the antenna can provide spatial or pattern diversity to increase the data capacity of wireless communication systems at mm-wave bands.

In Chapter 5, the design and concept of active FSS based on cantilever switches are explained. The design and simulation results of the initial designs of the cantilever enabled FSS are discussed. Furthermore, the fabrication process for the proposed FSS and the measurement setups used for the characterization are explained.

In Chapter 6, a beam-switching antenna for millimeter-wave applications at 30 GHz is presented. The radiation reconfigurability for a cylindrical Dielectric Resonator Antenna (DRA) is obtained by using a cantilever enabled frequency selective surface (FSS). The proposed cantilever enabled FSS provides reconfigurable band-pass and band-stop performance with good isolation between them. The investigation of designed FSS is performed using electromagnetic simulation and an array of proposed FSS unit cell is fabricated and measured using the free-space measurement method, which shows a good agreement with the simulation results. Finally, six panels of 1x5 array using the proposed reconfigurable FSS are arranged in a hexagonal configuration around a cylindrical DRA to obtain a reconfigurable radiation pattern in the azimuth plane. A prototype of the proposed radiation reconfigurable DRA is fabricated, and the switching radiation patterns are measured at 30 GHz.

In Chapter 7, a dual-plane beam-sweeping dielectric resonator antenna (DRA) using cantilever enabled frequency selective surfaces (FSS) is presented. The proposed antenna consists of a conventional cylindrical DRA and a hexagonally arranged active FSS operating at 30GHz frequency band. Initially, the reconfigurable FSS using cantilever beams is designed and analyzed. Further, a prototype of the proposed antenna with FSS is designed, fabricated and measured. The beam-sweeping is obtained in both azimuth and elevation planes of the antenna. The whole azimuth plane is covered by the switched beams in six steps of an angle of 60°. In the elevation plane, two steps of angles are obtained at 90° and 30°. The measured antenna gain of 8.1 dB is obtained.

Finally, Chapter 8 concludes the thesis with a summary of the accomplishments and the future work and ideas to be investigated. A detailed summary of the thesis in French is provided in Chapter 9.

1.4 List of Publications

Journals:

1. **Kesavan, Arun**, Karimian, R. and T. A. Denidni. A Novel Wideband Frequency Selective Surface for Millimeter-wave Applications. *IEEE Antennas and Wireless Propagation Letters*, 15:1711–1714, 2016.

2. **Kesavan, Arun**, Mantash, Mohamad, and T. A. Denidni. Beam-switching millimeter-wave antenna using cantilever based frequency selective surfaces. *IET Microwaves, Antennas & Propagation*, 12(13):2019-2024, June 2018.

3. **Kesavan, Arun**, Mantash, Mohamad, and T. A. Denidni. A Dual-plane Beam-sweeping Millimeter-wave antenna using Active frequency selective surfaces. *IEEE Antennas and Wireless Propagation Letters*, 17(10):1832-1836, Aug 2018.

4. **Kesavan, Arun**, Mantash, Mohamad, and T. A. Denidni. Supershaped reconfigurable frequency selective surfaces using cantilever enable switches. *IET Electronics Letters*, Submitted, Jan 2019.

5. **Kesavan, Arun**, Mantash, Mohamad, and T. A. Denidni. Supershaped reconfigurable frequency selective surfaces using cantilever enable switches. *IET Electronics Letters*, Submitted, Jan 2019.

6. Karimian, R. **Kesavan, Arun**, and T. A. Denidni. Low Mutual Coupling 60-GHz MIMO Antenna System with Frequency Selective Surface Wall. *IEEE Antennas and Wireless Propagation Letters*, 16:373-376, 2016.

7. Zaid, Jamal, Abdulhadi, Abdulhadi, **Kesavan, Arun**, Belaizi, Yassin and T. A. Denidni. Multiport Circular Polarized RFID-Tag Antenna for UHF Sensor Applications. *Sensors*, 17(7):1576, 2016.

8. Mantash, Mohamad, **Kesavan, Arun**, and T. A. Denidni. Beam-Tilting End-Fire Antenna Using a Single-Layer FSS for 5G Communication Networks. *IEEE Antennas and Wireless Propagation Letters*, 17(1):29-33, 2018.

9. Mehri Borhani Kakhki, Mantash Mohamad, **Kesavan, Arun**, Muhammad M. Tahseen, and T. A. Denidni. A Millimeter-Wave Beam-Tilting Vivaldi Antenna with Gain Enhancement using Multi-layer FSS. *IEEE Antennas and Wireless Propagation Letters*, Early Access Sep 2018.

10. Mantash, Mohamad, **Kesavan, Arun**, and T. A. Denidni. Millimeter-Wave Antenna with Tilted Beam for Future Base Station applications. *IET Microwaves, Antennas & Propagation*, Early access Oct 2018.

Conference proceedings:

1. **Kesavan, Arun**, Chacko, Bybi P. and Denidni, Tayeb A. Active frequency selective surfaces using cantilever switches for 60-GHz applications. *in Antennas and Propagation and USNC/URSI National Radio Science Meeting, 2015 IEEE International Symposium on*, pages 882–883.

2. **Kesavan, Arun** and Denidni, Tayeb A. Wide stop-band angular stable Frequency Selective Surface for Millimeter-wave applications. *Antenna Technology and Applied Electromagnetics (ANTEM), 2016 17th International Symposium on*, pages 882–883.

3. **Kesavan, Arun**, Chacko, Bybi P. and Denidni, Tayeb A. Beam-tilting Vivaldi antenna using cantilever based-frequency selective surfaces. *In Antennas and Propagation and USNC/URSI National Radio Science Meeting, 2016 IEEE International Symposium on*, pages 961–962.

4. **Kesavan, Arun**, Zaid, Jamal and Denidni, Tayeb A. Wideband FSS superstrate for millimeter-wave antenna gain enhancement. *In Antennas and Propagation and USNC/URSI National Radio Science Meeting, 2017 IEEE International Symposium on*, pages 1073–1074.

5. **Kesavan, Arun**, Mantash Mohamad, Zaid Jamal and Denidni, Tayeb A. Millimeter-wave Dual-plane Beam-switching Antenna based on Cantilever enabled FSS. *In Antennas and Propagation and USNC/URSI National Radio Science Meeting, 2018 IEEE International Symposium on*, pages 293-294.

6. Chacko, Bybi P., **Kesavan, Arun** and Denidni, Tayeb A. Pattern-Reconfigurable Antenna Using Cantilever based-AFSS. *Antenna Technology and Applied Electromagnetics (ANTEM), 2016 17th International Symposium on*, pages 882–883.

7. Zaid, Jamal, Farahani, Mohammadmahdi, **Kesavan, Arun** and Denidni, Tayeb A. Miniaturized microstrip patch antenna using Electromagnetic Band Gap (EBG) structures for multiport passive UHF RFID-tag applications. *in Antennas and Propagation and USNC/URSI National Radio Science Meeting, 2017 IEEE International Symposium on*, pages 2459–2460.

8. Mantash Mohamad, Zaid Jamal, **Kesavan, Arun**, and Denidni, Tayeb A. Wideband Circularly-Polarized 3D Antenna Array for Millimeter-Wave Applications. *in Antennas and Propagation and USNC/URSI National Radio Science Meeting, 2018 IEEE International Symposium on*, pages 601-602.

9. Zaid Jamal, Mantash Mohamad, **Kesavan, Arun**, and Denidni, Tayeb A. Miniaturized Microstrip Patch Antenna Using Magneto-dielectric Substrate for RFID applications. *in Antennas and Propagation and USNC/URSI National Radio Science Meeting, 2018 IEEE International Symposium on*, pages 645-646.

Chapter 2

Reconfigurable antennas

2.1 Introduction

In recent years, due to the demand for inexpensive, reliable, robust, versatile and high-quality communication, there was a rapid development of smart, adaptive and reconfigurable antennas [10, 11]. However, conventional smart antennas such as phased array antennas are bulky, complicated, power consuming and high cost due to their integration of many RF components, feed networks and control systems. In this scenario, smart antennas which are designed by reconfiguring a single element for a particular application, can improve the performance of the communication system efficiently and economically. For instance, by using alternate methods for directing the radiation beam to the desired direction, leads to the elimination of the unwanted noise and saving battery life of the devices. Thus reconfigurable antennas can be used as a key solution from the disadvantages of the conventional antennas and other bulky antenna systems.

In this chapter, a description of some kinds of reconfiguration methods such as the reconfigurability in frequency, polarization and radiation pattern widely used in the literature are explained.

2.2 Reconfigurable antennas

Basically, reconfigurable antennas are termed as those antennas which can alter their basic operating characteristics using some electrical or mechanical assistance. However, the basic radiating element will be the conventional kind of the antenna, but the properties such as current flow, radiation behaviour or electrical characteristics are varied for obtaining desirable outcomes.

2.2.1 Frequency reconfigurability

The frequency reconfigurability is an essential feature in modern communication systems since there are different frequency bands for various functions. In this reconfiguration, the use of multiple antennas for a system can be reduced by using a single unit for different operating frequencies. Thus, the complexity and expense of the overall system can be reduced. Without the deterioration of the basic radiation and the polarization characteristics of the antenna, the reconfigurability in the frequency bands is achieved.

Mostly, the common methods used for the frequency reconfigurability are using mechanical, electrical and by changing the material properties. In the methods using mechanical and electrical switches, the variation of the frequency is continuous, but in the other methods like changing the material properties and mechanically changing the structure, the variation of the frequency can be obtained continuously over a wide frequency band.

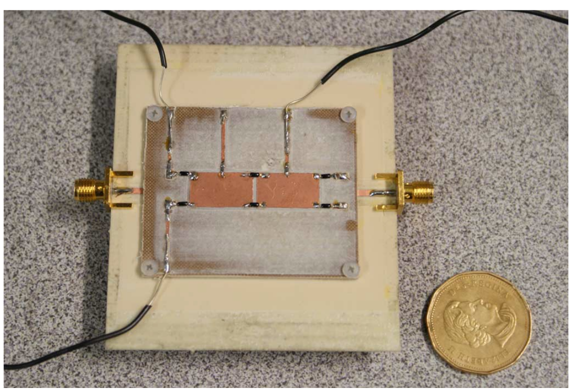

(a)

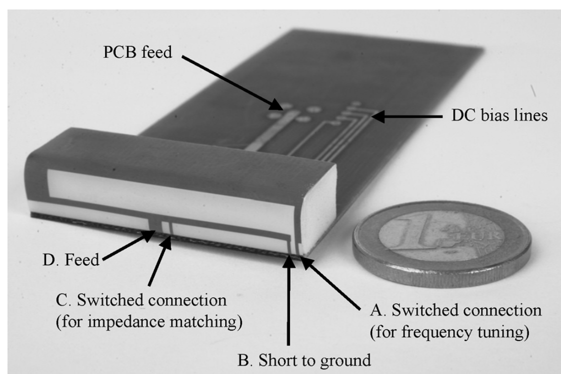

(b)

Figure 2.1 – Frequency reconfigurable antennas (a) Varactor diode enabled [1] (b) RF-MEMS enabled [2]

Using movable radiators with electromagnetic actuators such as piezoelectric actuators or micro-machined plastic deformations [12] come under the mechanical methods of frequency reconfigurability. Even though these methods provide a wide range of frequency and low loss, these switches are bulky and have low switching speed. The electrical switches such as PIN diodes, varactor diodes, optical switches, radio frequency micro-electro-mechanical systems switches(RF-MEMS) are some of the commonly used ones for the antenna applications. Better switching speed as compared with the mechanical switches makes these switches more advantageous. A differentially fed microstrip antenna with frequency tuning capability has been presented in [1] where varactor diodes have been utilized to tune the operational band (see Figure 2.1 (a)). A capacitive MEMS loaded PIFA antenna (see Figure 2.1 (b)) is capable of operating over a bandwidth of more than one octave while improving the performance in terms of specific absorption rate. Furthermore, in the method of changing material properties liquid crystals, ferromagnetic and ferroelectric materials are used, whereby applying DC voltage or magnetic field, the electrical properties are changed to achieve the reconfigurability.

2.2.2 Polarization reconfigurability

To reduce the interference of the signals, and to enhance the antenna link quality and to mitigate the polarization mismatch losses in various portable devices, the polarization reconfigurability can be an excellent choice. Usually, switching between the different polarization modes such as horizontal, vertical and circular polarization is performed in this reconfiguration. Since the current distribution on the antenna determines the polarization modes, the switches such as PIN diodes and RF-MEMS are used for controlling the current flow without deteriorating the radiation pattern and impedance match of the antenna. A ring slot patch antenna, as shown in Figure 2.2, using eight PIN diodes for frequency and polarization reconfigurability is proposed in [3].

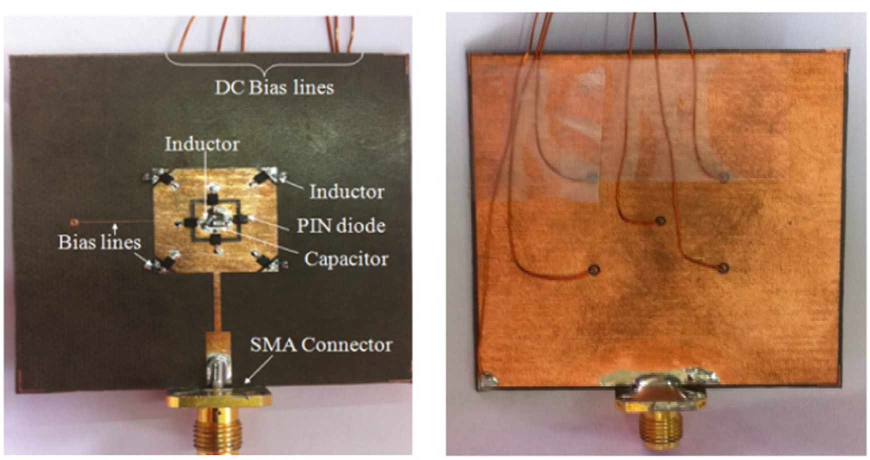

(a) (b)

Figure 2.2 – Frequency and polarization reconfigurable antenna [3]

2.2.3 Radiation pattern reconfigurability

The radiation pattern reconfigurability of the antenna is performed for the enhancement of link quality by directing the radiated beam to desired directions. Mostly, it is achieved by spatial filtering or changing the electric or magnetic currents on the radiating elements. To keep the impedance matching and the gain of the antenna to be in control is the great challenge in this reconfiguration. The active switches like PIN diodes and RF-MEMS are used to change the current distribution for radiation beam sweeping. Similarly, in phased array antennas, the radiation beam sweeping is performed using a controlled feed network with variable phase control. However, these methods have a lot of loss due to the use of phase shifters.

Another common method is the use of active parasitic elements for the spatial filtering of the radiated beams for the pattern reconfiguration. The theory behind this method takes back to the radiation mechanism of an N-port antenna system by reacting loading principle mentioned by R. F. Harrington. By using reconfigurable switched parasitic impedance elements around a central source radiator at a distance of $\lambda/4$, obtained a diverse pattern in [13].

With the development of engineered EM materials such as metamaterials, EBG structures and FSS have been used for the radiation pattern-sweeping applications. FSS as a periodic structure, when excited with a uniform plane wave, it acts as a bandpass or band-reject spacial filter according to its configuration. When incorporated with active components such as pin diodes [14, 15, 16, 17, 18], varactor diodes [4] and MEMS switches [19, 20], its resonance properties can be varied and has been used in beam-switching applications. Similar FSS screens have been used as cylindrically shaped partially reflective surface around omnidirectional source antenna for radiation beam-switching [14, 15, 16, 21]. A nimble radiation pattern structure and a wideband sweeping beam antenna using a hybrid structure have been described in [15] and [14], respectively. A cylindrical slot FSS has been used in [22] to obtain a better continuous sweeping of beam in the azimuth plane. The FSS panel has been made into sectoral shapes around a source antenna for beam-switching [17, 4, 23]. The high-gain sectoral antenna has been proposed in [17], where metal sheet guided structures has been used in front of the reconfigurable FSS screens. In [4], a ten-sided sectoral antenna (see Figure 2.3(a)) has been proposed, where single and dual-beam modes of radiation pattern switching has been achieved using FSS panels with varactor diodes as the active element. A hexagonal parasitic layer based reconfigurable antenna using PIN diodes (see Figure

2.3(b)) for 5G communications has been proposed in [5]. Recently, dual-band beam-switching antennas using pin diode enabled FSS screen have been proposed in [24, 25]. Moreover, for the high gain beam-switching, some works with metal sheet guided structures in front of the reconfigurable FSS screens have also been proposed [16, 26].

Along with the azimuth plane beam-switching, the beam-tilting in the elevation plane has also been suggested for the base station antennas. Some research contributions in beam-tilting can be found in the literature which includes beam-tilting using periodic surfaces such as EBG [27], metamaterials [28] and FSS [29]. A dipole array mounted on customized EBG for the enhanced down-tilt beam is proposed in [27]. Furthermore, mu-near-zero metamaterial slabs integrated with the dipole antenna to obtain E-plane beam-tilting with enhancement of gain at millimeter-wave bands has been proposed in [28]. Recently, a work has been reported for the elevation plane beam-switching, where a two-port feed array used as a source in [30].

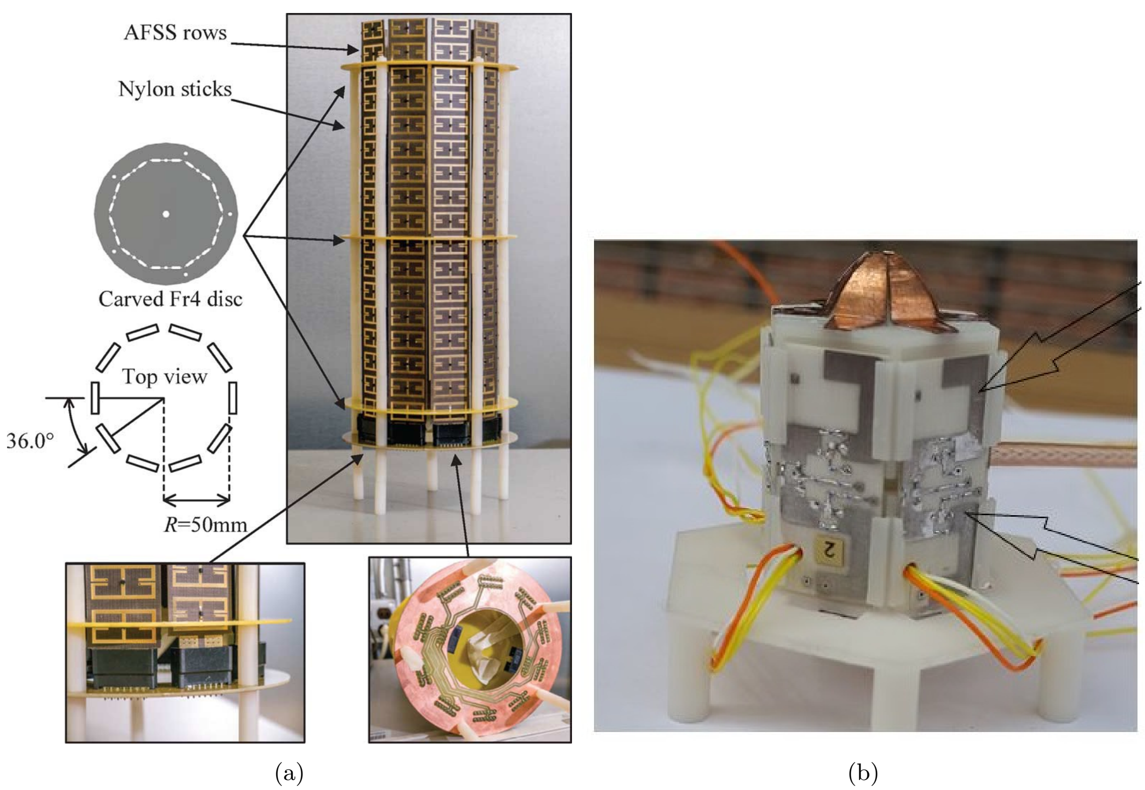

Figure 2.3 – Radiation reconfigurable antenna using active FSS (a) Varactor diode enabled [4] (b) PIN-diode enabled[5]

2.3 Conclusion

This chapter has presented a survey of research works about reconfiguration methods for the better performance of the antenna system. However, a few works have been reported in the millimeter-wave reconfigurable antennas. This proves that more studies have to be performed on the current methods of reconfiguration of antennas for the implementation in millimeter-wave frequency band.

Chapter 3

Frequency Selective Surfaces

3.1 Introduction

The history of frequency selective surfaces takes back to the 60's, where they have been extremely used in the military applications. In the development of FSS, they have been considered to be as dichroic surfaces used as spectral filters. Even though the initial sample of the FSS has been formulated by Marconi and Franklin in 1919, the further intense theoretical and experimental investigations of FSS have been reported after 1960s due to the high demand for military applications.

3.2 Frequency Selective Surfaces

Basically, frequency selective surfaces are termed as spatial filters in both two and three dimensionally. The 2D structures are infinite periodic-structures of metal patches or aperture etched on a metal sheet, while the 3D FSS are volumetric structures arranged periodically using some fixtures [6]. Mostly these structures are used for the either transmit or reflect EM waves in a particular band of frequency. The array of metal patches or structures acts as a band-stop filter for the EM waves while the apertures structures being the inversion of the patches, passes the EM waves for a specific band. Furthermore, the phase and polarization modes of the EM waves are also affected by the FSS shapes. The 3D FSS has better polarization variation compared with that of the planar FSS, due to which the former is more suitable for the polarizer application. Depending upon the application and the system requirements, FSS are widely designed by varying different parameters for the extended frequency bands from microwave to millimeter-wave till infrared where FSS screens are fabricated using micro-machining techniques [31].

3.2.1 Design parameters for FSS

For different applications, FSSs are designed as a narrow or wideband, or multiple resonances, or polarization independent. The main parameters of the FSS are the resonant structure shape and the lattice pattern, which directly depends on the wavelength of the center frequency and the bandwidth of the response [6, 32]. The arrangement of FSS lattice such as tetrahedral or hexahedral and period of unit-cell can effect the onset of grating lobes. The dielectric substrate supporting the FSS, the number of FSS layers and the spacing of these layers can affect the bandwidth of the response [32, 33].

The unit-cell type determines the resonance frequency, polarization, bandwidth and incidence angle of the FSS. Basically, slot type elements are used for the bandpass response and patch type elements are used for the band stop operations. Some of the shapes are more independent of polarization effects and wide bandwidth, while some have a narrow bandwidth and more polarization dependent. Similarly, some loop structures can make the size of the unit-cell more miniaturized. Thus, the shape of the element is chosen wisely depending on different applications.

The classification of the FSS based on the element shapes are center connected, loop structures, solid interior and hybrid elements (see Figure 3.1) [6]. Simple straight dipole, three-legged tripole, anchor shaped, square spiral and Jerusalem cross come under the first group of center connected type. Element size for this type is half of the resonant wavelength and can be packed tightly with enhanced bandwidth and higher onset of grating lobes. In the second group, the loop type elements have better resistant for the oblique incidence of the waves. The common loop shapes are three-legged, four-legged, circular, hexagonal shaped. Compact size and the broad range of bandwidth variation are the advantages of this group elements. The third group of solid structures are intended for specific applications with high sensitivity to the oblique incidence and onset of grating lobes. The fourth hybrid group is having a combination of the other groups, which can combine specific characteristic of each for a desired response. Thus the shape of the element determines the overall response of the FSS and have a crucial role in the design of FSS structures [6].

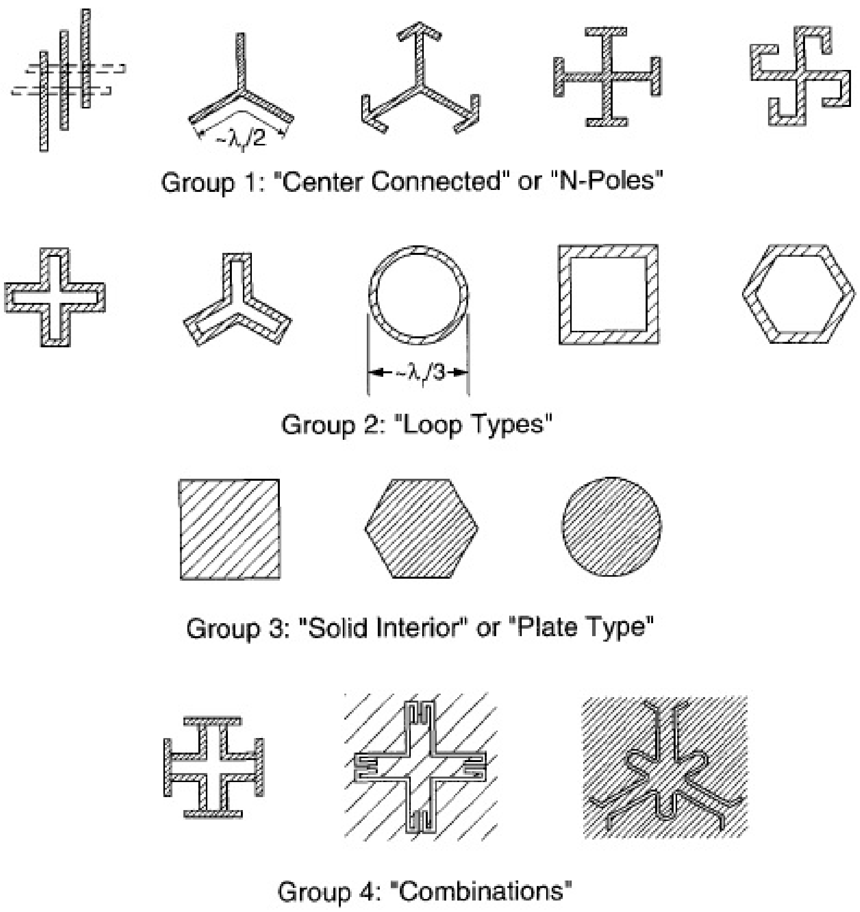

Figure 3.1 – Different groups of FSS element [6].

Usually, FSSs are fabricated on dielectric cladding printed circuit boards. Even though the dielectric gives supports for the FSS, but also they contribute for the flatness of bandwidth, roll-off rate and incident angle performance. The frequency response of an FSS embedded with dielectric cladding is decreased by a rate of $1/\sqrt{\epsilon_r}$, where ϵ_r is the relative permittivity of the dielectric substrate. Furthermore, the thickness of the dielectric substrate contributes to the angular stability and the polarization of the resonant FSS. To obtain broad-band flat response with rapid roll-off rate, the thickness of the dielectric is controlled. For better wideband performance, multiple layers of FSSs with dielectric cladding are used [6, 34].

The transmission/reflection responses of the FSS can be affected by its lattice pattern. Depending upon the distance between the elements and the geometrical position elements, the resonant frequency, bandwidth, and the angular stability are varied. Furthermore, the onset of grating lobes are determined by this geometrical lattices such as rectangular, skewed, square and equilateral triangular [6].

3.2.2 Applications of FSS

As the traditional applications of FSS are concerned, the most common are radomes, band-stop filters, dichroic reflectors, absorbers and polarizers [6]. In the design of vehicles with small radar cross sections, high RCS level of large antennas is an issue. The radomes with FSS can be a good solution for the reduction of RCS. The FSS radomes which are in-band transparent and reflective in the out-band are used to reduce RCS. FSSs are used as sub-reflectors in multi-band reflector antennas, where sub-reflectors are used to reflect one band and pass another; to cover different frequencies by multiple feeds placed at different places .

FSS with multiple layers can be placed in-front of a perfect electric layer for absorbing applications like stealth or electromagnetic shielding [35]. For shielding application, the works reported with single [36], double [37] and wide [38] frequency bands, where the polarization independence is the inevitable characteristics for FSS screens. Further, FSS can transform the polarization of an incident wave, by changing the phase of the horizontal and vertical wave components. The gain of the antenna can be increased by multi-layered FSS used as Fabry Pérot cavity along with a conventional patch antenna. Dual-band [39], wideband [40] and circular polarized [41] Fabry Pérot cavity antennas using FSS layers have been published in literature. Recently, the development of three-dimensional elements has been reported. These structures allow a better control of electric and magnetic currents compared with the planar FSS. They are less sensitive to the angle of incidence and having higher bandwidth [8, 42].

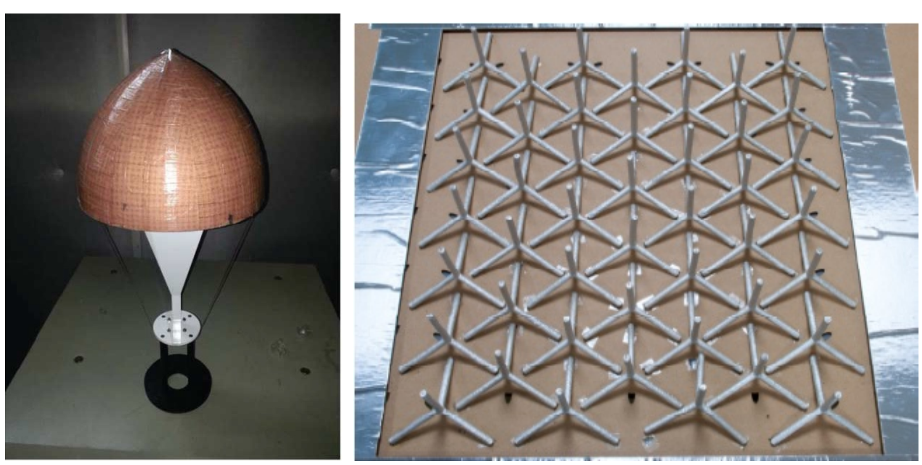

(a) (b)

Figure 3.2 – Application of FSS (a) Radome with FSS [7] (b) 3D calthrop array FSS [8]

3.3 Conclusion

In this chapter, a research survey of the basics of FSS and their applications has been performed. It should be noted that for the design and implementation of FSS for specific applications, a thorough investigation in theoretical and experimental are required. By the development of new technologies, FSS structures have immense applications yet to be explored in wide range of frequencies.

Chapter 4

mm-wave Wideband Frequency Selective Surface

4.1 Introduction

FSS structures are a 2-D or 3-D array of periodic elements that provide transmission or reflection characteristics depending on their element type. In modern wireless communications, frequency selective surfaces have widely been used in spatial filters, absorbers, radomes, and antennas in the microwave and millimeter-wave ranges [6].

Recently electromagnetic interference (EMI) shielding has extensively been examined. Electromagnetic (EM) bandgap structures [43], metamaterials [44], and FSS [45][46][47] have widely been used as shielding surfaces. Because of the ease of fabrication and the low profile nature, FSS has become the most suitable candidate for shielding. A single-layer FSS for ultrawideband shielding has been reported with 7.5GHz bandwidth [45]. The most of the work is focused on the lower frequency EM shielding. The millimeter waves have been increasingly important in the field of wireless communications, radar, remote sensing technology, and radio astronomy. However, few works have been reported in the millimeter-wave shielding. In [48], a carbon nanotube macrofilm operating at 40–60 GHz was used for millimeter-wave shielding.

Mostly, FSSs are designed for narrowband frequencies. Due to the improvement in technologies of wideband radomes and satellite communications, the demand for dual and wideband FSS have been increased. In [47], a wideband FSS using cantor dust fractal geometry has been designed with the angular and polarization-independent operation for UWB application. Indeed, some works with FSS having dual band have been noticed in [49] and [50]. In [50], a dual-band metamaterial FSS operating in V- and W-bands has been designed for radome applications with excellent transmission efficiency and wide incident angle stability. Recently, many wideband FSS structures have been proposed in the literature, using this technique of cascading of double layers. An equivalent circuit model-based the method for synthesizing band stop FSS and a wideband FSS having two square-loop arrays have been proposed in [51]. Furthermore, a wideband FSS for aircraft stealth designs with 110% bandwidth and high angular stability till 60° of oblique incidence [35], a cascaded dual-layer patch FSS reflector for 4G/X-Band/Ku-Band with 100% bandwidth [52] and a tunable broadband FSS for electromagnetic shielding using metasurfaces and plasma media with 181% bandwidth [53] have also been proposed in the literature.

In this chapter, a single-layered wideband FSS is proposed. It has a wide bandwidth of 30 GHz(from 40 to 70 GHz) and a fractional bandwidth of 54.5% with respect to the center frequency (55 GHz). The proposed structure has a wide bandwidth and the unit cell size is having a miniaturized size of ($0.34\lambda \times 0.34\lambda$). By changing the parameters of the FSS, the bandwidth and the resonance frequencies can be controlled. A panel of 40×40 unit cells was fabricated, and the results were compared with the simulation results. This FSS can be used as an effective shielding device and mutual coupling reduction element in the U- and V-band regions of the millimeter-wave frequencies.

4.2 FSS Design And Principle

Figure. 4.1 shows the single-layered geometry of the FSS unit cell with the conventional Jerusalem cross (J-cross) and the FAN shape etched on both sides of the RO4003 substrate. The periodicity of the unit cell is 1.9 mm in both x- and y-directions. The thickness of the Rogers substrate used is 0.508 mm, and its dielectric constant is 3.55 with a loss tangent of 0.0027. The J-cross and FAN shape consist of rectangular strips of width 0.5 and 0.2 mm, respectively. Each arm of the J-cross has a length of 0.623 mm and end with a perpendicular arm of 0.75 mm length. The loop radius and the arm length of the FAN shape are 0.375 mm and 1.325 mm, respectively.

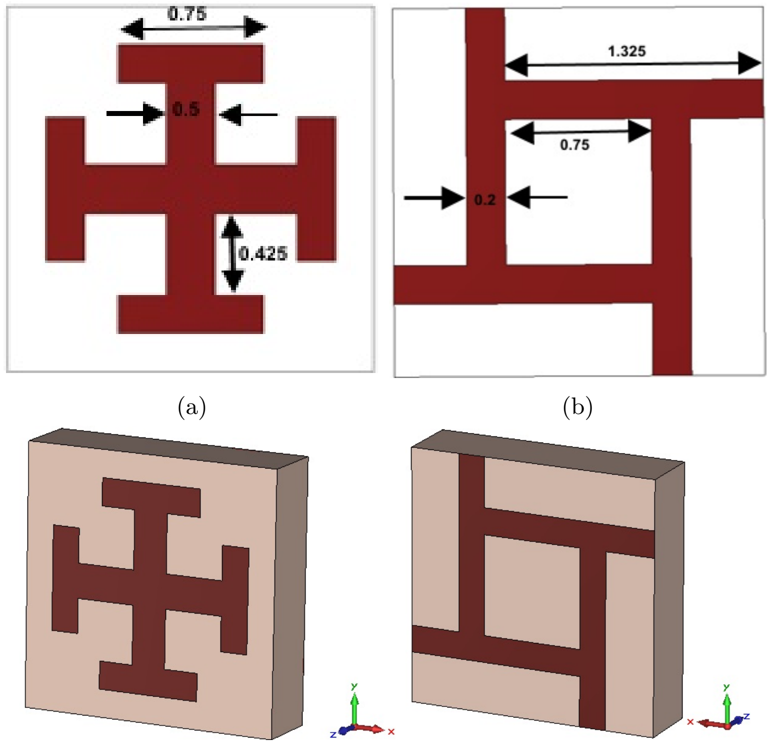

(a) (b)

(c) (d)

Figure 4.1 – (a) J-cross on the top surface. (b) FAN shape on the bottom surface. Perspective views of the unit cell (c) front and (d) back (dimensions in mm).

The FAN shape and J-cross are designed to resonate at the higher and lower frequencies, respectively, which are combined to form the wide stopband of the proposed FSS. The J-cross structure provides a miniaturized structure for the FSS and the FAN shape, which can be considered as a loaded loop provides a good bandwidth, and its resonance frequency can be tuned by adjusting loads and the loop radius [54].

4.3 Simulation results and Discussion

In the initial stage, the single-layered FSS unit cell was simulated using CST Microwave Studio [55] to obtain the transmission and reflection plots, as shown in Figures. 4.2-4.6. The J-cross resonates at the frequency of 48 GHz, and the FAN shape resonates at 60 GHz, when each of these structures is simulated alone. It is clearly shown in Figure. 4.2 how both of the FSS structure resonances

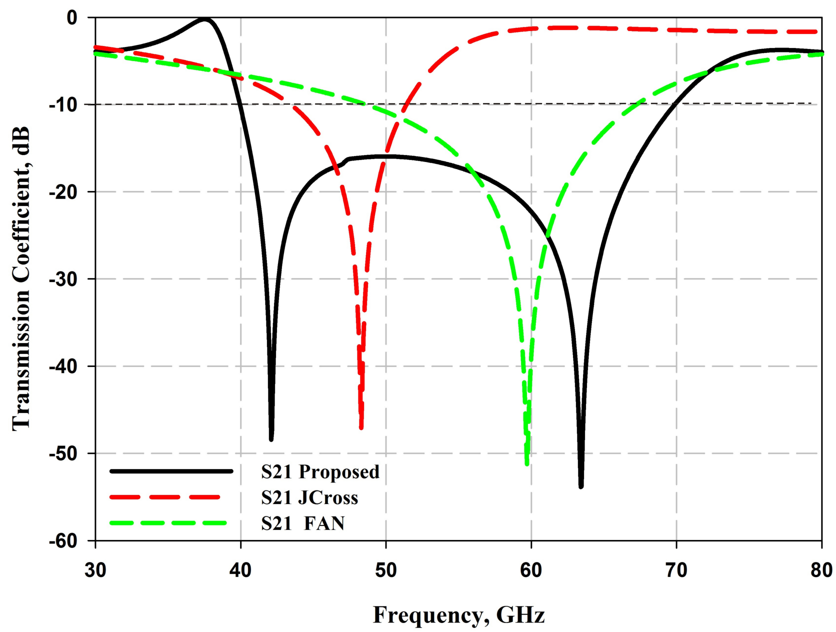

Figure 4.2 – Comparison of transmission coefficients of J-cross and FAN shape with the proposed FSS.

are combined to form a wide bandwidth at 30 GHz in the band of 40–70 GHz. The resonances of each FSS structure shift slightly when both are combined, and it is because of the mutual coupling between them. The phase and magnitude plots of transmission and reflection coefficients of the FSS are shown in Figure. 4.3.

Figure. 4.4 shows the surface current distribution on the proposed wideband FSS structure for different frequencies when a plane-wave is incident on it. In the higher and lower frequencies that are out of the stopband, the current distribution shows lesser values [see Figure. 4.4(a) and (d)], but in the resonance frequencies of the J-cross and FAN shape, the plot shows the contributions of each structure, respectively [see Figure. 4.4 (b) and (c)].

A parametric analysis was carried out by varying the dimensions of FSS unit cell to obtain a well optimized result. The dimensions affecting the wide bandwidth and the resonance frequency of the unit cell were analyzed. Figures. 4.5 and 4.6 show the parametric analysis of the FSS unit cell. It is observed that the loop radius of the FAN shape can affect the wide bandwidth of the unit cell. As the loop radius is changed from 0.4 to 0.25 mm, the bandwidth gets lowered from 56.75% to 44%. This is because of the decrease in the coupling effect between the FAN shape and J-cross. Indeed, the resonance frequency of the unit cell can be tuned using the arm length of the J-cross.

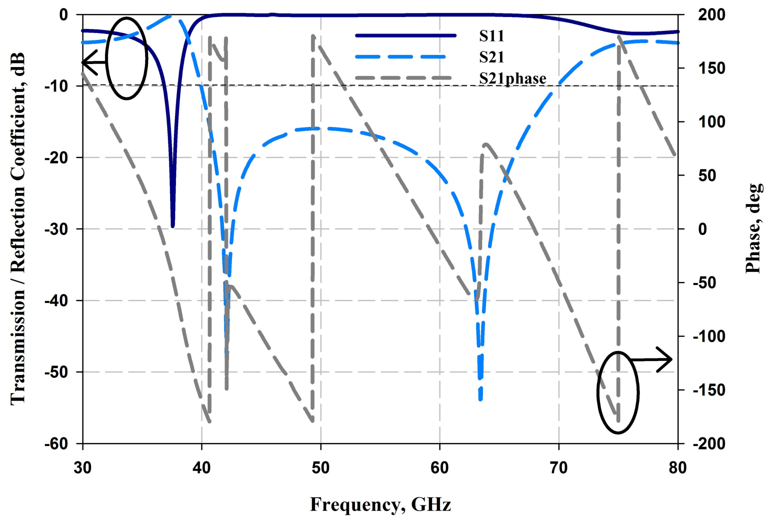

Figure 4.3 – Magnitude and phase plots of S_{11} and S_{21}

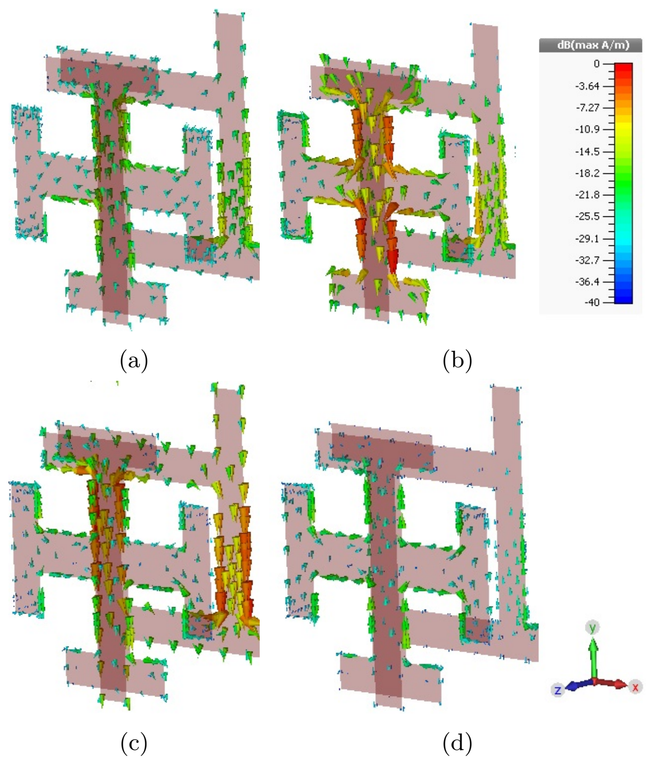

Figure 4.4 – Surface current distribution on the proposed FSS structure at (a) 35 GHz, (b) 42.1 GHz, (c) 63.2 GHz, and (d) 75 GHz.

The wide band of resonance shifts toward the lower frequency as the arm length of the J-cross is increased.

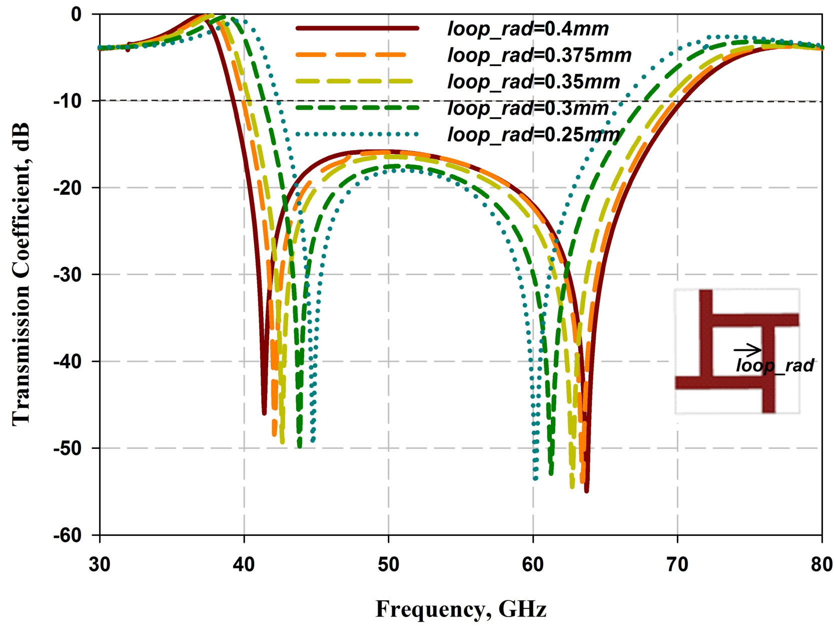

Figure 4.5 – Comparison of transmission coefficients of unit cell for different loop radius of FAN shape.

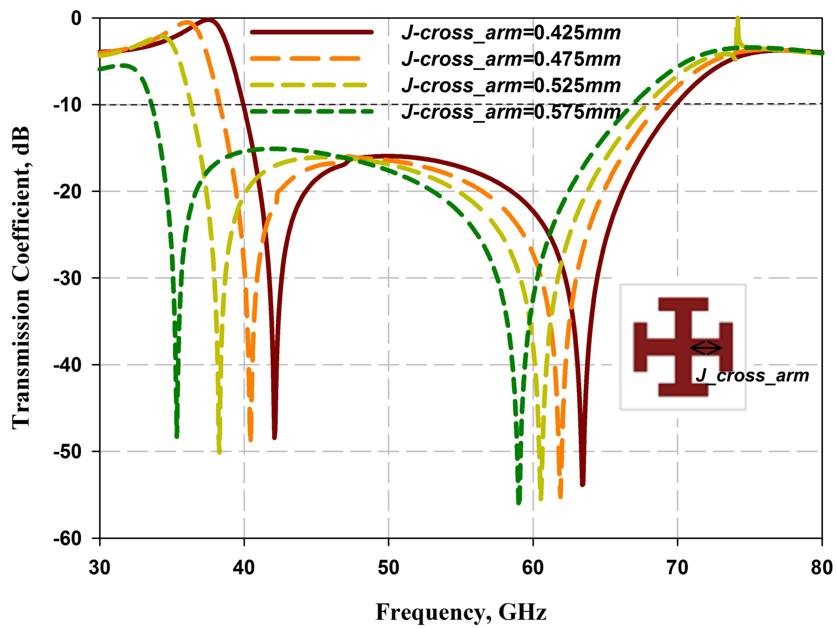

Figure 4.6 – Comparison of transmission coefficients of unit cell for different arm lengths of J-cross.

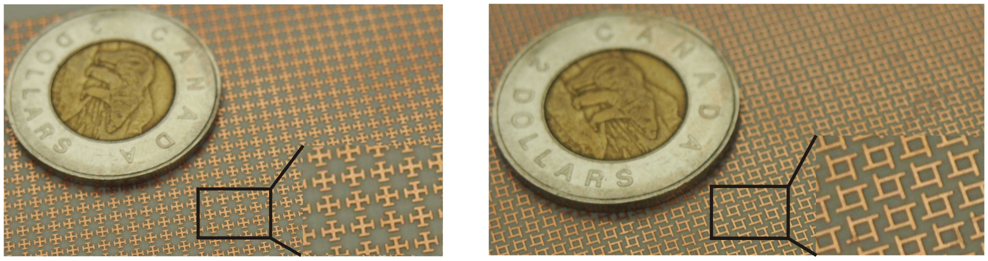

(a) (b)

Figure 4.7 – Fabricated prototype of FSS with zoomed view given as inset (a) Jerusalem cross on the top surface. (b) FAN shape on the bottom surface.

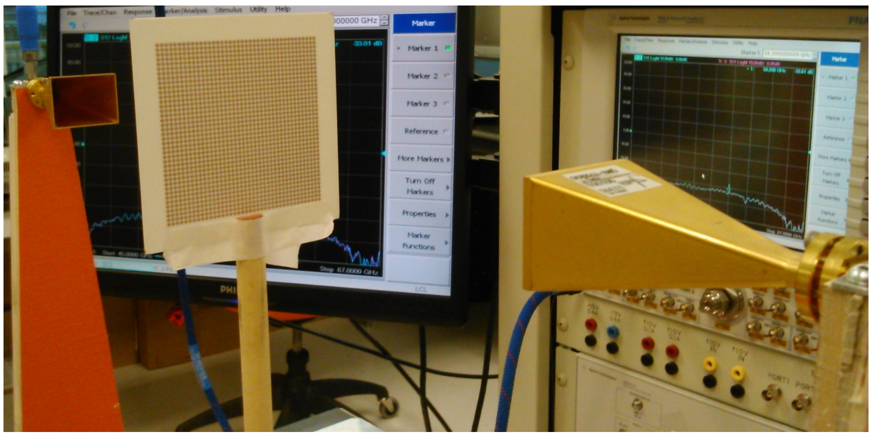

Figure 4.8 – Free-space measurement setup for the FSS measurement.

4.4 Experimental setup and results

To validate the simulated results, the proposed FSS was fabricated on the RO4003 panel of 95×95 mm^2 dimensions. The prototype of the fabricated FSS is shown in the Figure. 4.7. About 40 unit cells are arranged in xy-plane to form an FSS panel. The free-space measurement setup is used to obtain the transmission characteristics of the FSS. Because of the non-availability of standard antenna working in this large frequency bandwidth of 30–80 GHz, two symmetrical pyramidal horn antennas operating in the frequency band of V-band with 24 dBi gain are used in the measurement setup. As shown in Figure. 4.8, the FSS panel is placed between the horn antennas using a prototype holder. A network analyzer, Agilent technologies PNA N5247A with 10 MHz to 67 GHz frequency range, is used. The transmission characteristics without the FSS panel are measured at the beginning for obtaining the calibrated results. Using a mechanical rotation system, the prototype is rotated in various incident angles for the measurement of TE and TM modes.

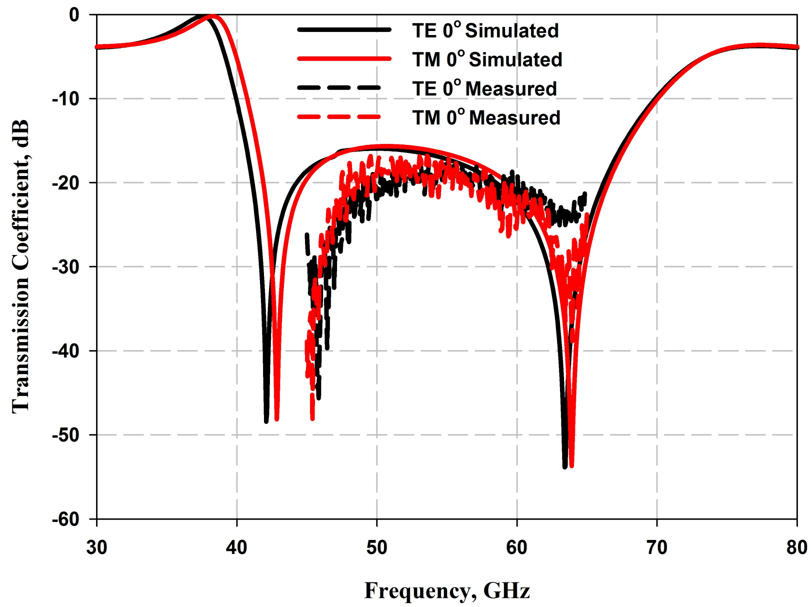

Figure 4.9 – Comparison of transmission coefficients of simulated and measured results for TE and TM modes with normal incidence.

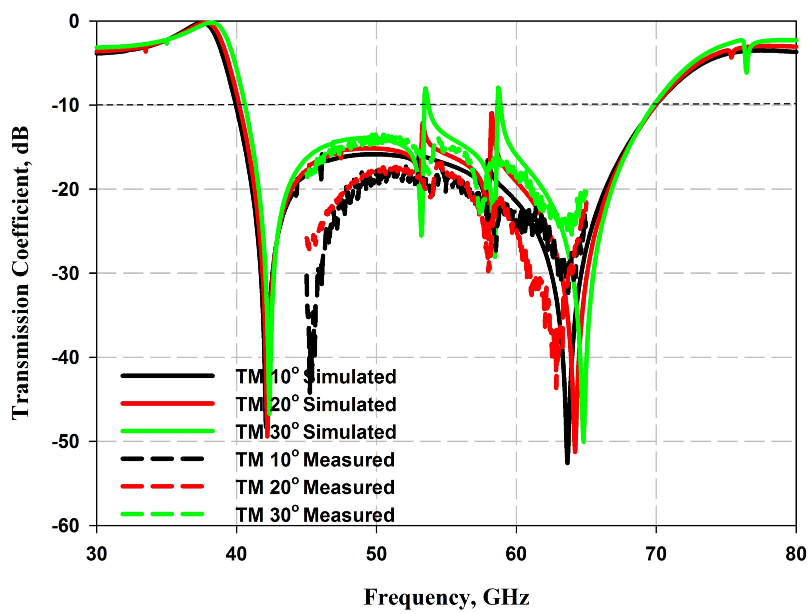

Figure 4.10 – Comparison of transmission coefficients of simulated and measured results for TM mode with oblique incidence.

The transmission coefficients of the prototype for both normal and oblique incidence are measured using the free-space measurement setup. The comparisons between simulated and measured

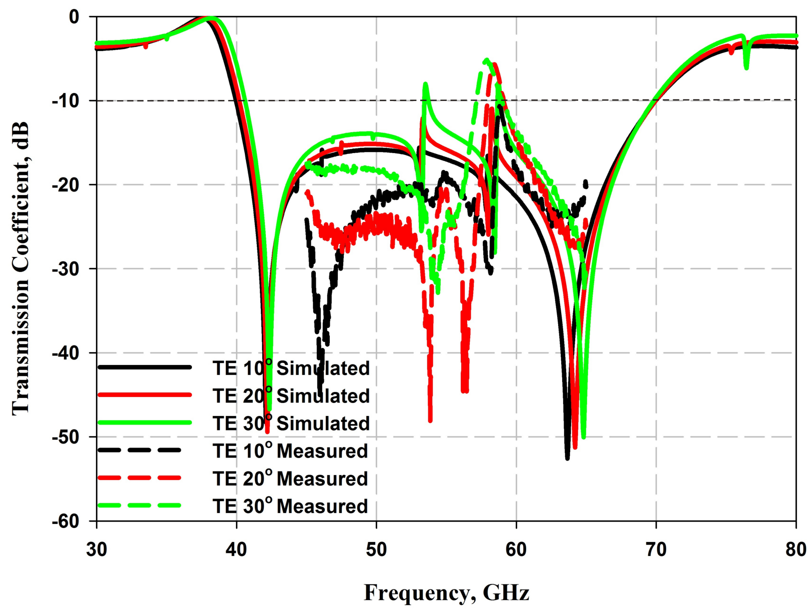

Figure 4.11 – Comparison of transmission coefficients of simulated and measured results for TE mode with oblique incidence.

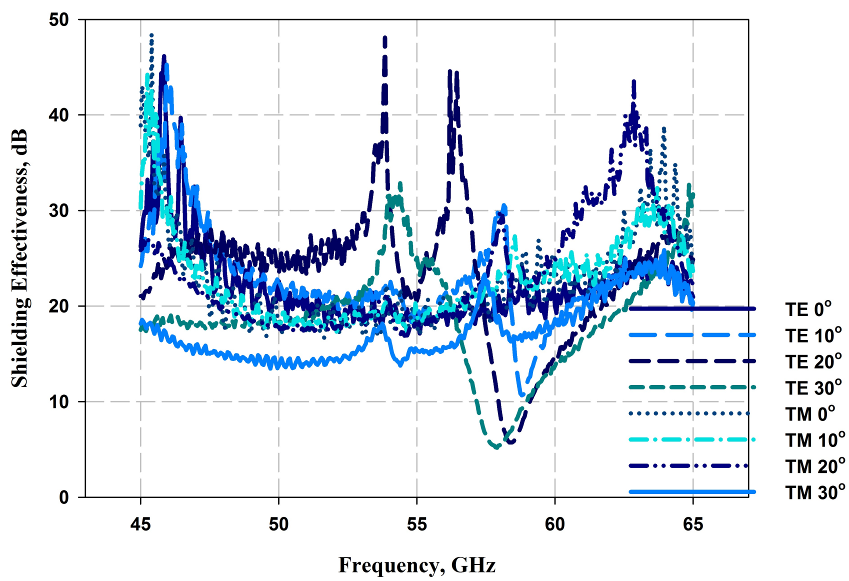

Figure 4.12 – Measured SE for both TE and TM modes with various incidence angles.

results for both TE and TM polarizations in different angles are plotted in Figures. 4.9- 4.11. It is evident from the comparisons that the measured results are in good agreement with the simulated ones. The slight variations of the resonance frequencies are due to the edge reflections and scattering of EM waves during the measurement. As the incidence angle changes, the wide bandwidth is affected a little due to the generation of grating lobes. These grating lobes can be reduced by the decreasing the loading of the FAN shape, but it reduces the attenuation in the whole frequency band.

The shielding effectiveness (SE) is defined as the ratio of the magnitude of the incident electric field on the surface and the transmitted electric field through the surface. Since the incident field is greater than the field exits from the surface, the value of the SE is always positive [56]. Using the S-parameter values obtained from the measurement, the SE can be calculated given as [57]

$$SE_{dB} = S_{21,\ without\ FSS} - S_{21,\ with\ FSS} \tag{4.1}$$

where $S_{21,\ without\ FSS}$ is the transmission coefficient of the antenna without the FSS and the $S_{21,\ with\ FSS}$ is the transmission coefficient with FSS. The measured SE for the TE and TM mode for various incidence angles is given in Figure. 4.12. It is found that high SE has been achieved for all incidence angles, but the bandwidth has been reduced for the oblique incidence angles due to grating lobes and fringing fields.

4.5 Application of proposed FSS as mutual coupling reduction wall

As an application, the proposed FSS wall has been inserted between two DRAs to reduce the mutual coupling due to free space radiation. To reduce the surface current between two antennas, two slots with different size acting as an LC resonator have been etched from the common ground plane of the structure. A parametric study has been done to explain the effect of the two slots. A prototype of the structure was fabricated and measured. The isolation better than -30 dB has been achieved by using FSS wall and slots. An envelope correlation coefficient better than 5e-6 and high efficiency makes this antenna a good candidate for MIMO system application at millimeter-wave frequencies.

4.6 Conclusion

In this chapter, a novel wide stopband FSS resonating at 40–70 GHz has been presented. The single-layered miniaturized geometry and wide stopband nature are the advantages of this FSS. It

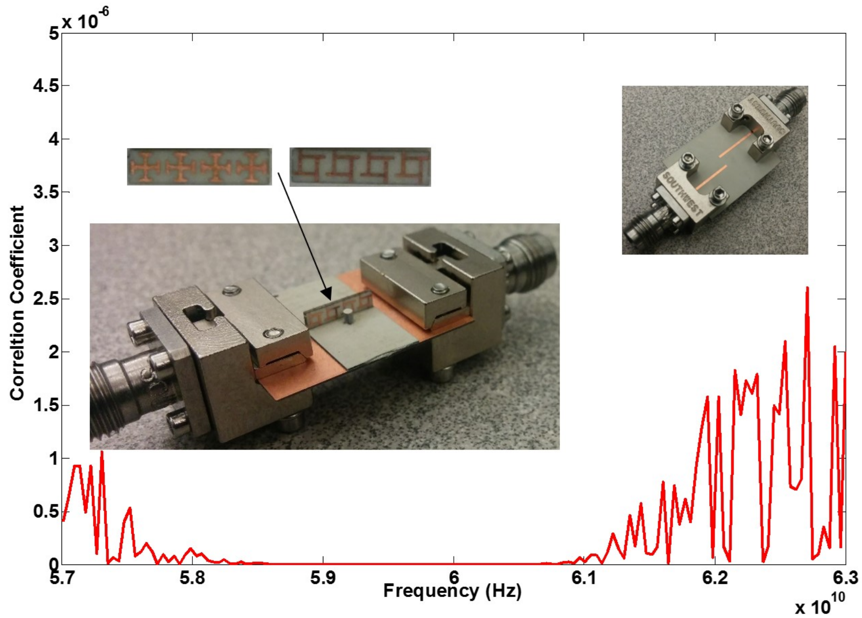

Figure 4.13 – Correlation coefficient between two antennas along with the fabricated prototype of the antenna system with FSS wall[9]

provides a wide bandwidth of 30 GHz from 40 to 70 GHz with a good SE of more than 16 dB. Along with that, its symmetric structure provides polarization-independent nature. Since it is working in the U- and V-bands, it can be used for millimeter-wave shielding applications and for mutual coupling reduction. A prototype of the wideband FSS has been fabricated and measured. The obtained experimental results have shown a good agreement with the simulated ones.

Chapter 5

Active FSS based on Cantilever switches

5.1 Introduction

As mentioned in Chapter 2, periodic structures are integrated with active elements for obtaining reconfigurability in their EM characteristics. In this regard, FSS incorporated with active components such as pin diodes [14, 15, 16, 17, 18], varactor diodes [4] and MEMS switches [19, 20], its resonance properties can be varied. However, the pin diode switches are lossy and the reflection from the biasing network may reduce the overall performance of the antenna. Similar to the pin-diodes, MEMS switches can be also used in the FSS to obtain reconfigurability. In [19] MEMS switches has been implemented in the reconfigurable FSS. In most of the work, the MEMS switches have been used as a capacitive load over an aperture for the reconfigurability of the FSS. However, the capacitance variation of the MEMS switches are very low because of the small size and the cost of fabrication is also very high.

Laser machined switches can overcome these problems [58]. Comparing to the pin diode and MEMS switches, reduction in loss and capacitive variation are better in these switches. Indeed the ease of fabrication and the less need of biasing network make these type of FSS a better candidate for beam switching application for millimeter-wave antennas.

The objectives of the thesis are based on applying this kind of FSS for the beam-switching application. This chapter describes a novel type of cantilever enabled FSS which can be used for beam-switching applications at microwave and millimeter-wave frequency bands. Initially, the performance of the FSS unitcell is analyzed using CST Microwave studio for transmission and reflection characteristics. Following, the fabrication method of the FSS is explained with various scenarios. Further, the measurement of fabricated FSS prototypes using wave-guide and free-space methods for X-band and millimeter-wave frequency band respectively are explained.

5.2 Design of Cantilever enabled FSS

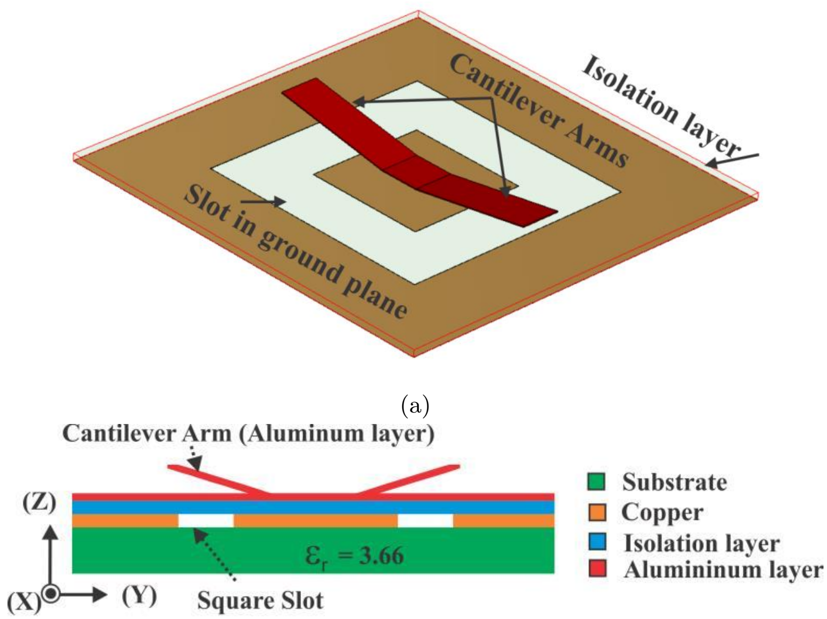

(b)

Figure 5.1 – Schematic of cantilever enabled FSS (a) Layout (b) Side view

The design of cantilever enabled FSS basically consist of two DC isolated metal layers, the lower static ground plane with slot and the upper movable cantilever arms. The basic working principle for the reconfigurable characteristics of the structure is that the movable cantilever arms capacitively load the slot and changes its resonance frequency. Figure 5.1(a) shows the layout of an active FSS unit cell comprises of a square slot and two movable cantilever arms. An initial cantilever UP state resonant frequency of the FSS is chosen first. By applying a sufficient DC-voltage between the two layers, the cantilever arms are attracted towards the ground plane and pull-down to the dielectric isolation layer. This changes the capacitance, and so the resonant frequency of the FSS structure shifts.

Figure 5.1(b) shows a side view of the active FSS unit-cell structure, where four layers of the unit-cell structure are described. The loop geometry is realized on a high-frequency laminate which acts as a supporting structure for the FSS. A thin sheet of aluminium or stainless steel can be employed to design the top layer which holds the cantilever arms. To DC isolate the two metal layers at the cantilever arms; a very thin layer of a dielectric is used.

5.3 Fabrication Process

The fabrication of the proposed type of FSS prototypes is performed by various steps. For the bottom layer of the FSS, high-frequency Roger laminates such as RO4003, R6002 are mostly used. The resonating loop structures on the upper surface of the copper laminate are etched and the bottom surface is left free of copper as shown in Figure 5.2. Further, the top metal layer is cut from the aluminium sheet or stainless steel shim of thickness $5mil$. The etching and cutting processes are performed using LPKF Protolaser laser machine (see Figure 5.5). The cantilever arms of each unit cell in the FSS panel are bent upwards to an optimized height using the laser beam. It is performed by heating the joints between the cantilever arms and the main body of the top layer precisely using laser. The fabricated top layer is shown in Figure 5.3.

The isolation layer between the metal layers is made using a thin layer of enamel paint. A thin coating of enamel paint is sprayed uniformly over the upper surface of the copper layer. Before spraying the paint, the center portion of the slot structure is masked, so that portion will be free of the isolation layer. After the curing of paint, the masks are removed and the top metal layer is placed over it. The center portion of the active layer of each unit cell is soldered to the circular portion of slot etched on the copper layer. The final prototype of the fabricated FSS panel is shown in Figure 5.4.

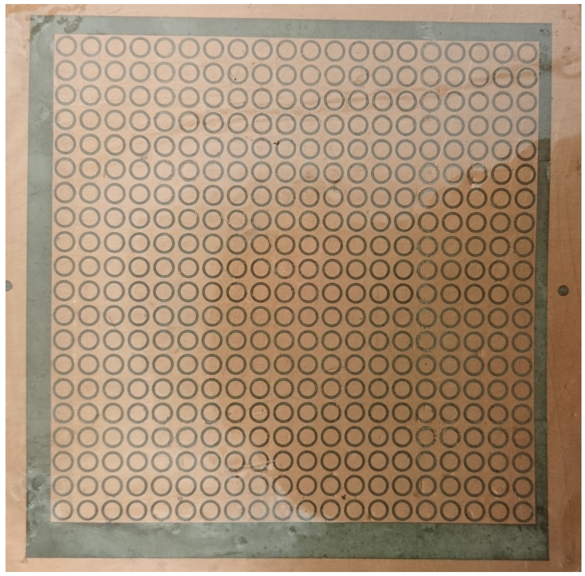

Figure 5.2 – Fabricated prototype of copper laminate layer

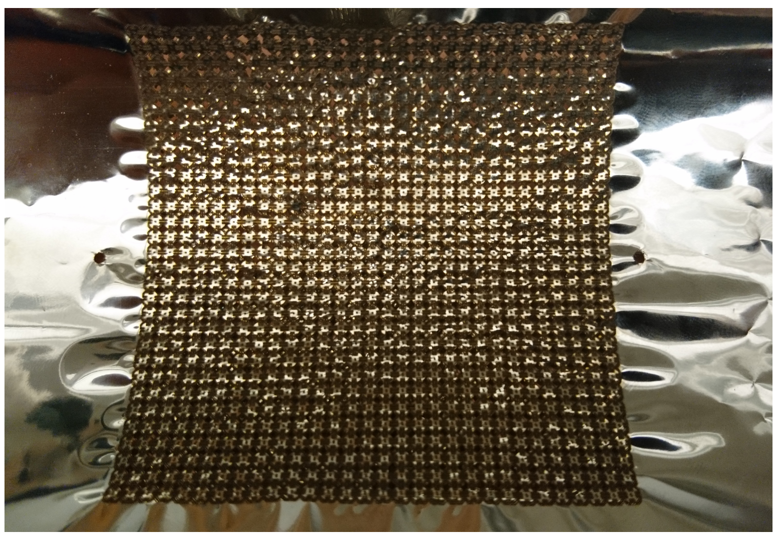

Figure 5.3 – Fabricated prototype of top metal layer

5.4 Measurement Methods

For the characterization of the FSS prototypes, two methods are used here, the waveguide method and free-space measurement method. Mainly the S-parameters of the FSS are measured using two-ports of network analyzer Agilent 8277ES. The cantilever enabled FSSs proposed here are bandpass FSS, so the measurement of transmission coefficients are performed.

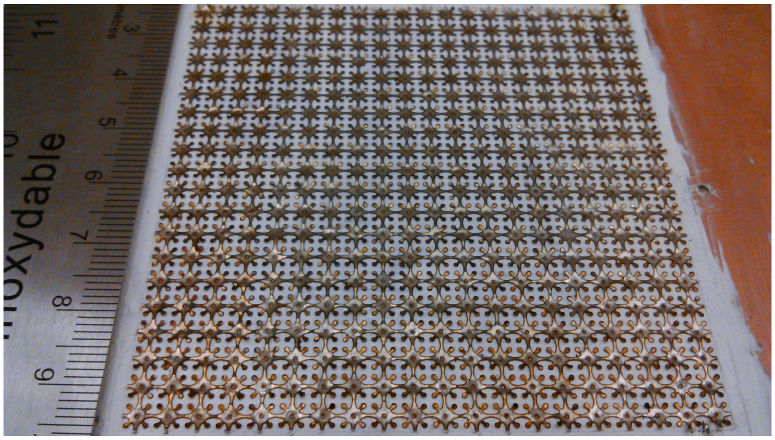

Figure 5.4 – Fabricated prototype of cantilever enabled FSS

Figure 5.5 – LPKF Protolaser laser machine

5.4.1 Waveguide Measurement

To validate the working principle of the cantilever based FSS, prototypes at X-band frequency is fabricated and measured. The waveguide measurement method is used for the characterization of this FSS prototypes at X-band frequency [59].

A unit cell of the proposed FSS is designed for X-band frequency. Nevertheless, the free-space parameters of the FSS unit cell are slightly modified to adjust for the effect of waveguide

(a)

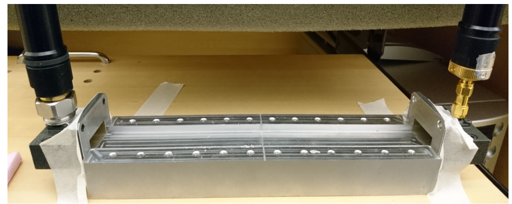

(b)

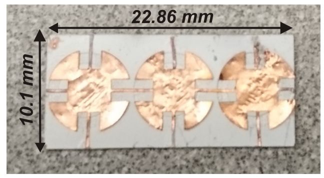

(c)

Figure 5.6 – Waveguide measurement setup, WR90 waveguide (a) closed (b) half opened (c) prototype

environment. The design of periodicity of the FSS can be perturbed by the sides of the waveguide when the image theory is applied. In order to avoid this perturbation, the period of the FSS is changed, so that the symmetry planes of FSS lie on the walls.

For the measurement of the FSS prototype, a WR90 waveguide structure is manufactured as shown in Figure 5.6 (a)-(b). Both ends waveguide structure are having a waveguide to coaxial transition for connecting to the two ports of the network analyzer. The waveguide is fabricated in a manner to have two hemispheres, top and bottom, for the placement of FSS prototype inside it. The FSS prototype with two unit cells of the proposed design as shown in the Figure 5.6 (c) is tested inside the waveguide. The size of the prototype is scaled to 22.86 $mm \times 10.16$ mm for the placement inside the waveguide.

5.4.2 Free-space Measurement

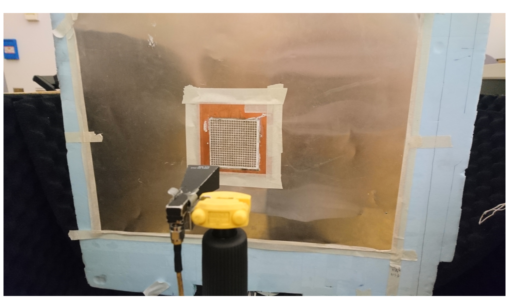

(a)

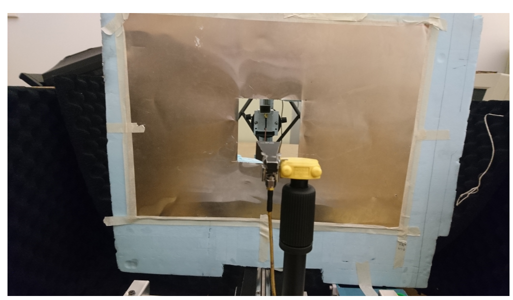

(b)

Figure 5.7 – Free space measurement setup (a) with FSS panel (b) with-out panel

The free space measurement setup is used for the characterization of FSS panels at millimeter-wave. In this measurement setup, two symmetrical pyramidal standard horn antennas operating in Ka-band frequency with 18 dB gain are used (see Figure 5.7). One antenna is facing the FSS and the another one facing the back of the FSS. The transmission characteristics of the FSS panel, which is kept in between the horn antennas using a prototype holder, is measured. The transmission coefficients of horn antennas without the FSS panel are measured initially to obtain the calibrated results and remove any interfaces with the surrounding objects. The FSS holder is a large reflecting metal plate having a space to hold the FSS at the center. [60]

5.5 Conclusion

In this chapter, the design, fabrication and the measurement methods of the proposed cantilever enabled FSS structure have been described. Two models of cantilever enabled FSS have been fabricated, one resonating in the X-band and the other in the 30 GHz frequency band. The waveguide and the free-space measurement setups have been implemented for the lower and higher frequency prototypes, respectively.

Chapter 6

Study, design and implementation of *mm*-wave beam-switching antenna

6.1 Introduction

As the evolution of wireless communication systems has entered 5G technology, there is much demand for greater spectrum allocations at millimeter-wave frequency bands, high directive beamforming antennas base stations, higher bit rates, low-cost infrastructure and higher aggregate capacity [61]. In this perspective, reconfigurable antennas should be exploited for millimeter-wave smart antenna array systems with more flexible and robust antenna elements to achieve more efficient communication systems.

In the literature, many contributions have been reported in designing beam-switching antennas using electronic components. The concept of beam-switching has been introduced by Harrington, in which reactive loaded dipoles have been used to obtain radiation-pattern reconfigurability [13]. Using the similar concept, frequency selective surfaces have widely been used in beam-switching antennas. Basically, an FSS is a periodic structure, when excited with a uniform plane wave, it acts as a bandpass or band-reject spacial filter according to its configuration. When incorporated with some electronic components such as pin diodes [14, 15, 16, 17, 18], varactor diodes [4] and MEMS switches [19, 20], its resonance properties can be electronically changed and has been used in beam-switching applications. In [14, 15, 16, 21], similar FSS screens have been used as a cylindrically shaped partially reflective surface around an omnidirectional source antenna for radiation beam-switching. A nimble radiation pattern structure and a wideband sweeping beam antenna using a hybrid structure have been described in [15] and[14], respectively. To obtain better continuous sweeping of beam in the azimuth plane, a cylindrical slot FSS has been used in [22]. Similarly, in [17, 4, 23], the FSS panels have been made into sectoral shapes around a source antenna for beam-switching. A high-gain sectoral antenna has been proposed in [17] using metal sheet guided structures in the front of the reconfigurable FSS screens. Further, a ten-sided sectoral antenna has been described in [4], where varactor diodes were used as the active element, in the FSS for radiation pattern switching for single and dual-beam modes. Recently, a dual-band beam sweeping antenna using two cylindrical active FSS operating at 2.45 GHz and 5.2 GHz has been proposed in [24], where two frequency bands can work independently in the same antenna system. As the number of active components used increases, the antenna efficiency will be decreased and its complexity will be increased. In addition, the cost of those components in the millimeter-wave frequency band is too high.

Recently, a kind of laser machined reconfigurable FSS has been proposed by in [58, 62, 63]. In this work, we propose a new beam-switching technique using cantilever switches, which can be an alternative switching method for reconfigurable antennas in the millimetre-wave frequency band. In all the references mentioned, the radiation beam switching is performed in the lower frequencies using active elements such as pin diodes and varactor diodes. Using these active elements along with their biasing circuits increases the complexity of the system and thus the efficiency of the antenna is decreased. Furthermore, the cost of the active components in the millimetre-wave frequency band is too high, as in these designs each unit cell needs at least one active element for the reconfigurability. For the validation of results, a prototype of designed FSS was initially fabricated and its transmission coefficients are measured using the free-space method. Furthermore, small panels of the proposed FSS are incorporated with a conventional radiating source with omnidirectional radiation to form a new beam-switching antenna.

In this chapter, the design principle of cantilever enabled FSS and its EM analysis are described in Section 6.2. Then, the fabrication process of the proposed FSS panels and their results are discussed in Section 6.3. In Section 6.4, the implementation of FSS panels with the DRA and analysis of simulation results are described and the experimental results of the beam-switching DRA are presented in Section 6.5.

6.2 Proposed Cantilever Enabled FSS Design

In this section, the proposed FSS unit cell with cantilever arms is described. Figure 6.1 shows the schematic structure of the FSS unit cell, which consists of four layers. The bottom layer is made of a substrate with dielectric constant 3.55, above which a copper layer is placed. The resonating component of this bandpass FSS is a circular slot with radius $R = 1.6\ mm$ and width $T = 0.4\ mm$ etched on the copper layer. The shape of the top layer is inspired from the *supershaped* structure design, where a wide variety of geometrical shapes can be generated using the *superformula* [64]. This top layer is made out of stainless steel, having four cantilever arms and four connecting lines. The two metal layers are separated using a thin dielectric layer acting as an isolation layer. The periodicity L of the unit cell is 3.7 mm.

The four cantilever arms on the top stainless steel layer act as active switches. Since the two metallic layers are isolated by dielectric substance at the cantilever arms, there is capacitive loading that changes the resonance frequency of the unit cell. The upward and downward movements of the cantilever arms vary the equivalent capacitance of the slot on the copper layer, thus providing a frequency reconfigurability characteristics to the FSS unit cell. The height h of upward bending of cantilever arms is optimized to $h = 0.1\ mm$, to get a resonance at the desired operating frequency.

The EM simulations of the FSS unit cell were performed using CST Microwave studio. In that, de-embedded Floquet ports are assigned on both sides of the unit cell to obtain its transmission and reflection characteristics. To study the frequency switching, two kinds of FSS unit cell structures are simulated, cantilever arms in the upward position (UP state) and in the downward position (DOWN state). Figure 6.2 shows the comparison of transmission characteristics for both states. It is evident from the plots that this FSS unit cell has a wide bandpass nature in the UP state around 30 GHz frequency band. Further, the transmission characteristics in the DOWN state show a good isolation of above 30 dB around the resonance frequency.

Figure 6.3 shows the transmission coefficients of the proposed FSS in both UP and DOWN states for oblique incidence. As the angle of incidence of the plane-wave, incident on the FSS varies from $0 - 60°$, stable transmission coefficients are obtained. From this analysis, it can be concluded that this FSS unit cell represents a good candidate for beam switching application. The frequency tuning of the FSS unit cell is performed by varying the height of cantilever arms to obtain a bandpass at

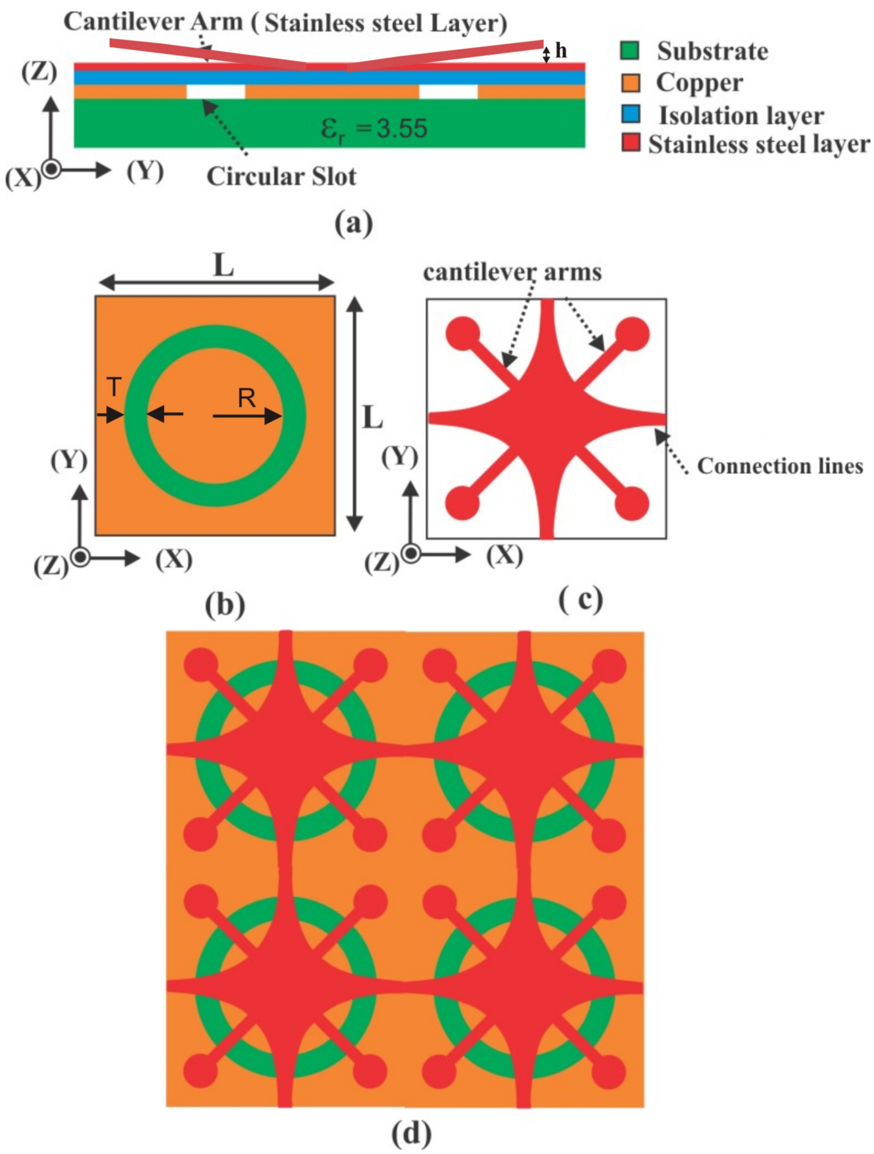

Figure 6.1 – Schematic of proposed FSS (a) Side view (b) Bottom copper layer (c) Top Stainless steel layer (d) FSS array

30 GHz, as shown in Figure 6.4. As the bending height of the cantilever arms varies, the capacitive loading of the circular ring changes, which results in the frequency reconfigurability of the unit cell. The surface current distribution of the unit-cell for both UP and DOWN states are depicted in Figure 6.5. It is observed that the intensity of surface current distribution is intense in the UP state than in the DOWN state at 30 GHz, due to the loading of the cantilever arms.

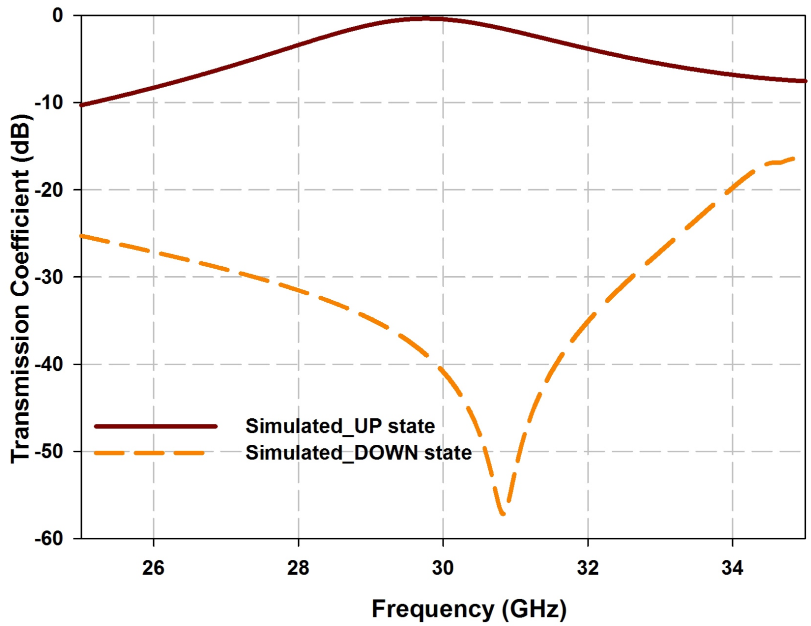

Figure 6.2 – Comparison of transmission coefficients of FSS unit cell at UP state and DOWN state

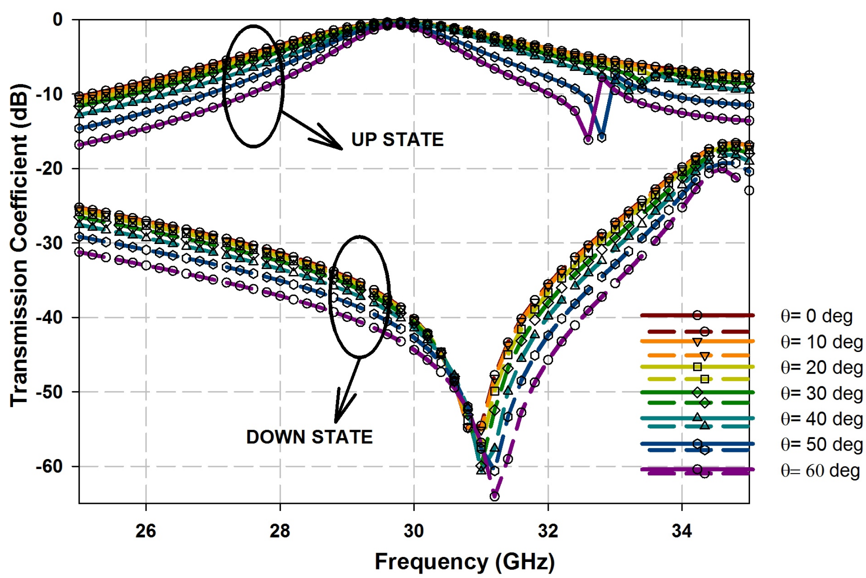

Figure 6.3 – Comparison of transmission coefficients of FSS unit cell at UP state and DOWN state for different incident angles

6.3 Fabrication and Measurement Results

The realization of the cantilever based FSS is done by fabricating $40 \times 40\ mm^2$ array on RO4003C substrate as the bottom layer. In order to prove the concept of the proposed design, both UP state and DOWN state panels are fabricated. The top active layer of each panel is carved on a thin stainless sheet using laser beam and placed over the substrate. To create an isolation layer, between

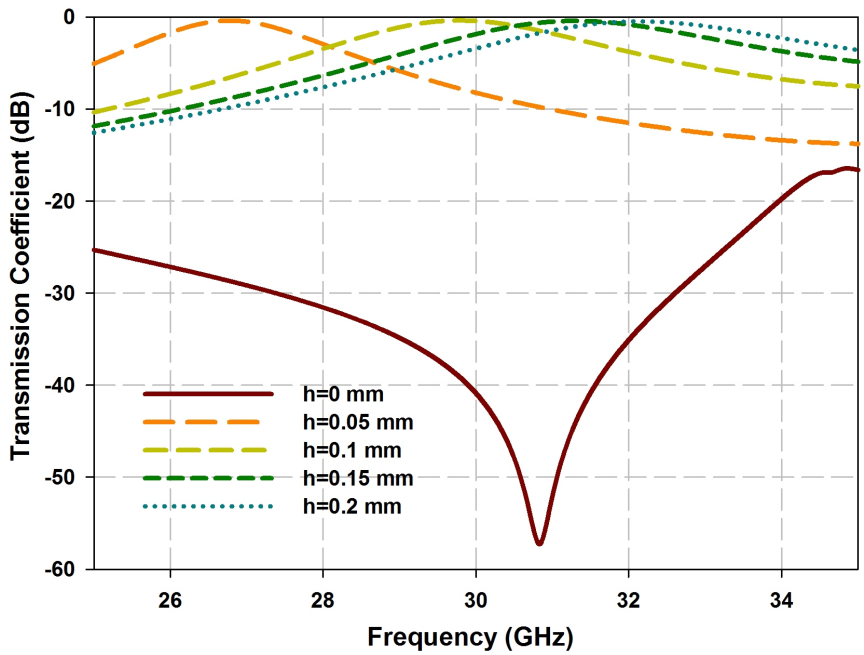

Figure 6.4 – Comparison of transmission coefficients of FSS unit cell for different heights of cantilever arms

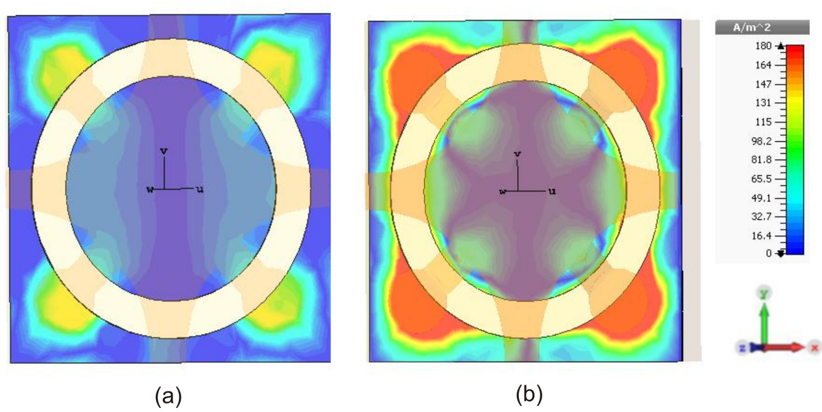

Figure 6.5 – Surface current distribution at 30 GHz (a) DOWN state (b) UP state

the copper layer and the stainless steel layer, a thin coating of enamel paint is sprayed uniformly with a thickness of 0.02 mm over the copper layer. In the UP state panel, the center portion of the slots on the copper layer are masked before coating the paint, so that portion will be free of the isolation layer. After painting, the masks are removed and the carved top layer is glued to the bottom layer at the connection lines only. The cantilever arms of each unit cell in the FSS panel are bent upwards to an optimized height using the laser beam. It is performed by heating the joints between the cantilever arms and the main body of the toplayer precisely using laser. Furthermore, the center portion of the active layer of each unit cell is soldered to the circular portion of the slot

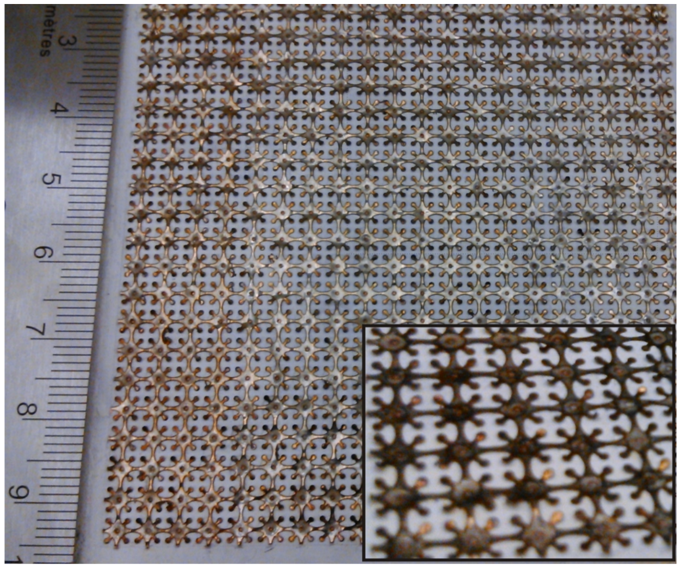

Figure 6.6 – Fabricated prototype of proposed FSS (UP state) with zoomed view given as inset

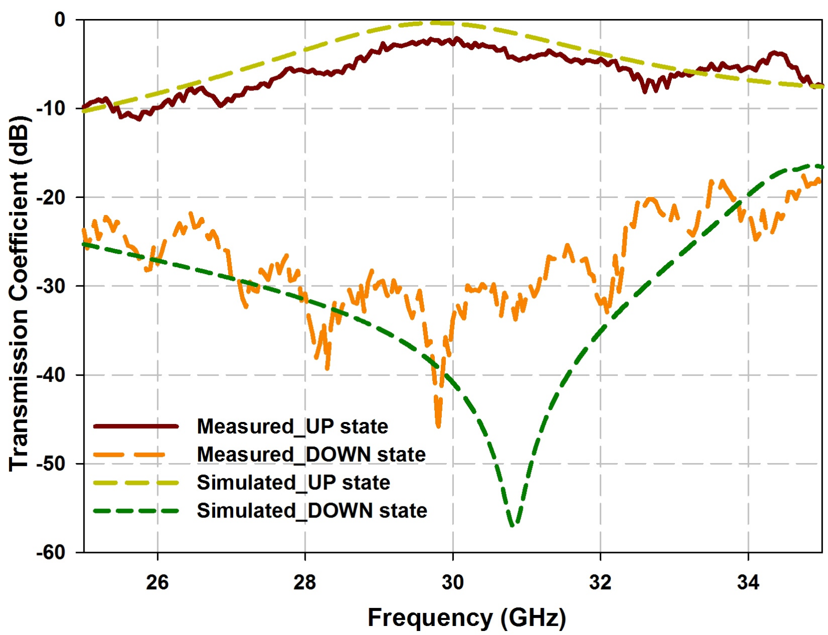

Figure 6.7 – Comparison of simulated and measured transmission coefficients for both UP and DOWN states

etched on the copper layer. But in the DOWN state panel, the whole top layer is glued to the paint-coated copper layer, so that all the cantilever arms of this FSS panel would be in the unbend position.

The fabricated FSS panel, as shown in Figure 6.6, is measured using the free-space method. Two symmetrical pyramidal standard horn antennas operating in Ka-band frequency with 18 dB gain are used in the measurement setup. Using the network analyzer Agilent 8277ES, the transmission characteristics of the FSS panel, which is kept in between the horn antennas using a prototype holder, is measured. To obtain the calibrated results, the transmission coefficients of horn antennas without the FSS panel are measured initially.

The comparison between simulated and measured transmission coefficients is shown in Figure 6.7. The measured results show a good agreement with the simulated ones. Isolation about 20 dB is achieved between the UP and DOWN states at the resonant frequency of the FSS.

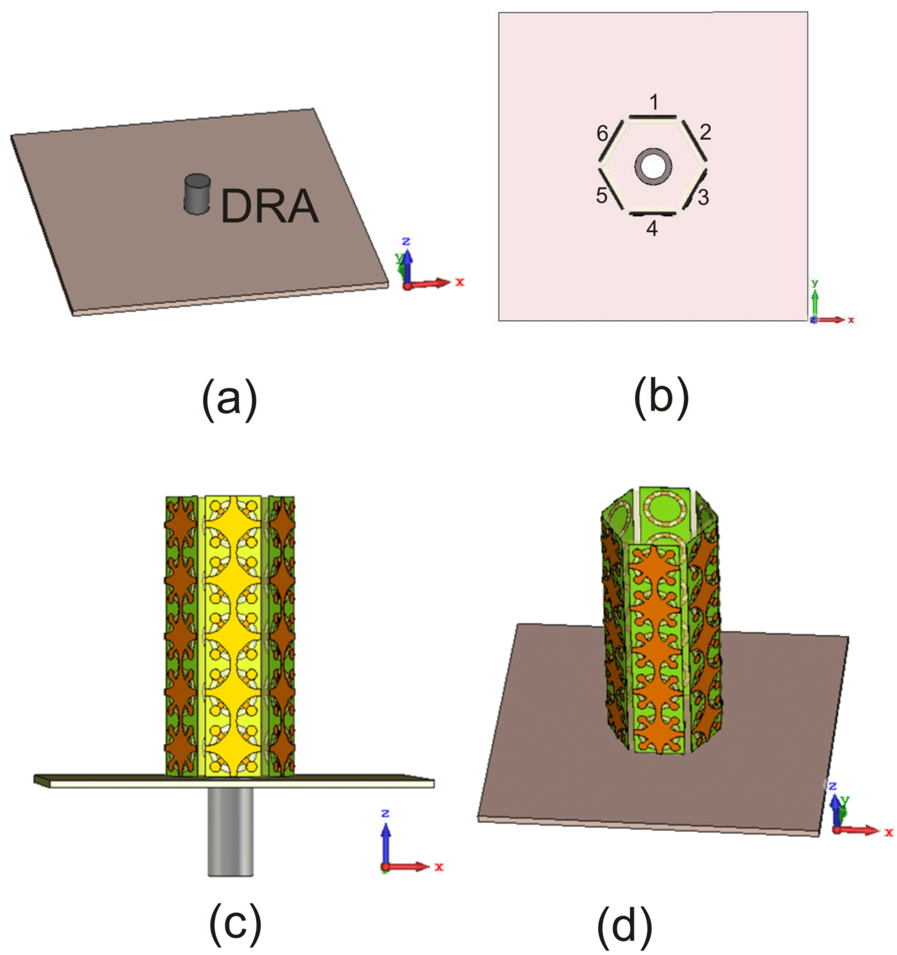

Figure 6.8 – Schematic of Beam-switching DRA (a) DRA alone, DRA with FSS (b) Top view (c) Side view (d) Perspective view

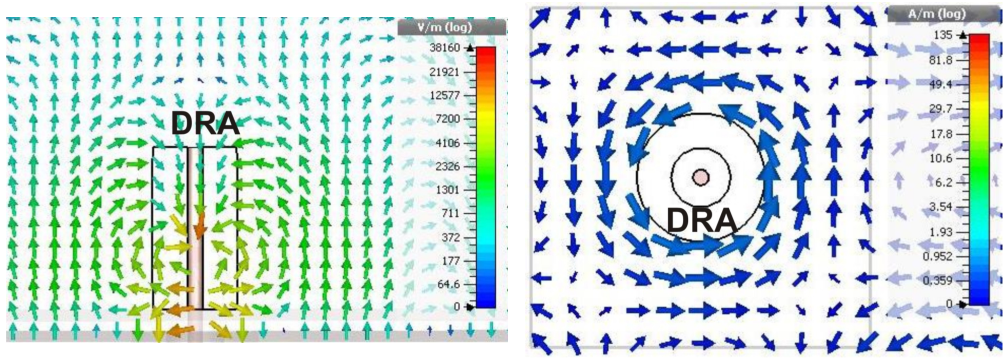

(a)

(b)

Figure 6.9 – Field distribution of DRA at 30GHz (a) E-field (XZ plane) (b) H-field (XY plane)

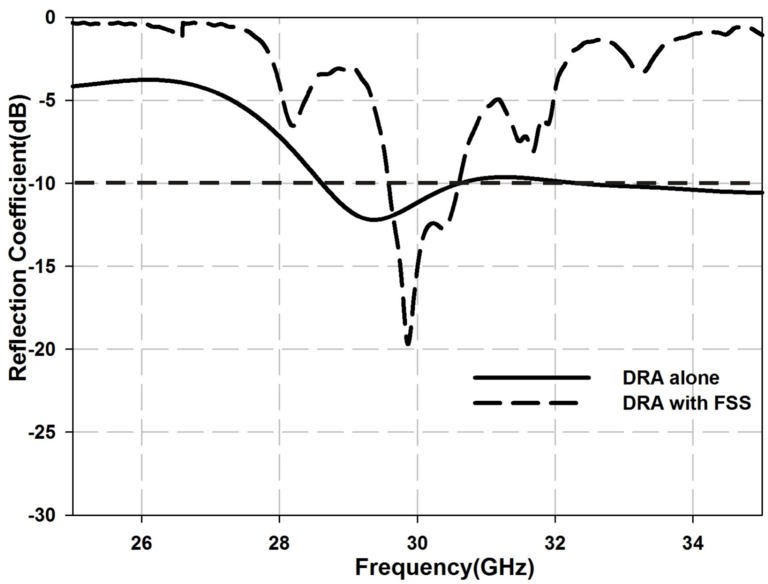

Figure 6.10 – Comparison of reflection coefficients of DRA with and without FSS

6.4 Beam-switching with DRA source

The proposed reconfigurable FSS explained in the previous section is embedded with a conventional dielectric resonator antenna for the beam-switching applications. The DRA consist of a cylindrical DR is placed over a ground plane and fed with a coaxial feed as shown in Figure 6.8(a). When the DRA is fed with a coaxial monopole feed from the bottom center, the current flowing in the monopole excites TM_{01} mode in the DRA. Figure 6.9 shows the E-field and H-field distribution of TM_{01} mode excited cylindrical DRA which is responsible for the omnidirectional radiation pattern. The radius and height of the DRA are optimized to 1 *mm* and 2.54 *mm*, respectively. The DRA is composed of a material with a dielectric constant 10.2 and placed over a ground plane made of RT6002 laminate with a thickness 0.508 *mm*.

The omnidirectional radiation pattern of the DRA in the azimuth plane is converted into a directive beam by incorporating the proposed FSS panels around it. 1x5 array of the cantilever enabled FSS unit cell are arranged as six side-panels of a hexagonal geometry and placed over the ground plane, as shown in Figure 6.8(b)-(d). Since the DRA is placed at the center of the FSS panel, which is considered as the focus of the parabolic FSS reflector panels. The radial focal distance from the DRA to the FSS panels is chosen as a value between $0.4\lambda - 0.7\lambda$ [15], where λ is the resonant wavelength, and here we optimized this distance into 0.4λ. Among the six panels, two consecutive panels is fixed in UP state and the remaining four panels are in the DOWN state. Since the two UP state panels act as bandpass FSS, the radiation from the DRA at these panels is unblocked. On the contrary, the radiation at the DOWN state panels is blocked and get reflected. Moreover, there is a constructive interference of in-phase radiated and reflected waves at the DOWN state panels towards the UP state panels, which confines the number of consecutive panels in UP state to two as well as enhances the gain of the antenna. As shown in Figure 6.11, by configuring the state of the six panels with different setups, we can achieve the beam-switching in six directions in the azimuth plane of the DRA.

The EM simulations of the beam-switching DRA were carried out, and the results obtained are shown in Figure 6.12-6.14. The reflection coefficient of the cylindrical DRA, as shown Figure 6.10, is affected by the placement of FSS panels due to their coupling effect. To compensate for that effect, the height of DRA is optimized to obtain a resonance at 30 GHz. The beam switching of DRA is investigated after placing the FSS panels. The radiation patterns at 30 GHz for each setup in Figure 6.11 are investigated, as shown in Figure 6.12. It is evident from the plots that beam switching is obtained in the whole azimuth plane with an interval of 60°.

Furthermore, the simulation of beam-switching DRA for dual-beam radiation pattern is also investigated. As shown in Figure 6.13, two opposite side FSS panels are set to UP state and the other left panels to DOWN state to obtain dual-beam radiation pattern. In *Case* 7, two beams are formed towards 90°-270° as shown in Figure 6.14. Similarly in *Case* 8 and *Case* 9 dual beams are formed at 30°-210° and 150°-330°, respectively.

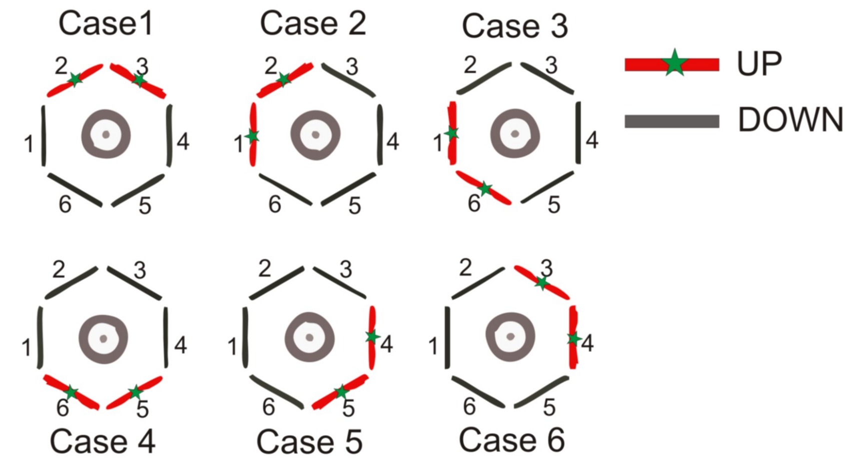

Figure 6.11 – Configuration of beam switching DRA for different cases

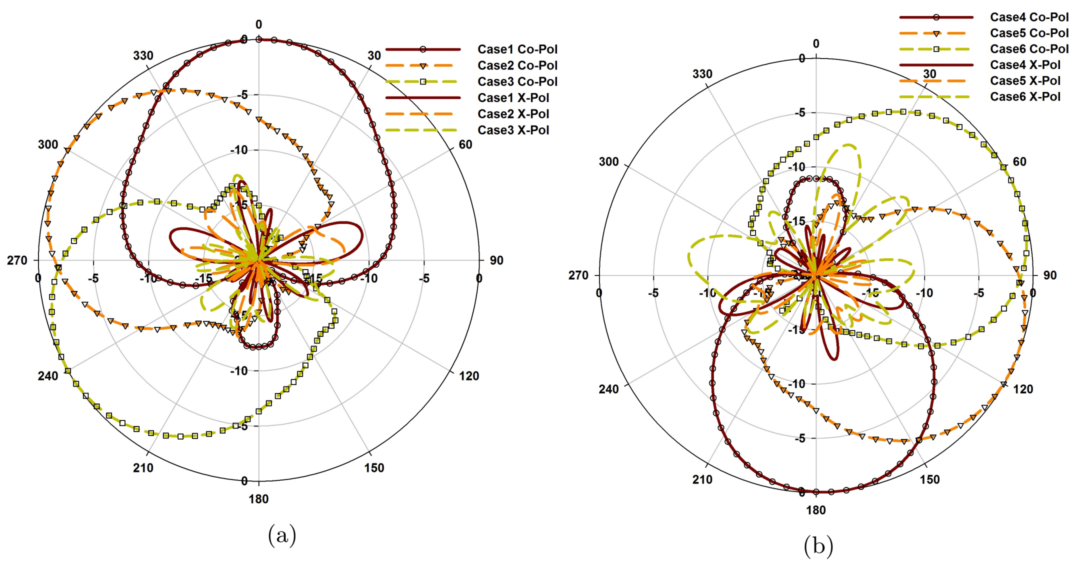

Figure 6.12 – Comparison of normalized radiation patterns at azimuth plane for different cases (a) Case1-Case3 (b) Case4-Case6

6.5 Fabrication and Experimental Results

Figure 6.15 shows the fabricated prototype of the DR placed over a ground plane, which is fed with a 2.92 mm (K) coaxial connector. The cylindrical DRA was fabricated using RT6010 substrate with 2.54 mm height. Six panels of the proposed cantilever enabled FSS were fabricated by the method mentioned in Section 6.3 and fixed over the ground plane using *Rohacell* $31HF$ foams, as shown in Figure 6.16.

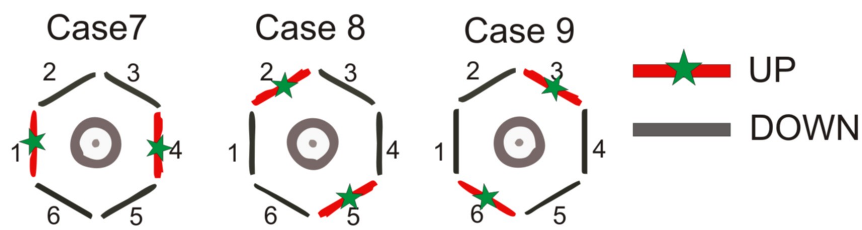

Figure 6.13 – Configuration of beam switching DRA for dual-beam cases

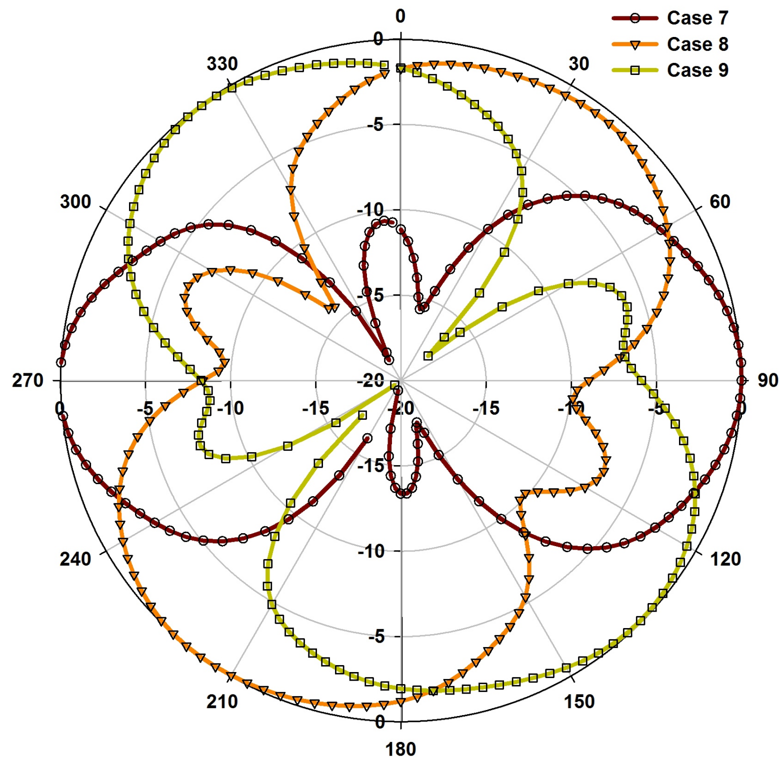

Figure 6.14 – Comparison of normalized simulated radiation patterns for dual-beam cases cases

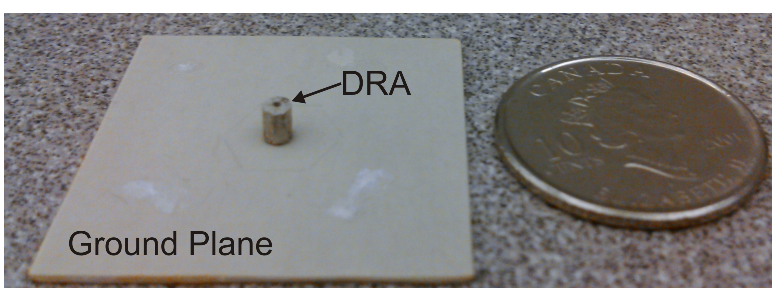

Figure 6.15 – Fabricated prototype of DRA

Figure 6.18 shows the MI Technologies Inc. anechoic chamber for the radiation pattern measurement at millimeter-wave frequency bands. In this setup, a reference horn antenna beam is reflected by a reflector towards the antenna under test. The radiation pattern of DRA at 30 GHz

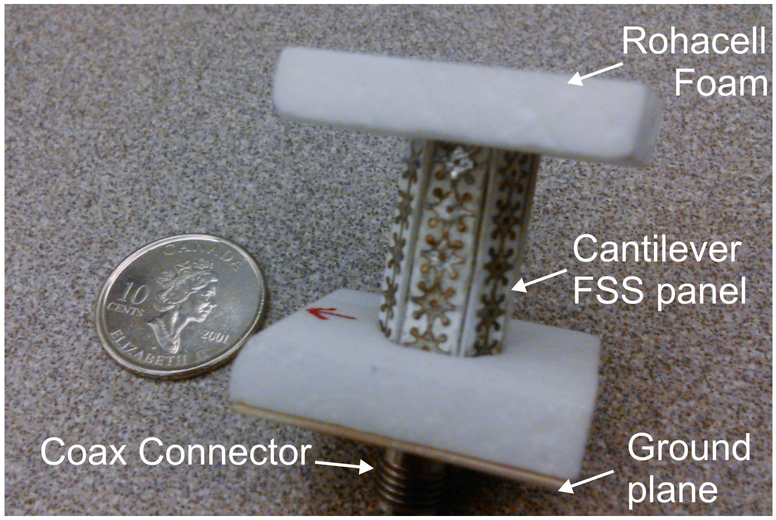

Figure 6.16 – Fabricated prototype of beam-switching DRA

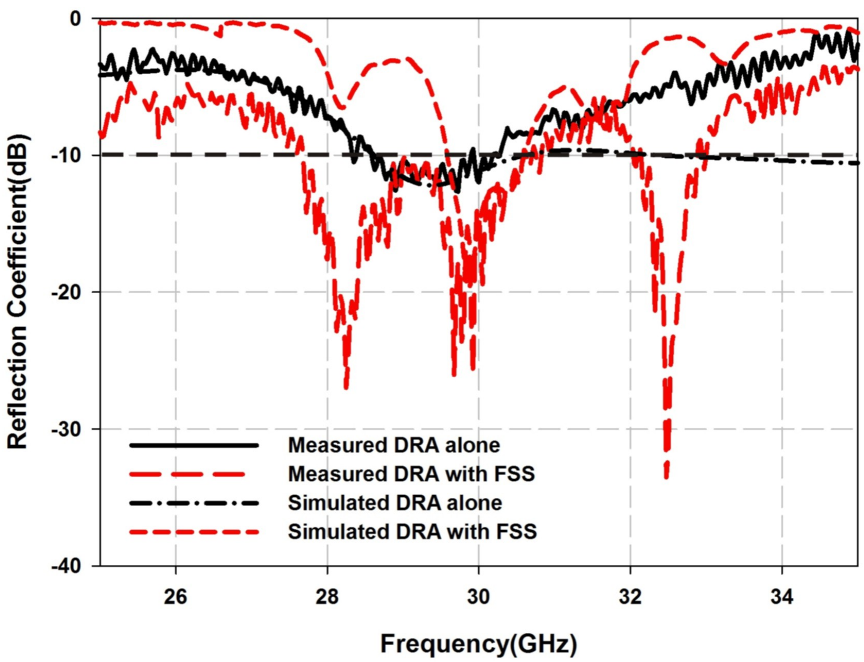

Figure 6.17 – Comparison of simulated and measured reflection coefficients of beam-switching DRA

is measured without FSS in the azimuth plane and compared with the simulation results, as shown in the Figure 6.19. The measured omnidirectional pattern has less than 5 dB variation with simulated radiation pattern. The comparison between measured and simulated reflection coefficients of DRA with and without FSS is shown in Figure 6.17, and they show good matching less than -10 dB at 30 GHz. After placing the six FSS panels around the DRA, beam-switching radiation patterns at 30 GHz for different setups are measured and compared with the simulated ones, as shown in Figure 6.20. A good agreement between the measured and simulated radiation patterns

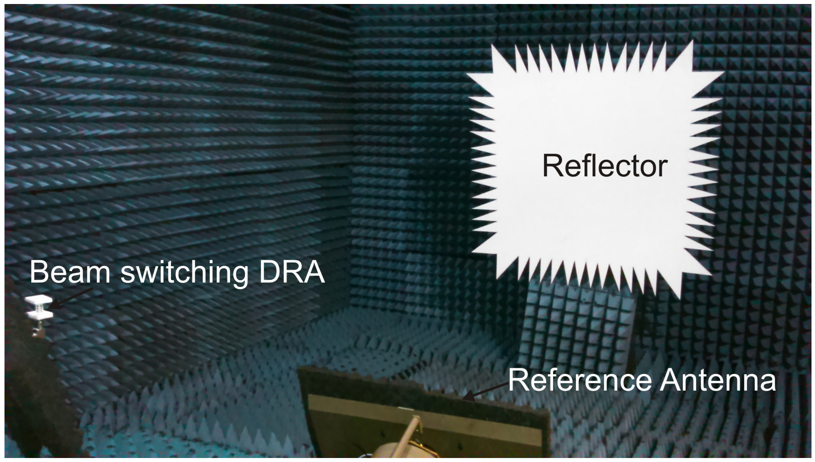

Figure 6.18 – Radiation pattern measurement setup

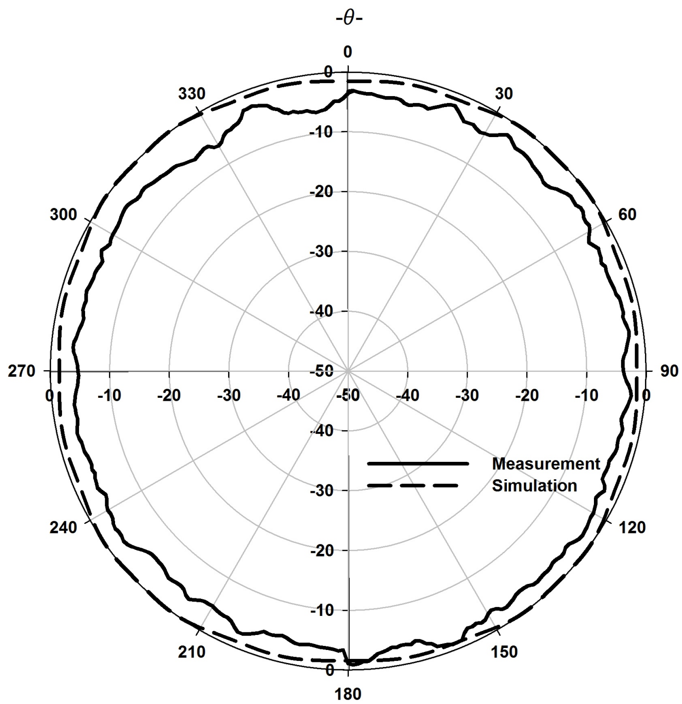

Figure 6.19 – Normalized simulated and measured radiation patterns at azimuth plane of DRA

are obtained. The direction of beams and beamwidths of the measured switching radiation patterns is roughly similar to the simulated ones. The presence of back lobes in the measured patterns is due to fabrication imperfection of the DOWN state FSS panels.

Table. 6.1 shows the measured and simulated maximum realized gains of the DRA. Due to the effect of loss in the coaxial connector and the fabrication tolerances, the measured gain has small variations with the simulated ones. Table. 6.2 shows the comparison of the proposed beam-switching

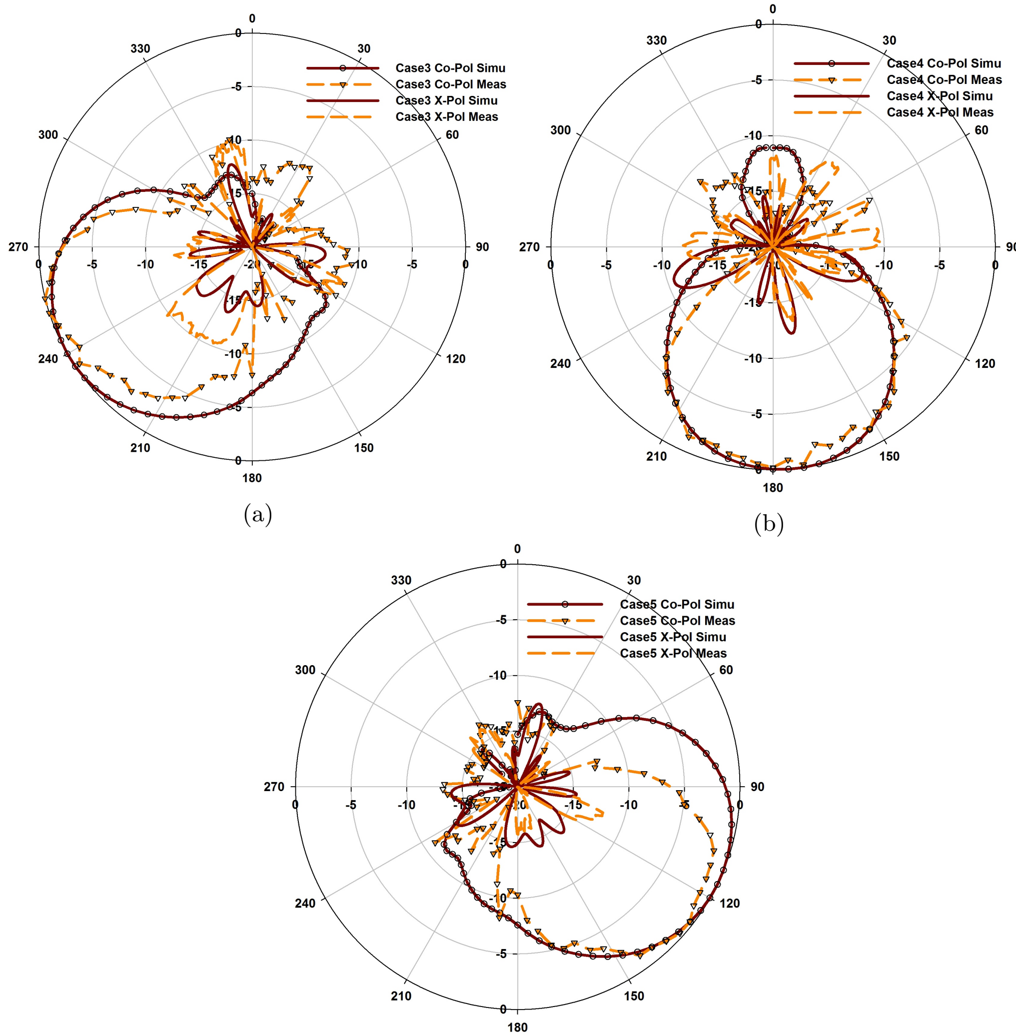

(a) (b)

(c)

Figure 6.20 – Normalized simulated and measured radiation patterns at azimuth plane for different cases (a) Case3 (b) Case4 (c) Case5

Tableau 6.1 – Comparison of simulated and measured realized gain of DRA

	DRA alone	DRA with FSS
Simulated	4.2 dB	7.2 dB
Measured	2.9 dB	6.1 dB

antenna with the previously reported works. Comparing to the other works using pin-diodes, this antenna lacks the losses due to the biasing circuitry and the associated components.

Tableau 6.2 – Comparison of proposed antenna with the previous works

References	[14]	[22]	Proposed
Frequency	2.45 GHz	2.4-2.5 GHz	30 GHz
Switching method	Using pin-diode enabled active cylindrical FSS	Using pin-diode enabled cylindrical slot FSS	Using cantilever enabled FSS
Dimensions	$1.3\lambda\times 1.3\lambda\times 1.6\lambda$	$1.7\lambda\times 1.7\lambda\times 1.6\lambda$	$1.5\lambda\times 1.5\lambda\times 1.8\lambda$
Gain	6 dB	8.7 dB	6.1 dB

6.6 Conclusion

In this chapter, a beam-switching DRA based on cantilever enabled FSS at 30 GHz has been proposed. A cantilever enabled FSS has been designed at 30 GHz as the active element for beam-switching and its transmission coefficients have been investigated. For the validation of results, the panels of the proposed FSS have been fabricated and measured to obtain a good isolation between UP and DOWN states of the FSS. Furthermore, by implementing the FSS panels around a cylindrical DRA, beam-sweeping of all angles in the azimuth plane by six steps has been achieved. In addition, a dual-beam configuration of beam-switching DRA has also been analyzed. In order to validate the concept of proof, a prototype of the beam-switching DRA has been fabricated and its radiation patterns in the azimuth plane have been measured and shown a good agreement with the simulated ones.

Chapter 7

mm-wave Dual-plane Beam-sweeping antenna

7.1 Introduction

Since the emergence of millimeter-wave technology, most of the research on wireless communications systems has a paradigm shift due to the challenging capacity, increased coverage range and latency demands of this communication technology. Adaptive antenna arrays and phased antenna arrays are the conventional solutions which can be adapted for the requirements of this technology. However, due to the expensive, bulky and complexity of the feeding network of these conventional antenna array systems made many researchers to investigate other beam-scanning techniques for the future 5G antenna applications [61, 5].

In contrast to the conventional phased antenna arrays, beam-scanning antennas using reconfigurable periodic structures can be an effective candidate with reduced size, low complexity and less expensive for the improved performance of wireless communication. The concept of beam-switching using reactive loaded dipoles has been introduced by Harrington [13]. Following this concept, many works have been published in the literature, where an omni-directional source has been converted to a directional antenna. Mostly reconfigurable FSS screens have been used for this kind of directional antennas [65, 22, 17]. FSSs are basically spatial filters of electromagnetic waves, when incorporated with some active elements such as pin-diodes[14, 24], varactor diodes[66] or MEMS[19] switches act as reconfigurable filters switching between transmitting and reflecting modes. The active screens and panels using FSS in various shapes such as cylindrical[16], semi-cylindrical[67], hexagonal[5], nanogonal[23] have been found in the literature. Recently, dual-band beam-switching antennas using pin diode enabled FSS screen have been proposed in[24, 25]. Moreover, the works with metal sheet guided structures in the front of the reconfigurable FSS screens for high-gain beam-switching have also been proposed [16][26].

For the base station antennas, along with azimuth plane beam-switching, the beam-tilting in the elevation plane has also been suggested. Some research contributions in beam-tilting can be found in the literature which includes beam-tilting using periodic surfaces such as EBG [27], metamaterials [28] and FSS [29]. In [27], a dipole array mounted on customized EBG for enhanced down-tilt beam has been proposed. Furthermore, mu-near-zero metamaterial slabs integrated with the dipole antenna to obtain E-plane beam-tilting with enhancement of gain at millimeter-wave bands has been proposed in [28]. In the concepts reported [65, 22, 17], most of the beam-sweeping techniques have been concentrated on the azimuth plane of the antenna. In these concepts, the radiation pattern of an omnidirectional source is swept using a reconfigurable FSS screen. The only work reported in the elevation plane switching is [30], where the source antenna is a two-port feed array. In this chapter, we propose a new dual beam-switching technique using cantilever enabled FSS [62], which can be feasible for base station antennas in *mm*-wave band. As an alternative of using expensive pin diodes and varactor diodes which increases the complexity of the system and decreases the antenna efficiency, cantilever enabled FSS are used for the reconfigurability of the single source beam switching antenna.

In this chapter, initially, the beam-sweeping mechanism of the reconfigurable antenna is explained. Further, the structure of the reconfigurable FSS unit-cell is designed and assessed. In further sections, design, fabrication measurement results of the proposed antenna are discussed.

7.2 Beam-sweeping mechanism

In this proposed work, we have obtained a beam-tilting on elevation plane together with the beam-sweeping in the azimuth plane, thus obtaining a new dual-plane beam-sweeping antenna using a single source. For the beam sweeping in the azimuth plane, the FSS panels are divided into six

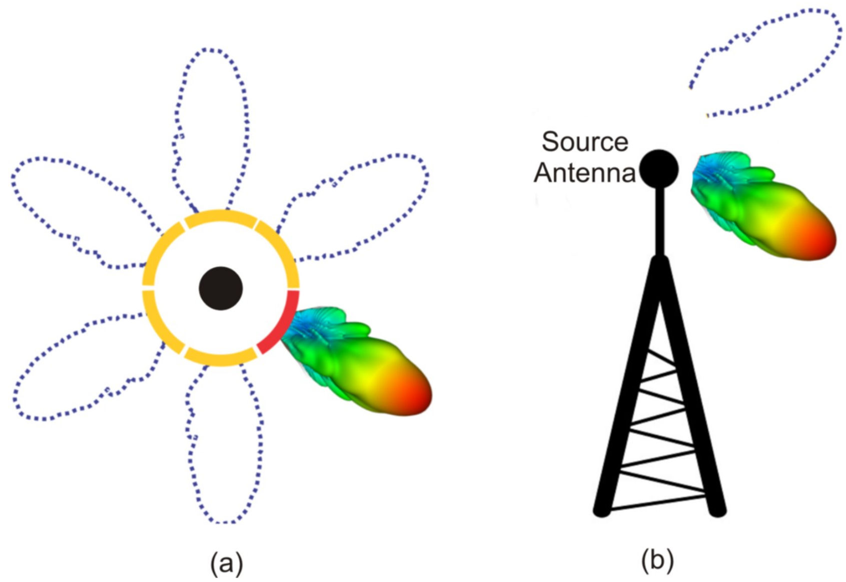

Figure 7.1 – Schematic of beam-sweeping mechanism (a) Azimuth plane (b) Elevation plane

sections as in the previous works. Similarly, the elevation plane sweeping is obtained by the division of FSS panels into two segments, upper and lower. Thus, two azimuth sweeps are obtained in the two segments of elevation angles as shown in Figure. 7.1. As the number of unit cells increases in the vertical panel, we can obtain more angles of tilts in the elevation plane.

7.3 FSS unit-cell design

The proposed FSS unit cell is a four-layer cantilever enabled structure as shown in Figure. 7.2. The top layer consists of the axe-shaped active cantilevers with the connecting lines cut out of stainless steel material. The ground layer consists of a circular slot etched on a copper laminate made of RO6002. Both the metal layers are isolated by a thin layer of epoxy-resin glue. The dimensions of the unit-cell are given in Figure. 7.2.

From the equivalent circuit as shown in Figure. 7.2(d), the resonant frequency of the FSS can be obtained as,

$$f_r = \frac{1}{2\pi\sqrt{L_1(C_1 + C_2)}} \tag{7.1}$$

where L_1 is the equivalent inductance due to the metal layers, C_2 is the equivalent capacitance of due to the slot on the ground layer and the C_1 is the coupling capacitance between the cantilever arms and the ground layer, with values optimized as $L_1 = 7.541\ pH$, $C_2 = 3.5\ pF$ and $C_1 = 0.25\ pF$.

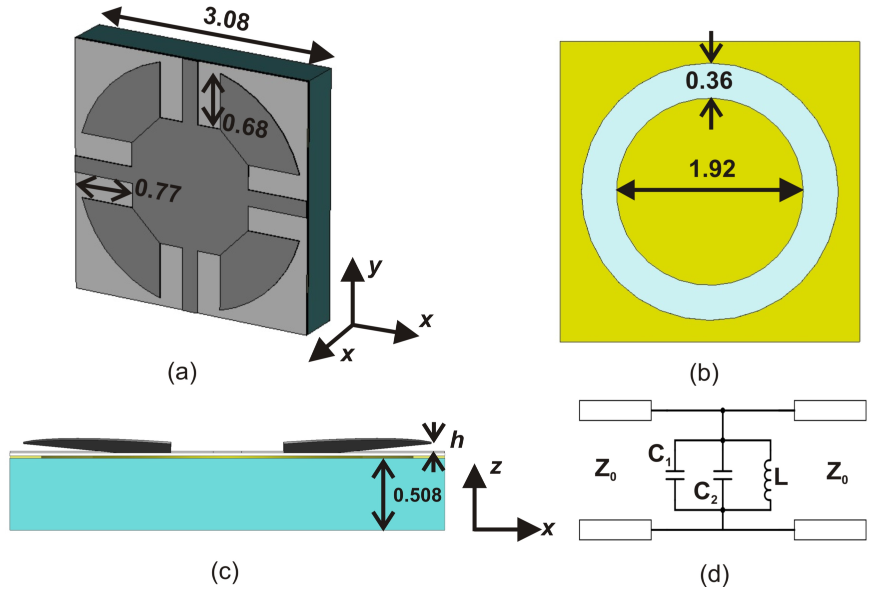

Figure 7.2 – Schematic of proposed FSS (a) Perspective view (b) Bottom copper layer (c) Side view

The working principle of the proposed FSS mainly depends on the cantilever layer of the FSS. The circular slot on the ground layer, which is a resonating structure, is loaded by the cantilever arms of the top stainless-steel layer. By adjusting the height of the bending of the cantilever arms, the capacitance between the top and ground layers gets changed and thus the resonance frequency of the circular slot can be varied. As the height of the cantilever beam is changed, the coupling capacitance C_1 is varied, i.e. they are inversely proportional to each other.

The EM simulation of the proposed unit cell is performed using the software CST Microwave studio, where floquet ports are assigned on both sides of the unit cell for the analysis. The transmission coefficients of the unit cell are shown in Figure. 7.3. As the height of the cantilever arms is varied, the resonance frequency of the unit cell is also varied. The optimized height of the cantilever arms for the resonance at 30 GHz is $h = 0.1\ mm$. Thus, the two operating states of the unit cell are confirmed at $h = 0\ mm$ and $h = 0.1\ mm$ as DOWN state and UP state, respectively. It is to be pointed that, the isolation between UP and DOWN states is obtained to be above -50 dB at the resonance frequency. The equivalent circuit is analyzed, and the scattering parameters for both UP and DOWN states are shown in Figure. 7.4. It is concluded that the value of the coupling capacitance C_1 from UP state to DOWN state varies from $C_1 = 0.25\ pF$ to $C_1 = 21.8\ pF$.

Furthermore, the unit-cell at UP state is analyzed for the various oblique incident angles of the plane wave incidence (Figure. 7.5). It should be noted that the transmission coefficient of the

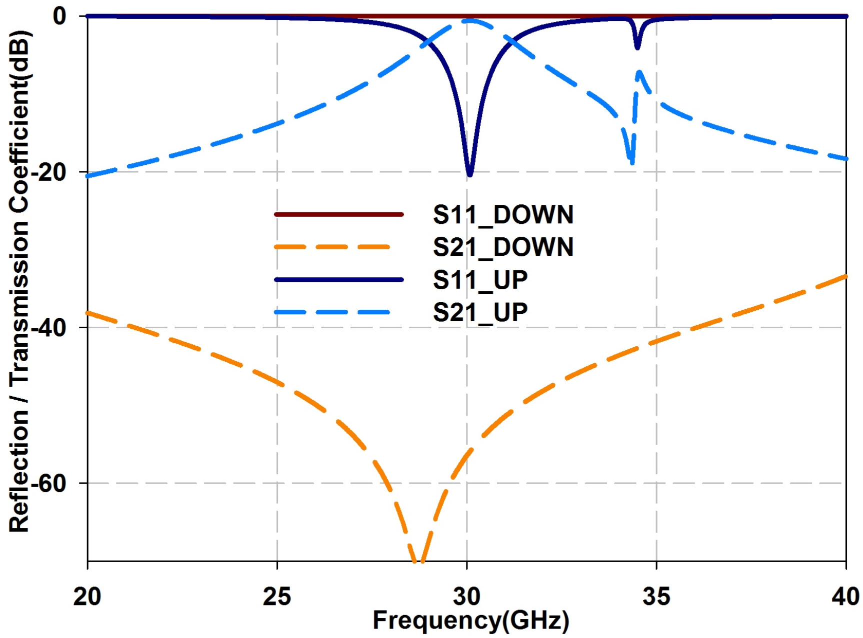

Figure 7.3 – Simulated transmission and reflection coefficients of FSS unit-cell, EM analysis for both states

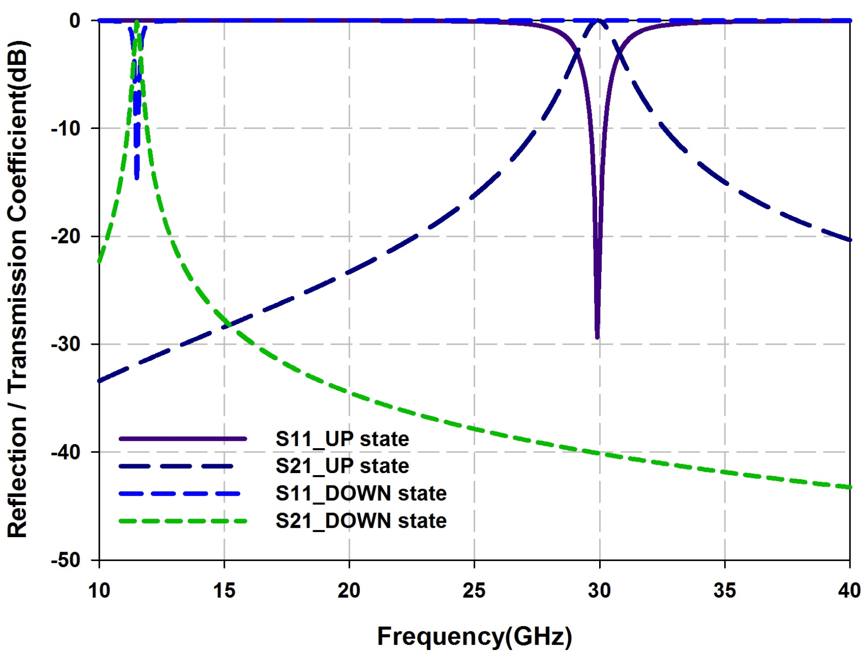

Figure 7.4 – Simulated transmission and reflection coefficients of FSS unit-cell, Equivalent circuit analysis

unit-cell does not vary much, except the transmission bandwidth. The polarization independence of this unit-cell makes it a good candidate for beam-sweeping applications at 30 GHz.

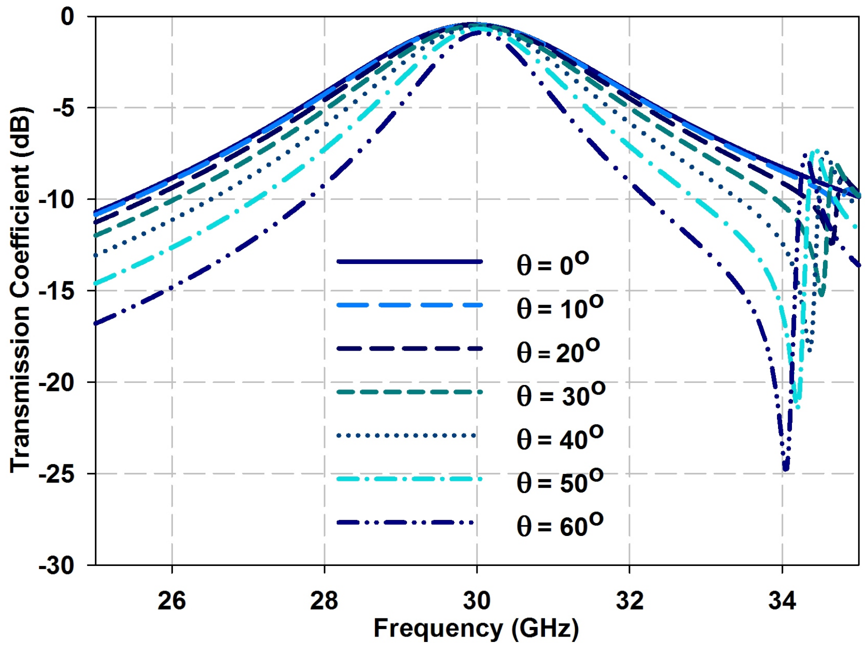

Figure 7.5 – Simulated transmission coefficients of FSS unit-cell for oblique incidence

7.4 Beam-switching antenna design

The schematic of the proposed beam switching antenna is shown in Figure. 7.6. It consists of a radiating source and FSS panels arranged hexagonally around the source. The radiating source is a conventional cylindrical DRA with a circular ground plane and fed with a coaxial feed. The DRA acts as a conventional monopole source, where TM_{01} mode has been excited by the coaxial probe and it has an omnidirectional radiation pattern in the azimuth plane and a directional pattern in the elevation plane. The optimized radius and height of the DRA are $r = 1\ mm$ and $h_1 = 2.54\ mm$, respectively. While the center feed of the coaxial port is extended to a monopole with height, $h_2 = 3\ mm$ through a circular ground plane with radius $r_2 = 15\ mm$.

Further, the six panels of 1x6 array of the proposed FSS are arranged around the DRA in a hexagonal manner to form the beam switching antenna. The radius of the FSS panels placed on the circular ground plane is optimized to obtain a better beam-sweeping and is about $r_3 = 0.45\lambda$, where λ is the wavelength at the operating frequency. Since each FSS panel is arranged in a hexagonal manner, it inclines an angle of 60° to the center. Moreover, six unit-cells of the FSS are used vertically, the total height of the antenna including the DRA is observed to be $h_3 = 18.9\ mm$.

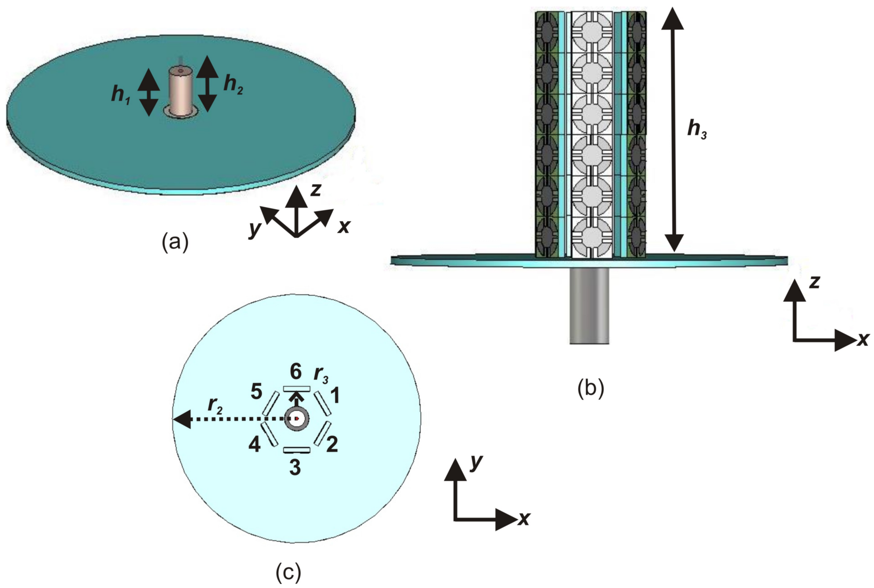

Figure 7.6 – Schematic of beam-sweeping antenna (a) DRA alone, (b) DRA with FSS Side view (c) Top view

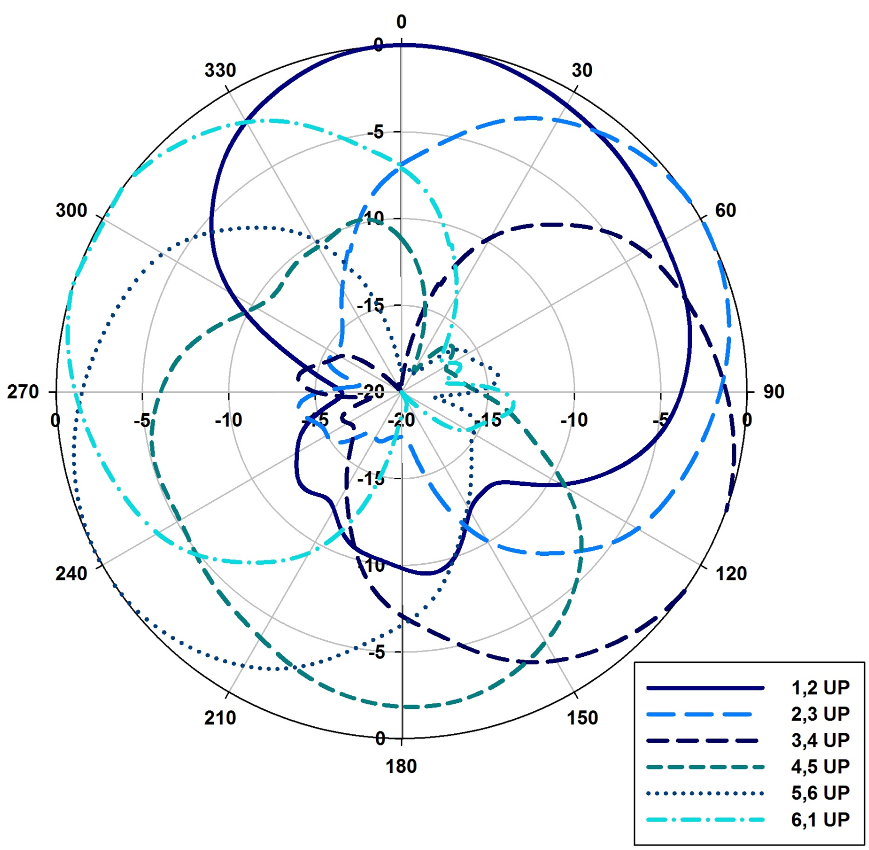

Figure 7.7 – Normalized simulated radiation patterns in azimuth plane

To evaluate the EM characteristics of the proposed antenna, simulation results are discussed. The reflection coefficient of the coax fed DRA with and without the FSS panels is shown in Fig-

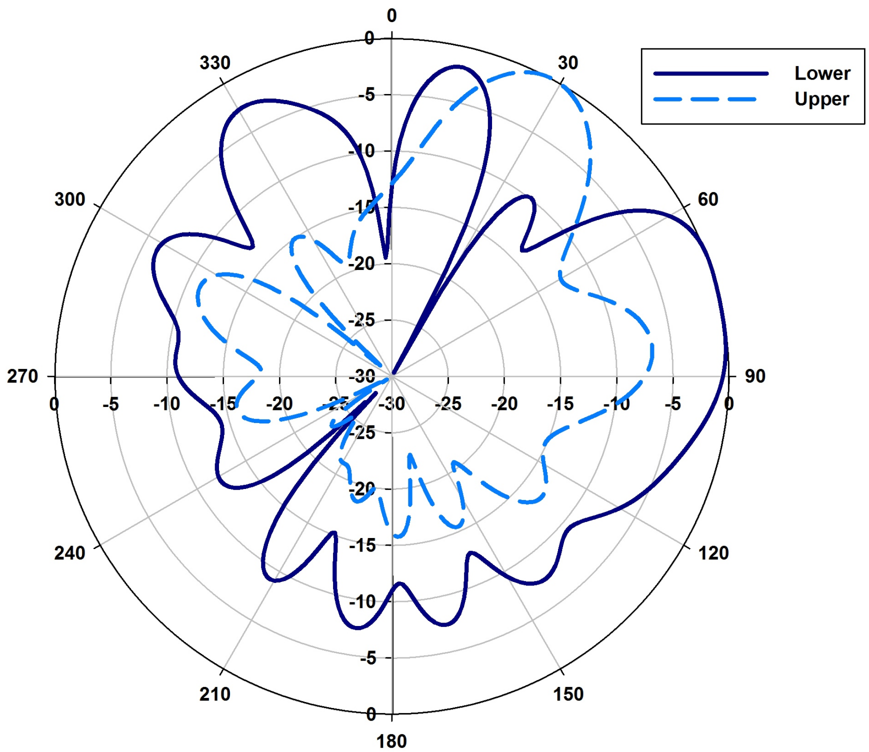

Figure 7.8 – Normalized simulated radiation patterns in elevation plane

ure. 7.10. It is evident from the plot that the matching of the antenna is changed due to the effect of the placement FSS panels, even though $S_{11} < 10\ dB$ is obtained at the resonance frequency of the antenna.

The radiation characteristics of the beam-sweeping antenna is shown in Figure. 7.7-7.8. To obtain the beam-sweeping in the azimuth plane at $\phi = 90°$, the two consecutive panels of the lower or upper segment are made to UP state. For each case, the normalized patterns are shown in Figure. 7.7, where they sweep the whole plane in six steps subtending an angle of 60°. In the elevation plane, two beams tilts are obtained at $\phi = 30°$ and $\phi = 90°$ by switching the UP states panels in the upper and lower segment, respectively. The normalized pattern of beam tilting at $\theta = 0°$ are shown in Figure. 7.8. It is evident that the side lobes for both cases are limited.

7.5 Fabrication and measurement

To validate the simulated results, a prototype of the proposed antenna as shown in Figure. 7.9, was fabricated and measured. The cylindrical DRA is fabricated on a Rogers RT6010 laminate with

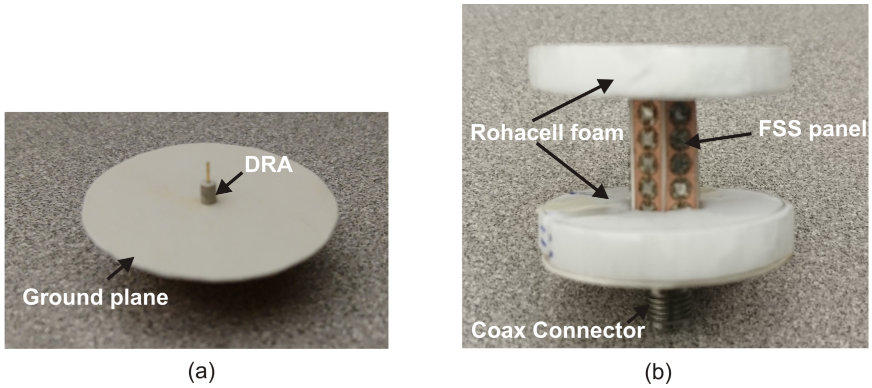

Figure 7.9 – Fabricated prototype (a) DRA alone (b) Beam switching DRA

$\epsilon = 10.2$ using LPKF protomat etching machine. Further, it is placed on a ground plane made of Rogers RT6002 laminate with $\epsilon = 2.94$ and fed with coaxial 2.92 mm (K) $connector$. The center pin of the coax connector is extended through the ground plane and DRA and the heights h_1 and h_2 are optimized to obtain a resonance at 30 GHz.

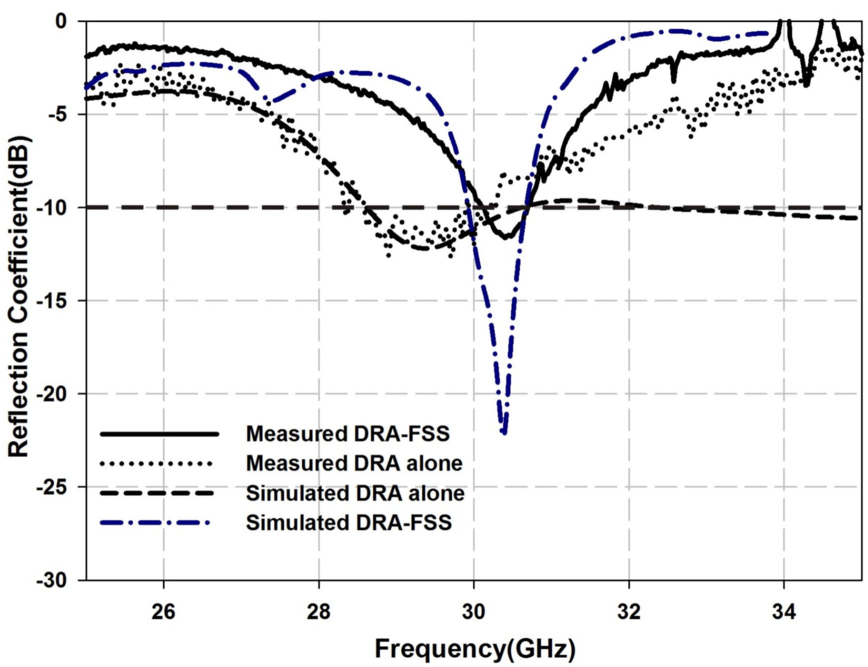

Figure 7.10 – Comparison of simulated and measured reflection coefficients of the DRA with and with out the FSS panels

The FSS panels are etched using LPKF Protolaser laser machine. The ground layer is etched on Rogers RT6002 of thickness $t = 0.508$ mm. Further, the top layer is carved on Precision brand stainless steel shim of thickness 0.013 mm. The bending of cantilever arms of this layer is performed by the sufficient heating of the cantilever arm joins to obtain the optimized height h. Both the top

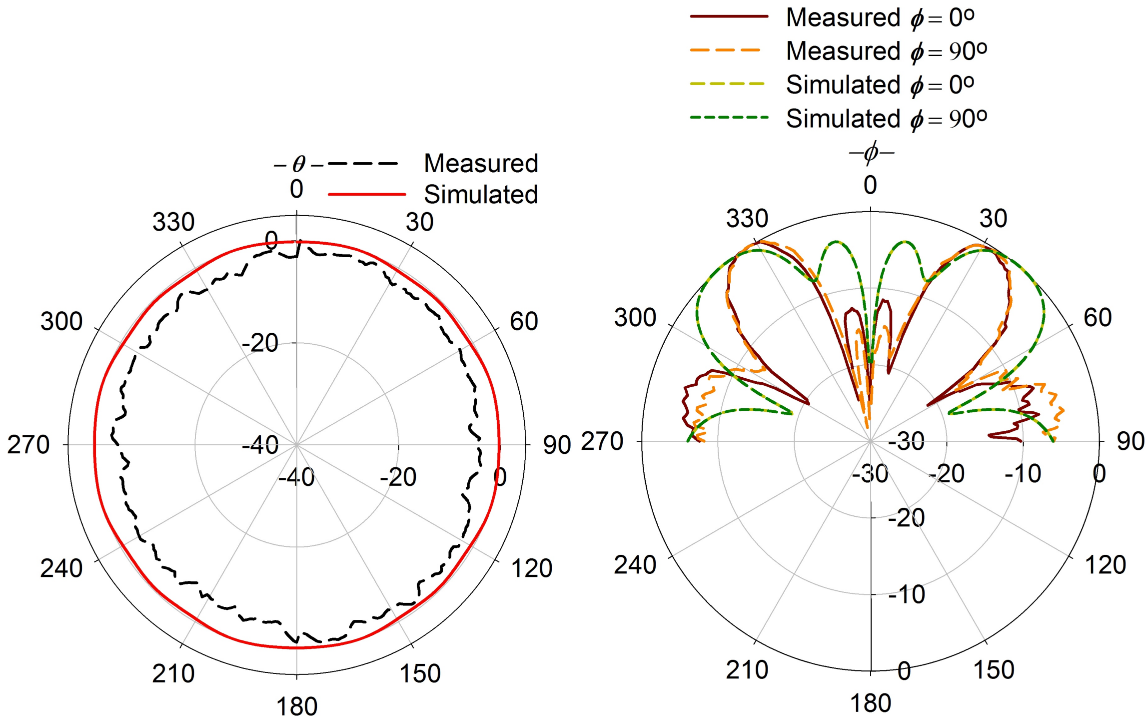

(a) (b)

Figure 7.11 – Comparison of simulated and measured normalized radiation patterns of DRA alone (a) Azimuth plane (b) Elevation plane

and ground layer are combined using epoxy glue of thickness 0.02 mm. In order to prove the concept of the proposed FSS, both UP and DOWN state panels are made separately. Only in the fabrication of UP state unit cells, the bending of cantilever arms is done. But in the fabrication of DOWN states unit cells, the whole top layer is glued to the ground layer without bending the arms.

The measured reflection coefficients of the DRA without the FSS panels and whole beam-sweeping antenna are shown in Figure. 7.10, and compared with simulated results. The small deviations of the measured results from the simulated ones are due to the fabrication errors. The radiation pattern measurement of the beam-sweeping antenna is performed in an anechoic chamber at millimeter-wave bands. Initially, the measurement of the cylindrical DRA without the FSS panels are performed and the normalized patterns compared with the simulated results are shown in Figure. 7.11. Since the DRA acts as a conventional monopole, it is observed that the patterns in the elevation and azimuth planes show directional and omnidirectional patterns, respectively. The measured patterns have a less variation than 5 dB compared with the simulated ones.

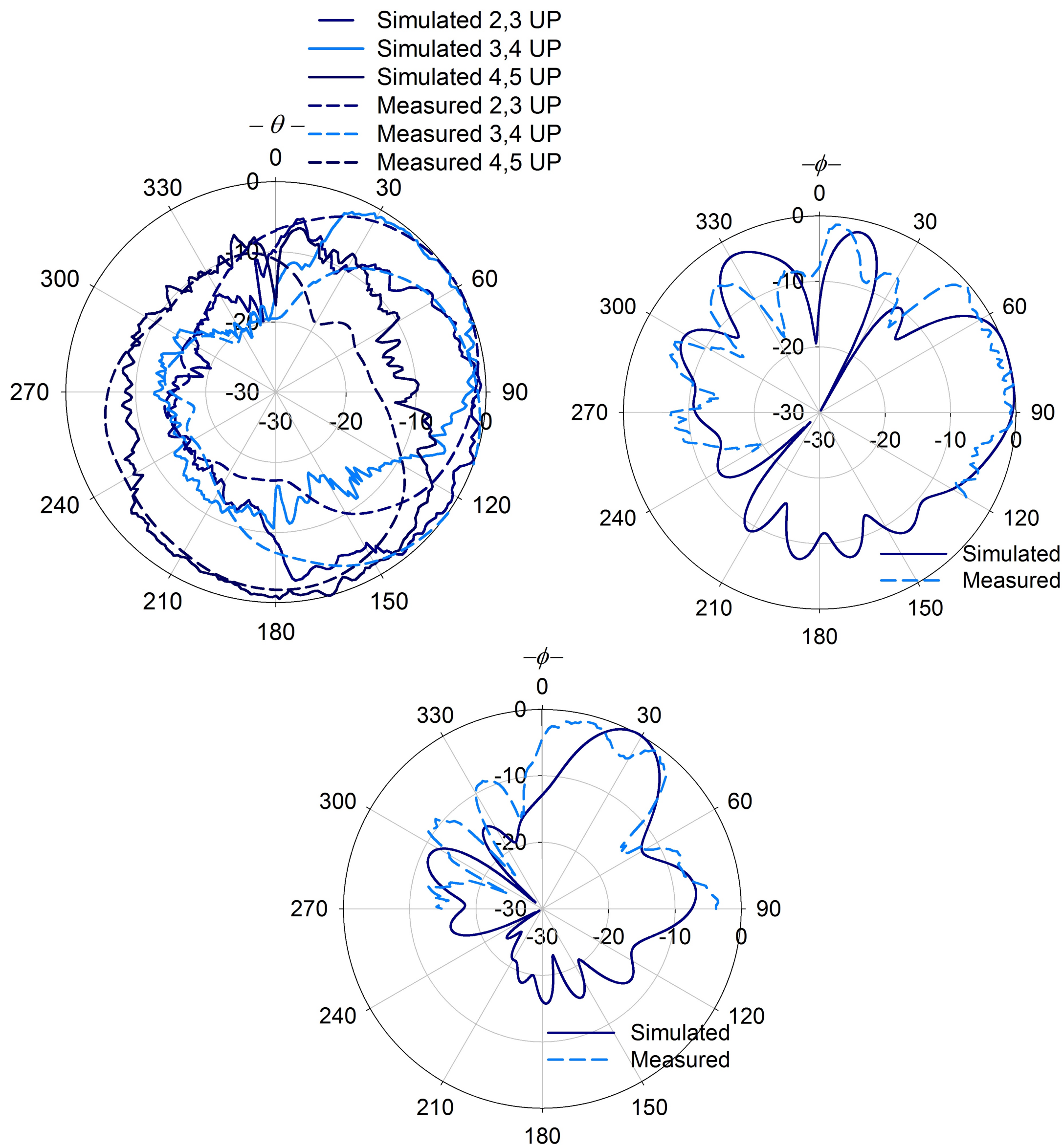

Figure 7.12 – Comparison of simulated and measured normalized radiation patterns of beam-switching antenna (a) Azimuth plane (b) Elevation plane(lower)(c) Elevation plane(upper)

Further, the radiation pattern of the beam-sweeping antenna was measured for each case, and the results at 30 GHz are shown in Figure. 7.12. The azimuth plane patterns shown in Figure. 7.12(a), compares the measured patterns with the simulated radiation patterns at $\theta = 90°$ for three cases with the lower segment in UP state, to obtain a beam-sweeping in an angular resolution of 60°. In Figure. 7.12(b) and (c), the elevation plane pattern shows the switching beams at $\phi = 0°$ and the comparison of the measured with the simulated patterns. It is evident that a beam tilt of 60° is obtained by switching the lower and upper segments. About 46° and 85° of -3 dB beamwidths are obtained in the elevation and azimuth plane, respectively.

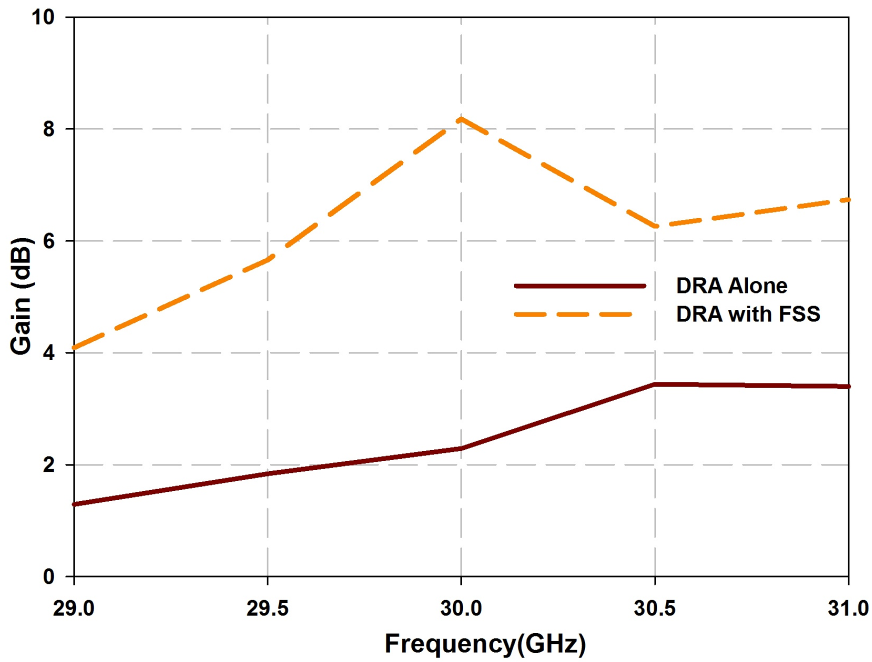

Figure 7.13 – Comparison of measured gain of the DRA with and with out the FSS panels

The measured and simulated gains of the antenna in the band of frequency are shown in Figure. 7.13. After the placement of the FSS panels around the DRA, the opaque FSS panels act as a parabolic reflector [14] and reflect the incident waves towards the transparent FSS panels. Thus, the beamwidth of the radiation pattern is decreased due to the combined reflections of FSS and ground plane to a particular direction enhances the gain of the antenna.

7.6 Conclusion

In this chapter, a beam-sweeping dielectric resonator antenna, which can sweeps beams in both elevation and azimuth planes has been presented. The reconfigurable cantilever enabled FSS panels have been used as an active screen for beam-sweeping. The proposed antenna with FSS has been designed and fabricated and measured at 30 GHz. In the elevation plane, two angles of sweeps at 30° and 90° have been obtained. Similarly, in the azimuth plane, six sweeps cover the whole 360°. As compared with the omnidirectional source DRA, a gain enhancement of 6 dB has been observed. With these features, this antenna can be a good candidate for millimeter-wave base-station communications.

Chapter 8

Conclusion and Future Research work

8.1 Conclusion

In this thesis, the applications of frequency selective surfaces in reconfigurable antennas have been investigated. The main objective of the work has to design a novel frequency selective surface for the beam-switching applications at millimeter-wave frequency bands. As an initial work of application of FSS in millimeter-wave, a wideband FSS for shielding and MIMO applications has been designed. Further, the novel cantilever enabled reconfigurable FSS has been designed. Using the cantilever FSS designs, a single plane and double plane beam-switching antennas have been designed for millimeter-wave applications. For the accomplishment of the aforementioned goals, a stepwise design methodology has been followed in this thesis, which is concluded as follows.

In the initial step, an extensive study of frequency selective surfaces for the modern antenna applications has been performed. This confirms the contribution of reconfigurable frequency selective surfaces in the future antenna millimeter-wave applications. As a commencement, a wideband FSS with dual resonating structures for MIMO and shielding applications has been designed. Further, this FSS wall has been used for mutual coupling reduction in a DRA MIMO system of DRAs. This work gave an in-depth vision of the millimeter-wave antenna system and their measurement techniques. These investigations have resulted in the publications shown in [68, 9].

As the next step, we have introduced a novel reconfigurable FSS using cantilever switches for antenna applications. Compared with the other kind of switches used in the FSS, this switch shows better performance and feasibility for fabrication. For the validation of the designed prototypes of the cantilever enabled FSS in lower frequency and in millimeter-wave band, waveguide method and free-space method has been used respectively. These investigations result in the publications shown in [62, 69, 70].

Then, two kinds of beam-sweeping antennas have been designed using the aforementioned FSS at millimeter-wave band. A beam-switching dielectric resonator antenna using hexagon shaped cantilever enabled FSS panel has initially been designed for azimuth plane beam-switching. The cantilever enabled FSS designed for this antenna has been inspired from the *supershaped* structures. For the validation of the proposed design of cantilever enabled FSS, a conceptual model of switching has been used. The results obtained have demonstrated that the switching beam in the azimuth plane can cover the whole azimuth plane with 60° angle. This investigation has resulted in the publication shown in [71].

Finally, a novel kind of reconfigurable antenna with dual plane beam-sweeping using cantilever enabled FSS has been presented. Along with the azimuth plane switching, elevation plane switching has also been achieved. Comparing to the *supershaped* FSS, the use of wide cantilever beams has provided miniaturization of the unit cell and hence more unit-cells have been used horizontally to obtain switching in the elevation plane. The results demonstrated shows freedom of beam-sweeping in the elevation plane, compared with the previous prototypes, which has made the antenna more feasible. This investigation has resulted in the publication shown in [72] [73].

8.2 Future Research work

The research work performed in this thesis as part of the doctoral course opens a new window in the reconfigurable FSS and their applications in antenna domain. However, it is observable that there are many other investigations to be explored in this area which give way for future research possibilities as explained in the following paragraphs.

Firstly, different shapes of the FSS can be explored with cantilever enabled switches to obtain FSS having better characteristics of a wide/narrow selection of bands, with high isolation of switching and low loss properties. For example, there are various *supershaped* designs which can be explored for various periodic array resonating structures. The realization of switching of cantilever beam enabled FSS with voltage can possible using other fabrication methods such as LTCC technology, which can help to design fully controllable cantilever enabled FSS. Furthermore, dual/triple-band beam switching antenna by using dual/triple-band cantilever enabled switches can be realized as mentioned in [26, 74], with better beam-switching performances. On the other hand, this cantilever enabled switching technology can be used in other RF components like phase shifters, amplifiers and couplers at millimeter-wave frequency band.

Chapter 9

Résumé

9.1 Introduction

Dans ce chapitre, un résumé du travail effectué dans le cadre de ma thèse de doctorat est présenté. Initialement, la motivation et les objectifs de ce travail sont expliqués. En outre, les solutions proposées dans mon travail sont discutées. Enfin, les conclusions avec mes contributions du travail de recherche et les travaux futurs sont également présentées.

9.1.1 Motivation

Comme l'avancement dans les systèmes de communication sans fil modernes, des fonctionnalités diversifiées comme la transmission de données élevées, la polarisation ou la diversité spatiale, les opérations multi bandes, plus de versatilité et à faible coût confinées dans l'unité individuelle sont disponibles pour la communauté. Tout au long du développement, des différentes technologies ont ete ajoutées à l'amélioration de la qualité des systèmes de communication. Le confinement de toutes ces unités unitaires rend les systèmes intelligents plus adaptés aux applications militaires et industrielles. Les systèmes de communication intelligents comprennent le développement de modules de réception et d'unités de traitement. Comme le système d'antenne joue un rôle important dans les modules de réception et de transmission, il est également transformé en configurations multifonctionnelles. À cet égard, l'intégration de plusieurs unités d'antennes fournit de meilleures performances des systèmes de communication.

En raison des faits mentionnés ci-dessus, les antennes reconfigurables ont attiré beaucoup d'intérêt parmi les chercheurs depuis quelques décennies. Les caractéristiques les plus communes de ce type d'antennes sont la reconfigurabilité dans les fréquence, de polarisation et faisceaux de rayonnement qui ne peuvent rendre que des fonctions multiples mais aussi améliorer l'efficacité spectrale et réduire les détériorations des canaux. De nombreuses approches électroniques et mécaniques sont utilisées avec ces antennes reconfigurables pour obtenir diverses caractéristiques.

Au cours des dernières années, les bandes millimétriques ont attiré l'attention des chercheurs. Ils ont le potentiel de répondre aux exigences des nouveaux systèmes et applications de communication. En outre, la grande vitesse, la bande passante, les systèmes et les applications à grande capacité, la facilité d'intégration d'antennes compactes et à haut rendement font de cette bande un choix approprié pour les communications sans fil gigabit, les capteurs d'imagerie, les radars automobiles et les communications spatiales. Cependant, il existe certains obstacles dans le déploiement de la technologie des ondes millimétriques. L'un est le taux d'atténuation élevé dû à la perte de trajet étant donné que la longueur d'onde à 60 GHz est proche de 5 mm. L'atténuation due à l'absorption d'oxygène qui est également significative dans cette bande de fréquence. Du fait de la compacité des systèmes à réseau d'antennes d'ondes millimétriques, le couplage mutuel entre les éléments rayonnants peut affecter négativement les performances de l'antenne. Afin d'améliorer les caractéristiques du système et réduire ces problèmes, des antennes reconfigurables peuvent être utilisées.

Les structures périodiques sont largement utilisées avec les antennes pour une variété d'applications en raison de leurs caractéristiques électromagnétiques. Elles sont largement classées en métamatériaux, structures à bande interdite électromagnétique (BIE) et structures sélectives en fréquence (SSF). Les métamatériaux sont de nouveaux matériaux avec des propriétés électromagnétiques inhabituelles et BIE et SSF sont des filtres spatiaux pour les ondes incidentes. Les structures BIE fonctionnent dans tous les angles de polarisation de l'onde tandis que les SSF se limitent seulement à des angles spécifiques. Le BIEs possèdent des propriétés de bande interdite électromagnétique et peuvent diriger les ondes dans les structures périodiques défectueuses qui servent à réduire les ondes de surface des antennes. Elles peuvent être également utilisées comme conducteur magnétique ou de surface haute impédance avec des plans de masse pour les antennes discrètes.

Comme nous l'avons déjà mentionné, les surfaces sélectives en fréquence, les antennes reconfigurables et les ondes millimétriques nous ont motivés à effectuer une recherche approfondie sur les applications du SSF pour les antennes en ondes millimétriques. En conséquence, cette thèse vise à la conception, la fabrication et l'implantation de nouvelles SSF large bande pour les applications dans le blindage et des antennes reconfigurable à balayage électronique. En outre, deux antennes de commutation de faisceau sont introduites en utilisant des structures SSF reconfigurables à 30 GHz.

9.1.2 Identification du problème et objectifs de recherche

En raison de leur caractéristique du filtrage spatial des ondes électromagnétiques incidentes sur la surface, les surfaces sélectives en fréquence ont obtenu une immense attraction parmi les chercheurs dans le domaine des antennes. Par la suite, elles sont utilisées pour les antennes reconfigurables en tant que surfaces actives pour contrôler la direction du faisceau d'antenne, et la polarisation. Dans cette thèse, une SSF double couche à large bande est introduite pour la réduction du couplage mutuel en fréquence millimétrique. En outre, un nouveau type de SSF reconfigurable utilisant des commutateurs à cantilever est conçu dans la bande de fréquence de 30 GHz. Ces SSF sont utilisées pour convertir une source omnidirectionnelle en une antenne à commutation de faisceau directionnelle. Il est important de mentionner que les structures de commutation actives utilisées peuvent être fabriquées à faible coût par rapport aux composants actifs coûteux dans la bande de fréquence en ondes millimétriques.

Plus précisément, les objectifs de cette thèse sont la conception d'une SSF large bande pour la réduction de couplage mutuel dans les systèmes MIMO et la conception de SSFs reconfigurables utilisant des commutateurs à cantilever pour concevoir des antennes à commutation de faisceau sur une bande de fréquence millimétrique. La SSF à large bande a atteint une efficacité de blindage supérieure à 16 dB et une bonne isolation de -20 dB dans un système MIMO à une fréquence de 60 GHz. Deux antennes à commutation de faisceaux pour les opérations à un seul plan et à deux plans sont conçues à l'aide de panneaux SSF à 30 GHz activés en cantilever, qui sont essentiellement une nouvelle antenne à commutation de faisceaux pour une application à ondes millimétriques.

9.2 Surfaces Sélectives un Fréquence millimétriques et large bande

Dans cette partie, une SSF large bande simple-couche est proposée. Elle a une large bande passante de 30 GHz (de 40 GHz à 70 GHz) et une bande passante fractionnaire de 54,5% par rapport à la fréquence centrale (55 GHz). Par rapport aux travaux précédemment rapportés dans la gamme des ondes millimétriques, la structure proposée a une bande passante plus large et la taille de la cellule unitaire est aussi miniaturisée ($0,34\lambda \times 0,34\lambda$). En modifiant les paramètres du SSF, la bande passante et les fréquences de résonance peuvent être contrôlées. Un panneau de cellules unitaires 40×40 a été fabriqué, et les résultats ont été comparés aux résultats simulés. Cette SSF peut être utilisée comme dispositif de protection efficace et comme élément de réduction du couplage mutuel dans les régions des bandes U et V des fréquences millimétriques. En outre, le mur SSF proposé a été inséré entre deux AD pour réduire le couplage mutuel dû au rayonnement de l'espace libre. Pour réduire le courant de surface entre les deux antennes, deux fentes de taille différente ont été gravées dans le plan de masse commun de la structure.

9.2.1 Conception et principe de la SSF

La Figure 9.1 montre la géométrie simple-couche de la cellule unitaire SSF avec la croix de Jérusalem classique (J-croix) et la forme FAN gravée sur les deux côtés du substrat RO4003. La périodicité de la cellule unitaire est de 1,9 mm dans les directions x et y. L'épaisseur du substrat de Rogers utilisé est de 0,508 mm et sa constante diélectrique est de 3,55 avec une tangente de perte de 0,0027. J-croix et la forme FAN constituent des bandes rectangulaires de largeur 0,5 et 0,2 mm, respectivement. Chaque bras de la cellule J-croix a une longueur de 0,623 mm et se termine par un bras perpendiculaire de 0,75 mm de longueur. Le rayon de la boucle et la longueur du bras de la forme FAN sont 0,375 mm et 1,325 mm, respectivement.

Le formée FAN et J-croix sont conçues pour résonner aux fréquences supérieure et inférieure, respectivement, qui sont combinées pour former une large bande non passante du SSF proposée. La structure en croix fournit une structure miniaturisée pour la forme SSF et FAN, qui peut être considérée comme une boucle chargée, fournissant une bonne bande passante, et sa fréquence de résonance peut être ajoutée en variant les charges et le rayon de la boucle [54].

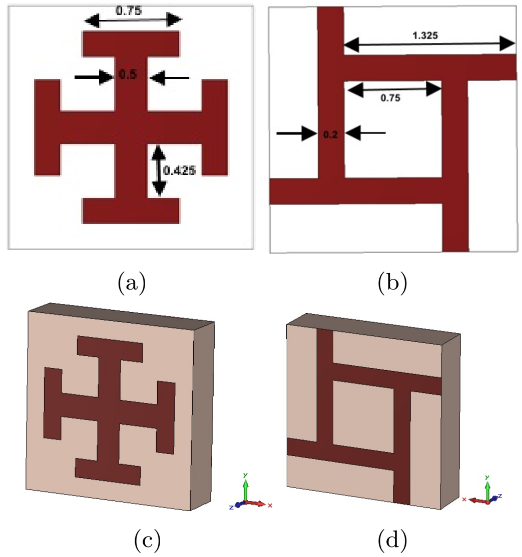

Figure 9.1 – (a) J-croix sur la surface supérieure. (b) Forme FAN sur la surface inférieure. Vues en perspective de la cellule unitaire (c) face et (d) arrière (dimensions en mm).

9.2.2 Résultats et discussion

Dans la phase initiale, la cellule unitaire SSF monocouche a été simulée à l'aide de CST Microwave Studio [55] pour obtenir les résultats de transmission et de réflexion. La forme J-cross résonne à une fréquence de 48 GHz, et la forme du FAN résonne à 60 GHz, lorsque chacune de ces structures est simulée seule. La Figure. 9.2 montre clairement comment les deux résonances de la structure SSF sont combinées pour obtenir une large bande passante de 30 GHz dans la bande 40-70 GHz. Les résonances de chaque structure SSF se sont légèrement décalées lorsque les deux sont combinées, c'est à cause du couplage mutuel entre elles.

Pour valider les résultats simulés, la SSF proposée a été fabriquée en utilisant le substrat RO4003 de 95 $\times$ 95 mm^2 dimensions. Le prototype du SSF fabriqué est représenté à la Figure. 9.3. Environ 40 cellules unitaires sont disposées dans le plan xy pour former un panneau SSF. La configuration de mesure en espace libre est utilisée pour obtenir les caractéristiques de transmission du SSF. En raison de la non disponibilité de l'antenne standard fonctionnant dans cette large bande passante de 30 à 80 GHz, deux antennes à cornet pyramidal symétriques fonctionnant dans la bande de fréquence de la bande V avec un gain de 24 dBi sont utilisées dans le montage de mesure. Le panneau SSF est placé entre les antennes cornet à l'aide d'un porte-prototype. Un analyseur de réseau, Agilent PNA N5247A, courant la bande de 10 MHz à 67 GHz, est utilisé. Les paramètres sans le panneau SSF sont mesurées au début pour obtenir les résultats étalonnés. En utilisant un système de rotation

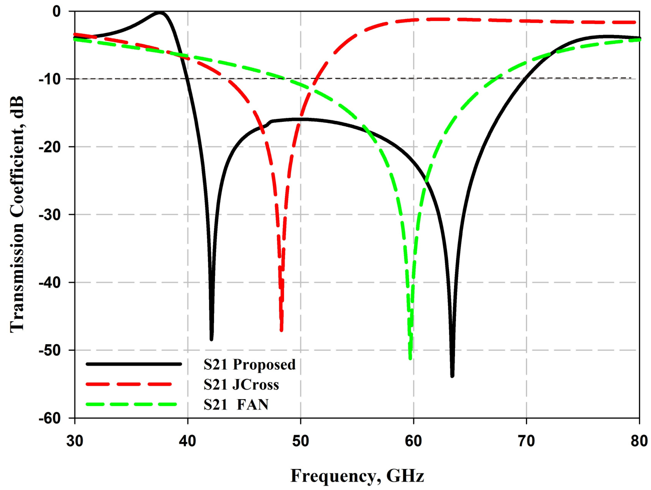

Figure 9.2 – Comparaison des coefficients de transmission de la forme en J-croix et en FAN avec le SSF proposé.

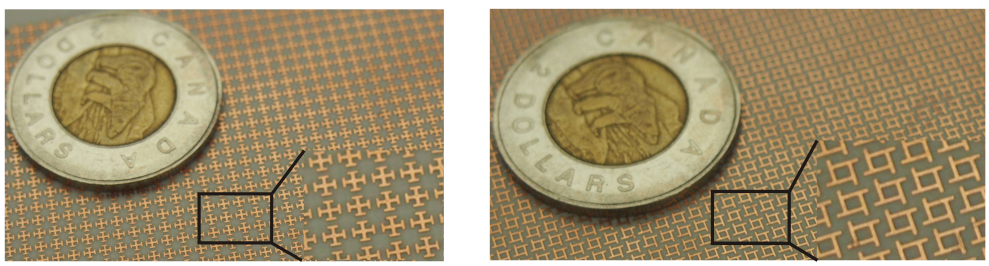

(a) (b)

Figure 9.3 – Prototype fabriqué de SSF avec vue agrandie (a) J-croix sur la surface supérieure. (b) FAN forme sur la surface inférieure.

mécanique, le prototype est tourné dans différents angles d'incidence pour la mesure des modes TE et TM. Les comparaisons entre les résultats simulés et mesurés pour les polarisations TE et TM sous différents angles d'incidentes sont présentées à la Figure. 9.4. Il ressort des comparaisons que les résultats mesurés concordent bien avec les résultats simulés. Les légères variations des fréquences de résonance sont dues aux réflexions de bord et à la diffusion des ondes EM pendant les mesurée. Lorsque l'angle d'incidence change, la large bande passante est légèrement affectée par la génération de lobes. Ces lobes de réseau peuvent être réduits en diminuant le chargement de la forme FAN, mais cela réduit l'atténuation dans toute la bande de fréquence. L'efficacité du blindage (EB) est définie comme le rapport entre l'amplitude du champ électrique incident sur la surface et le champ électrique transmis à travers la surface. Puisque le champ incident est plus grand que le champ sort de la surface, la valeur du EB est toujours positive [56]. En utilisant les valeurs des paramètres S

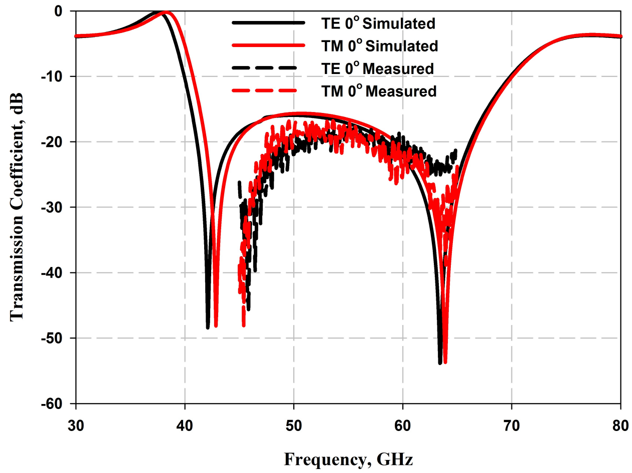

Figure 9.4 – Comparaison des coefficients de transmission des résultats simulés et mesurés pour les modes TE et TM avec incidence normale.

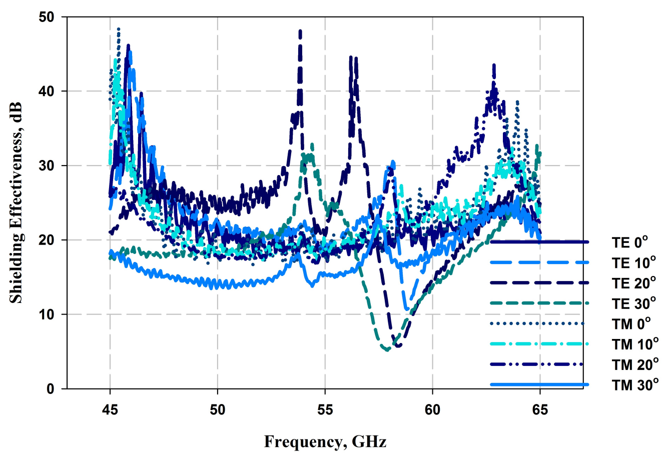

Figure 9.5 – EB mesuré pour les modes TE et TM avec différents angles d'incidence.

obtenues à partir de la mesure, le EB peut être calculé comme suit [57]:

$$EB_{dB} = S_{21,\ sans\ SSF} - S_{21,\ avec\ SSF} \tag{9.1}$$

où $S_{21,\ sans\ SSF}$ est le coefficient de transmission de l'antenne sans la SSF et le $S_{21,\ avec\ SSF}$ est le coefficient de transmission avec la SSF. La EB mesurée pour les modes TE et TM pour différents angles d'incidence est donnée à la Figure. 9.5. On constate qu'une valeur EB élevée est obtenue pour tous les angles d'incidence, mais la bande passante est réduite pour les angles d'incidence obliques dus aux lobes de réseau et aux champs frangeants.

9.2.3 Application de la SSF proposée comme mur de réduction à couplage mutuel

En application, le mur SSF proposé a été inséré entre deux antenne diélectrique (AD) pour réduire le couplage mutuel dû au rayonnement d'espace libre. Pour réduire le courant de surface entre deux antennes, deux fentes de taille différente jouant le rôle de résonateur LC ont été gravées à partir du plan de masse commun de la structure. Une étude paramétrique a été réalisée pour expliquer l'effet des deux créneaux. Un prototype de la structure a été fabriqué et mesuré. L'isolation, meilleure que -30 dB, a été obtenue en utilisant un mur et des fentes FSS. Un coefficient de corrélation d'enveloppe supérieur à 5e-6 et une efficacité élevée font de cette antenne un bon candidat pour l'application du système MIMO aux fréquences millimétriques.

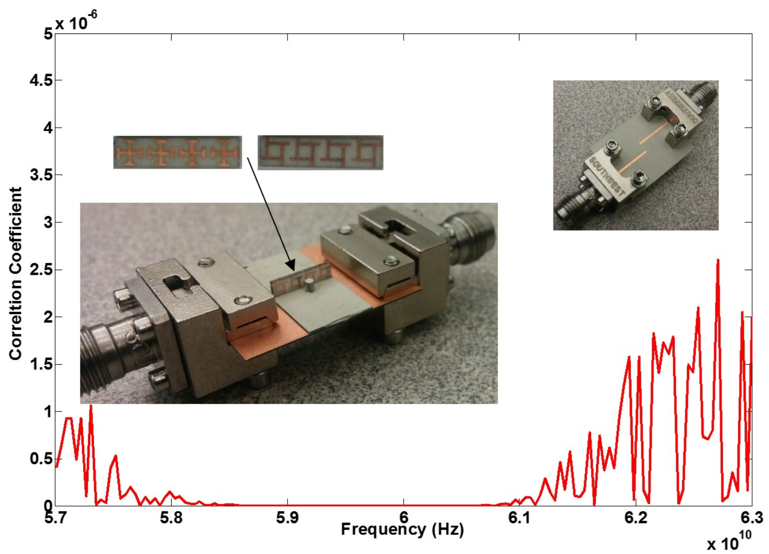

Figure 9.6 – Résultat de mesure pour le coefficient de corrélation entre deux antennes avec le prototype fabriqué de l'antenne proposée[9]

9.3 SSF active basée sur des commutateurs cantilever

Comme mentionné dans le chapitre 2, les structures périodiques sont intégrées avec des éléments actifs pour obtenir une reconfigurabilité de leurs caractéristiques EM. À cet égard, une structure SSF est incorporée avec des composants actifs tels que les diodes pin [14, 15, 16, 17, 18], les diodes varactor [4] et les commutateurs MEMS [19, 20], ses propriétés de résonance peuvent être variés. Cependant, les commutateurs à diodes ont des pertes, et les réflexions provenant des réseaux de polarisation peuvent réduire les performances globales de l'antenne. Similaire aux diodes pin, les commutateurs MEMS sont également utilisés dans la SSF pour obtenir une reconfigurabilité. Dans [19], les commutateurs MEMS sont implémentés dans la SSF reconfigurable. Dans la plupart des travaux, les commutateurs MEMS sont utilisés comme charges capacitives sur une ouverture pour la reconfigurabilité de la SSF. Cependant, la variation de capacitance des commutateurs MEMS est très faible en raison de la petite taille et le coût de fabrication est également très élevé.

Les commutateurs usinés au laser peuvent surmonter ces problèmes [58]. La comparaison avec les diodes pin et les MEMS permet de mieux détecter les pertes et les variations capacitives dans ces commutateurs. En effet, la facilité de fabrication et le besoin de réseau, font de ce type de SSF un meilleur candidat pour toutes les applications d'alimentation pour les antennes à commutation de faisceau aux ondes millimétriques.

Les objectifs de la thèse sont basés sur l'application de ce type de SSF pour les antennes à commutation de faisceau.

9.3.1 Conception de SSF activée en cantilever

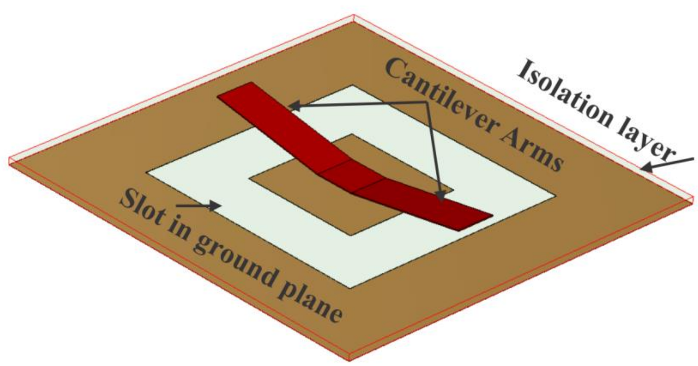

(a)

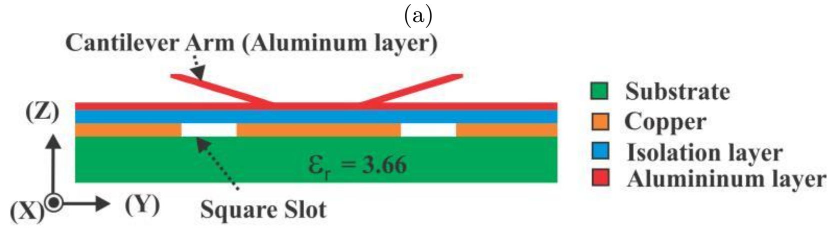

(b)

Figure 9.7 – Schéma de SSF activée en cantilever (a) Mise en page (b) Vue de côté

La conception des SSF en cantilever consiste essentiellement en deux couches métalliques isolées en continu, le plan de masse statique inférieur avec une fente et les bras mobiles en cantilever supérieurs. Le principe de fonctionnement de base pour les caractéristiques reconfigurables de la structure est que les bras mobiles en cantilever chargent de manière capacitive la fente et changent sa fréquence de résonance. La Figure 9.7 (a) montre la disposition d'une cellule unitaire active du SSF composée d'une fente carrée et de deux bras mobiles en cantilever. Une première fréquence de résonance d'état en cantilever HAUT du SSF est définie en premier. En appliquant une tension continue suffisante entre les deux couches, les bras en cantilever sont attirés vers le plan de masse et vers le bas jusqu'à la couche d'isolation diélectrique. Cela modifie la capacité, et donc la fréquence de résonance de la structure SSF se décale. La figure 9.7 (b) montre une vue latérale de la structure de cellule unitaire active du SSF, où quatre couches de la structure de cellule unitaire sont décrites. La géométrie de la boucle est réalisée sur un stratifié à haute fréquence qui sert de structure de support pour la SSF. Une mince feuille d'aluminium ou d'acier inoxydable peut être utilisée pour concevoir la couche supérieure qui maintient les bras en cantilever. Pour isolation de courant continu (CC) les deux couches métalliques aux bras en cantilever; une couche très mince d'un diélectrique est utilisée.

9.3.2 Processus de fabrication

La fabrication des structures SSFs proposés est effectuée par divers processus. Pour la couche inférieure de la SSF, les substrats Roger haute fréquence tels que RO4003, R6002 sont principalement utilisés. Les structures en boucle résonantes sur la surface supérieure du stratifié de cuivre sont gravées et la surface inférieure est laissée exempte de cuivre comme le montre la Figure 9.8(a). En outre, la couche de métal supérieure est découpée dans la feuille d'aluminium ou la cale d'acier inoxydable d'une épaisseur de 5 *mil*. Tous les procédés de gravure et de découpe sont réalisés à l'aide d'une machine laser LPKF Protolaser. Les bras en cantilever de chaque cellule du panneau SSF sont courbés vers le haut à une hauteur optimisée en utilisant le faisceau laser. Il est effectué en chauffant les articulations entre les bras en cantilever et le corps principal de la table de lecture en utilisant précisément le laser. La couche supérieure fabriquée est représentée à la Figure 9.8 (b).

La couche d'isolation entre les couches métalliques est réalisée en utilisant une fine couche de peinture émail. Une mince couche de peinture émail est pulvérisée uniformément sur la surface

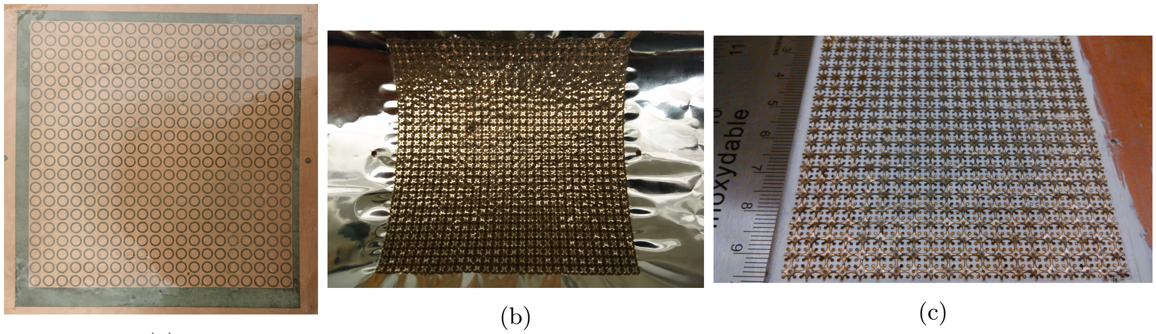

(a) (b) (c)

Figure 9.8 – Prototype fabriqué de (a) couche de stratifié de cuivre (b) couche de métal supérieure

supérieure de la couche de cuivre. Avant de pulvériser la peinture, la partie centrale de la structure de fente est masquée, de sorte que cette partie sera exempte de couche d'isolation. Après le durcissement de la peinture, les masques sont enlevés et la couche de métal supérieure est placée par-dessus. La partie centrale de la couche active de chaque cellule unitaire est soudée à la partie circulaire de la fente gravée sur la couche de cuivre. Le prototype final de la structure fabriquée du panneau SSF est représenté à la Figure 9.8(c).

9.3.3 Méthodes de mesure

Pour la caractérisation des prototypes SSF, deux méthodes sont utilisées ici, la méthode du guide d'onde et la méthode de mesure en espace libre. Principalement, les paramètres S de la SSF sont mesurés en utilisant deux ports de l'analyseur de réseau Agilent 8277ES. Les SSF activés en cantilever proposés ici sont des SSF passe-bande, de sorte que la mesure des coefficients de transmission est effectuée.

Pour valider le principe de fonctionnement de la SSF en cantilever, des prototypes à la fréquence de la bande X sont fabriqués et mesurés. La méthode de mesure du guide d'ondes est utilisée pour la caractérisation de ces prototypes SSF dans la bande X [59].

Une cellule unitaire de la SSF proposée est conçue pour la fréquence de la bande X. Toutefois, les paramètres d'espace libre de la cellule unitaire SSF sont légèrement modifiés pour s'adapter à l'effet de l'environnement du guide d'ondes. La conception de la périodicité de la SSF peut être perturbée par les côtés du guide d'ondes lorsque la théorie de l'image est appliquée. Afin d'éviter

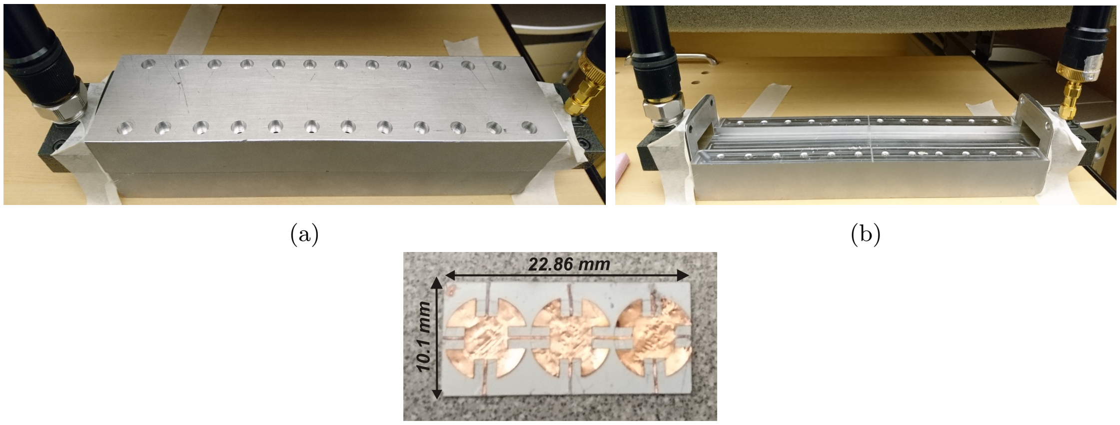

(a) (b) (c)

Figure 9.9 – Configuration de la mesure du guide d'ondes à l'aide du guide d'ondes WR90 (a) fermé (b) ouvert (c) prototype

cette perturbation, la période de la SSF est modifiée, de sorte que les plans de symétrie de la SSF reposent sur les murs.

Pour la mesure du prototype SSF, une structure de guide d'ondes de $WR90$ est fabriquée comme indiqué à la figure. 9.9 (a)-(b). La structure de guide d'ondes à deux extrémités présente des transitions coaxiales de guide d'ondes à coaxial pour la connexion aux deux ports de l'analyseur de réseau. Le guide d'ondes est fabriqué de manière à avoir deux hémisphères, en haut et en bas, pour le placement du prototype SSF à l'intérieur. Les prototypes SSF avec deux cellules unitaires de la conception proposée, sont testés à l'intérieur du guide d'ondes comme indiqué à la figure. 9.9 (c). La taille du prototype est mise à l'échelle à 22.86 $mm \times 10.16$ mm pour le placement à l'intérieur du guide d'ondes.

La configuration de mesure en l'espace libre est utilisée pour la caractérisation des panneaux SSF en ondes millimétriques. Dans cette configuration de mesure, deux antennes cornet standard

(a) (b)

Figure 9.10 – Configuration de mesure d'espace libre (a) avec panneau SSF (b) sans panneau SSF

pyramidales symétriques fonctionnant en bande Ka avec un gain de 18 dB sont utilisées (voir Figure 9.10). Les caractéristiques de transmission du panneau SSF, qui est maintenu entre les antennes cornet à l'aide d'un porte-prototype, sont mesurées. Les coefficients de transmission des antennes cornet sans le panneau SSF sont mesurés initialement pour obtenir les résultats étalonnés.

9.4 Antenne à commutation de faisceaux en ondes millimétriques

Une antenne à commutation de faisceaux pour les applications en ondes millimétriques à 30 GHz est présentée dans cette section. La reconfigurabilité de rayonnement pour une antenne à résonateur diélectrique cylindrique (AD) est obtenue en utilisant une surface sélective en fréquence activée en cantilever. La SSF à cantilever proposée offre des performances de band-pass et de band-rejet reconfigurables avec une bonne isolation. L'étude de la SSF conçue est réalisée à l'aide d'une simulation électromagnétique et un ensemble de cellules unitaires SSF est fabriqué et mesuré en utilisant la méthode de mesure en espace libre, ce qui montre un bon accord avec les résultats de la simulation. Enfin, six panneaux du réseau 1×5 de la SSF reconfigurable proposées sont disposés dans une configuration hexagonale autour d'un AD cylindrique pour obtenir un diagramme de rayonnement reconfigurable dans le plan azimutal. Un prototype de l'antenne diélectrique reconfigurable est fabriqué, et les diagrammes de rayonnement de commutation sont mesurés à 30 GHz.

9.4.1 Conception SSF proposée en cantilever

La Figure 9.11 montre la structure schématique de la cellule unitaire SSF, qui est constituée de quatre couches. La couche inférieure est constituée d'un substrat avec constante diélectrique de 3,55, au-dessus de laquelle une couche de cuivre est placée. La composante résonnante de cette bande passante SSF est une fente circulaire de rayon $R = 1,6\ mm$ et de largeur $T = 0,4mm$ gravée sur la couche de cuivre. La forme de la couche supérieure est inspirée de la structure *supershaped*, où une grande variété de formes géométriques peuvent être générées en utilisant le *superformula* [64]. Cette couche supérieure est faite d'acier inoxydable, ayant quatre bras cantilever et quatre lignes de connexion. Les deux couches métalliques sont séparées en utilisant une fine couche diélectrique agissant comme une couche d'isolation. La périodicité L de la cellule unitaire est de 3.7 mm.

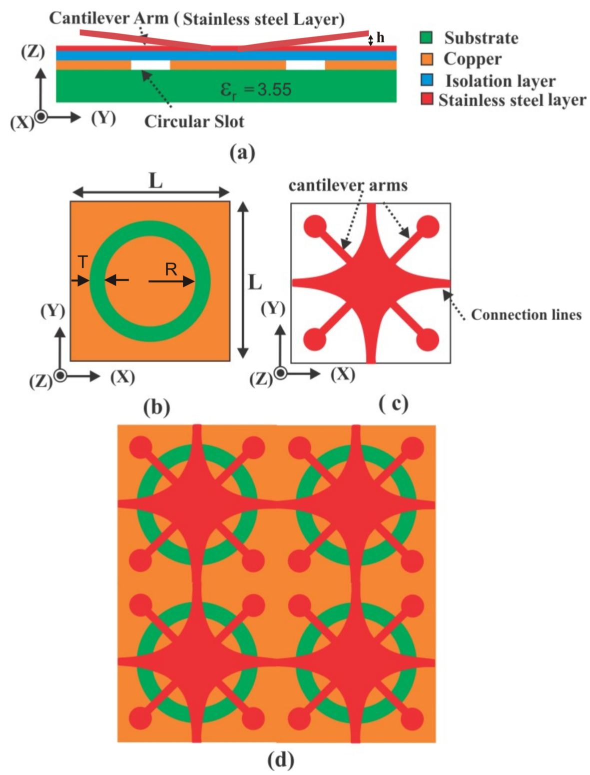

Figure 9.11 – Schéma de la SSF proposée (a) Vue de côté (b) Couche de cuivre inférieure (c) Couche supérieure en acier inoxydable (d) Réseau SSF

Les quatre bras en cantilever sur la couche supérieure en acier inoxydable agissent comme des interrupteurs actifs. Puisque les deux couches métalliques sont isolées par une substance diélectrique au niveau des bras en cantilever, il existe une charge capacitive qui modifie la fréquence de résonance de la cellule unitaire. Les mouvements ascendants et descendants des bras en cantilever font varier la capacité équivalente de la fente sur la couche de cuivre, fournissant ainsi des caractéristiques de reconfigurabilité de fréquence à la cellule unitaire SSF. La hauteur h de flexion vers le haut des bras en cantilever est optimisée à $h = 0,1\ mm$, pour obtenir une résonance à la fréquence de fonctionnement désirée. Afin d'étudier la commutation de fréquence, deux types d'unités SSF sont simulés, les bras en cantilever dans la position ascendante (état HAUT) et dans la position descendante (état BAS).

La réalisation de la SSF basée sur le cantilever est faite en fabriquant une matrice $40 \times 40\ mm^2$ sur le substrat RO4003C comme couche inférieure. Afin de prouver le concept de la conception proposée, les panneaux d'état HAUT et BAS sont fabriqués. Le panneau SSF fabriqué, tel que représenté à la Figure 9.12, est mesuré en utilisant la méthode de l'espace libre. Deux antennes à pavillon standard pyramidales symétriques fonctionnant en fréquence Ka avec un gain de 18 dB

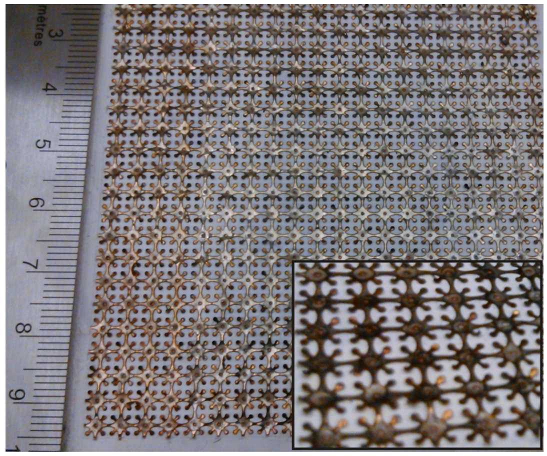

Figure 9.12 – Prototype fabriqué du SSF proposé (état HAUT) avec une vue agrandie donnée en encart

sont utilisées dans la configuration de mesure. À l'aide de l'analyseur de réseau Agilent 8277ES, les paramètres de transmission du panneau SSF, qui est maintenu entre les antennes cornet à l'aide d'un porte-prototype, sont mesurés. Pour obtenir des résultats étalonnés, les coefficients de transmission des antennes cornet sans le panneau SSF sont mesurés initialement.

La comparaison entre les coefficients de transmission simulés et mesurés est montrée à la Figure 9.13. Les résultats mesurés sont en bon accord avec les résultats simulés. Une isolation d'environ 20 dB est obtenue entre les états HAUT et BAS à la fréquence de résonance du SSF.

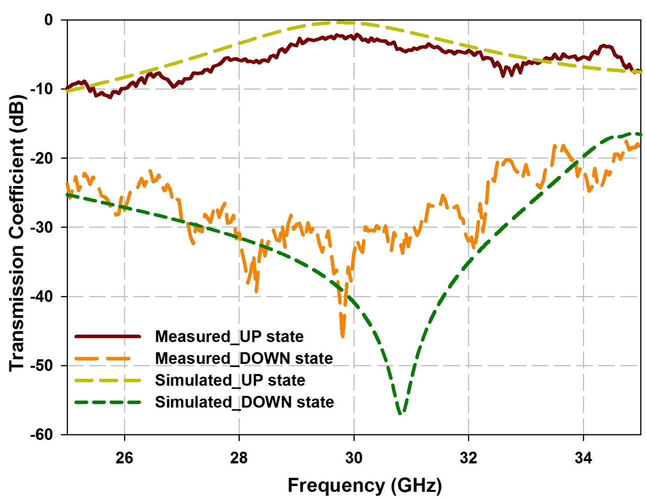

Figure 9.13 – Comparaison des coefficients de transmission simulés et mesurés pour les états HAUT et BAS

9.4.2 Antenne diélectrique à commutation de faisceau

Le SSF reconfigurable proposé dans la section précédente est intégré à une antenne à résonateur diélectrique classique pour obtenir une commutation de faisceau. L'antenne, diélectrique à commutation de faisceaux (ADCF) consistent en un résonateur diélectrique cylindrique placé sur un plan de masse et alimenté par une alimentation coaxiale comme indiqué sur la Figure 9.14 (a). Lorsque l'antenne électrique est alimentée par une alimentation monopôle coaxiale à partir du centre inférieur, le courant circulant dans le monopôle excite le mode TM_{01} dans la AD et un modèle omnidirectionnel est généré. Le rayon et la hauteur d'AD sont optimisés à 1 mm et 2,54 mm, respectivement. La AD est composée d'un matériau ayant une constante diélectrique de 10,2 et placée sur un plan de masse en stratifié RT6002 d'une épaisseur de 0,508 mm.

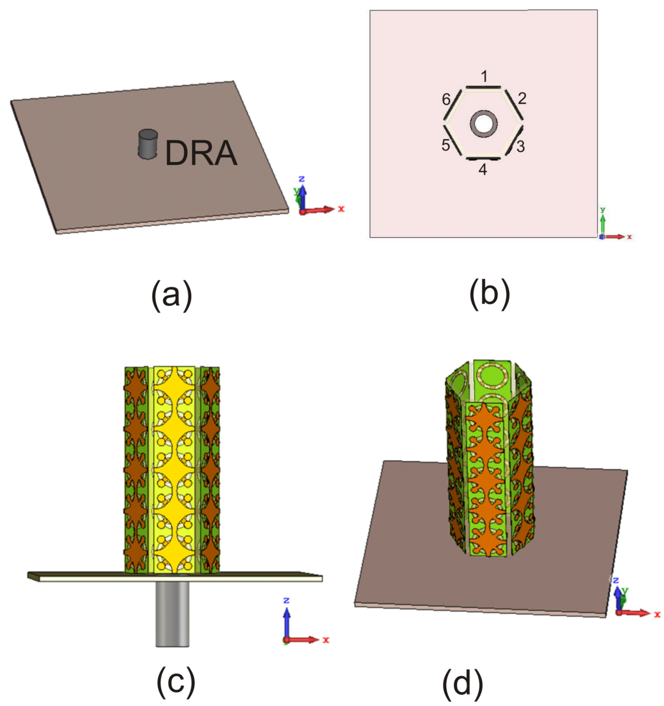

Figure 9.14 – Schéma d'AD de commutation de faisceau (a) AD seul, AD avec SSF (b) Vue de dessus (c) Vue de côté (d) Vue en perspective

Le diagramme de rayonnement omnidirectionnel de l'AD dans le plan azimutal est converti en un faisceau directif en incorporant les panneaux SSF proposés autour de celui-ci. Les rangées 1x5 de la cellule unitaire SSF activée en cantilever sont disposées en six panneaux latéraux d'une géométrie hexagonale et placées sur le plan de masse, comme indiqué à la Figure 9.14 (b)-(d). La distance radiale entre les panneaux SSF et la source est choisie comme valeur entre $0.4\lambda - 0.7\lambda$ [15], où λ est la longueur d'onde de résonance, et ici nous avons optimisé cette distance en

0.4λ parmi les six panneaux, deux panneaux consécutifs sont fixés dans l'état HAUT et les quatre panneaux restants dans l'état BAS. Étant donné que les deux panneaux d'état HAUT agissent en tant que SSF passe-bande, le rayonnement provenant de l'AD sur ces panneaux est débloqué. Au contraire, le rayonnement des panneaux d'état BAS est bloqué et réfléchi. De plus, il y a une interférence constructive des ondes rayonnées et réfléchies en phase sur les panneaux d'état BAS vers les panneaux d'état HAUT, ce qui améliore le gain de l'antenne. Comme le montre la Figure 9.16(a), en configurant l'état des six panneaux avec des configurations différentes, nous pouvons réaliser une commutation de faisceau dans six directions dans le plan azimutal.

Figure 9.15 montre le prototype fabriqué de l'antenne placée sur un plan de masse, qui est alimentée avec un connecteur coaxial de 2.92 mm (K). La AD cylindrique a été fabriquée en utilisant un substrat RT6010 avec une hauteur de 2,54 mm. Six panneaux de la SSF proposée en cantilever ont été fabriqués par la méthode mentionnée dans la section 9.4.1 et fixés sur le plan de masse à l'aide de mousses *Rohacell* $31HF$, comme le montre la Figure 9.15(b).

(a) (b)

Figure 9.15 – Prototype fabriqué (a) AD (b) faisceau-commutation AD

Après avoir placé les six panneaux SSF autour du AD, les diagrammes de rayonnement de commutation de faisceau à 30 GHz pour différentes configurations sont mesurés et comparés aux diagrammes simulés, comme indiqué à la Figure 9.16. Un bon accord entre les diagrammes de rayonnement mesurés et simulés est obtenu. La direction des faisceaux ansi qui les largeurs de faisceau des diagrammes de rayonnement de commutation mesurés est à peu près similaire à celles simulées. La présence de lobes arrière dans les motifs mesurés est due à l'imperfection de fabrication des panneaux SSF à l'état BAS.

Le Tableau. 9.1 montre les gains maximaux mesurés et simulés de la AD. En raison de l'effet de perte dans le connecteur coaxial et des tolérances de fabrication, le gain mesuré à des petites variations avec les simulations. Le Tableau. 9.2 montre la comparaison de l'antenne à commutation

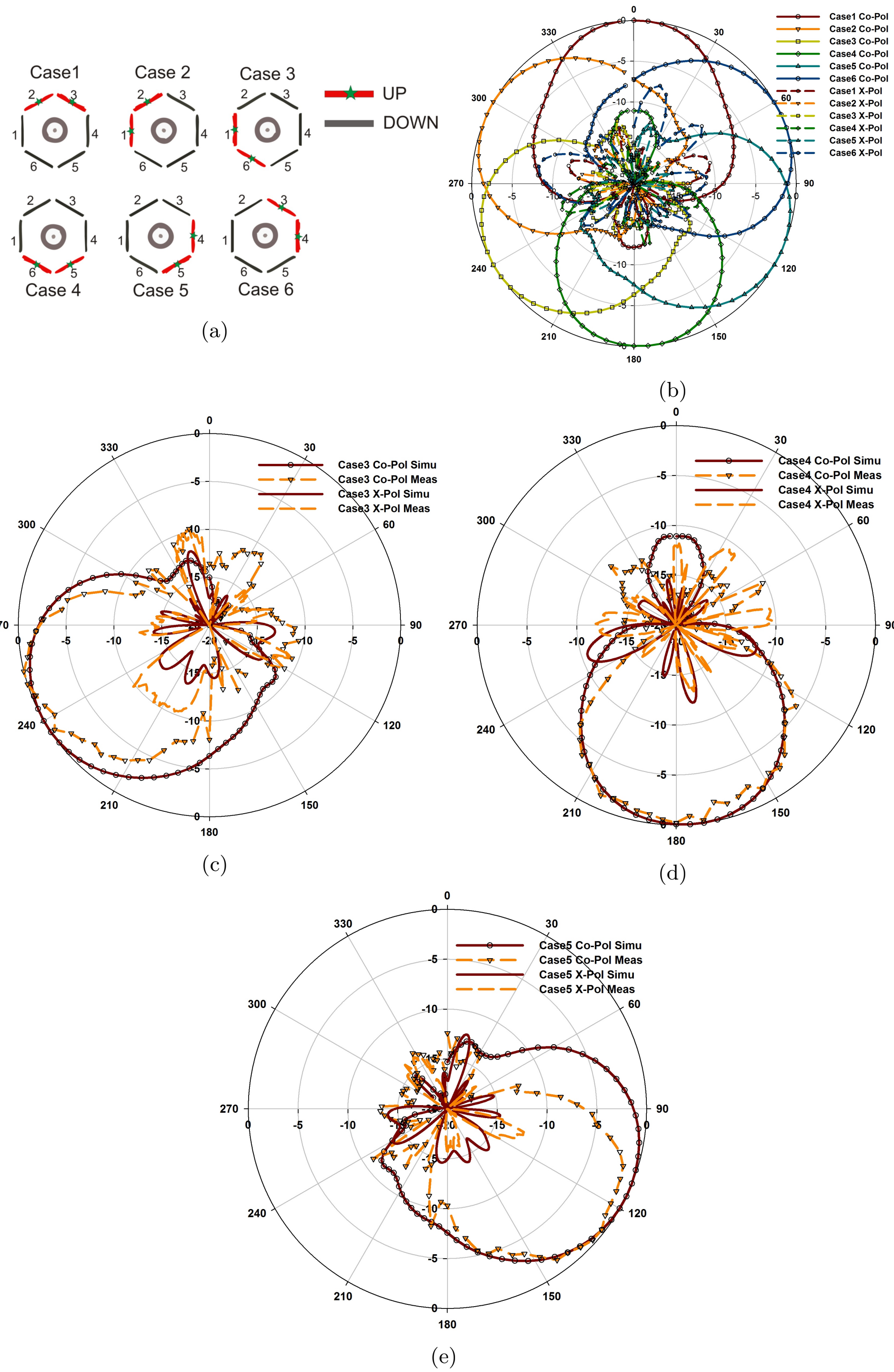

Figure 9.16 – (a) Configuration de la commutation de faisceau de l'antenne proposée pour différents cas (b) schémas de rayonnement normalisés simulés au plan azimutal. Schémas de rayonnement simulés et mesurés normalisés au plan azimutal (c) cas 3 (d) cas 4 (e) cas 5

Tableau 9.1 – Comparaison du gain réalisé simulé et mesuré du AD

	AD seul	AD avec SSF
Simulé	4.2 dB	7.2 dB
Mesuré	2.9 dB	6.1 dB

Tableau 9.2 – Comparaison de l'antenne proposée avec les travaux précédents

Les références	[14]	[22]	Proposée
La fréquence	2.45 GHz	2.4-2.5 GHz	30 GHz
Méthode de commutation	Utilisation d'une SSF cylindrique active activée par pin-diode	Utilisation d'une fente cylindrique à pin-diode activée SSF	Utilisation de SSF activé en cantilever
Dimensions	$1.3\lambda\times 1.3\lambda\times 1.6\lambda$	$1.7\lambda\times 1.7\lambda\times 1.6\lambda$	$1.5\lambda\times 1.5\lambda\times 1.8\lambda$
Gain	6 dB	8.7 dB	6.1 dB

de faisceaux proposée avec les travaux précédemment rapportés. En comparaison avec les autres travaux utilisant des diodes, cette antenne n'a pas de pertes dues aux circuits de polarisation et aux composants associés.

Une AD à commutation de faisceau basée sur une SSF activé en cantilever à 30 GHz a été proposée. Une SSF activée en cantilever a été conçue à 30 GHz en tant qu'élément actif pour la commutation par faisceau et ses coefficients de transmission ont été étudiés. Pour la validation des résultats, les panneaux du SSF proposé ont été fabriqués et mesurés pour obtenir une bonne isolation entre les états HAUT et BAS de la SSF. De plus, en mettant en œuvre les panneaux SSF autour d'une AD cylindrique, le balayage de tous les angles dans le plan d'azimut en six étapes a été réalisé. De plus, une configuration à deux faisceaux a également été analysée. Afin de valider le concept, un prototype d'AD à commutation de faisceaux a été fabriqués et ses diagrammes de rayonnement dans le plan azimutal ont été mesurés et ont montrée un bon accord avec les diagrammes simulés.

9.5 Antenne de commutation de faisceau à double plan

Dans cette section, une antenne à résonateur diélectrique à balayage à faisceau double plan utilisant des surfaces sélectives en fréquence activées en cantilever est présentée. L'antenne proposée est constituée d'un AD cylindrique et d'une SSF active ayant une forme hexagonale fonctionnant sur une bande de fréquence de 30 GHz. Initialement, la SSF reconfigurable utilisant des poutres en cantilever est conçue et analysée. De plus, un prototype de l'antenne proposée avec la SSF est conçu, fabriqué et mesuré. Le balayage de faisceau est obtenu dans les plans d'azimut et d'élévation de l'antenne. Le plan d'azimut entièrement est couvert par les faisceaux commutés en six étapes d'un angle de 60°. Dans le plan d'élévation, deux positions d'angles sont obtenues à 90° et 30°. Un gain d'antenne mesuré de 8,1 dB est obtenu.

9.5.1 Mécanisme de balayage du faisceau

Dans les travaux précédents rapportés dans [15, 16, 22], la plupart des balayages de faisceau ont été concentrés sur le plan azimutal de l'antenne. Dans ces travaux, le diagramme de rayonnement d'une source omnidirectionnelle est balayé à l'aide d'un écran SSF reconfigurable. Le seul travail signalé dans la commutation du plan d'élévation est dans la référence [30], où l'antenne source utilisée est un réseau d'alimentation à deux ports. Dans ce travail proposé, nous avons obtenu un plan d'inclinaison de faisceau en même temps que le balayage de faisceau dans le plan d'azimut, obtenant ainsi une nouvelle antenne à balayage de faisceau à double plan en utilisant une seule source. Pour le balayage du faisceau dans le plan azimutal, les panneaux SSF sont divisés en six sections comme dans les travaux précédents. De même, le balayage du plan d'élévation est obtenu par la division des panneaux SSF en deux hémisphères, supérieur et inférieur. Ainsi, deux balayages azimutaux sont obtenus dans les deux hémisphères d'angles d'élévation comme le montre la Figure 9.17. Lorsque le nombre de cellules unitaires augmente dans le panneau vertical, nous pouvons obtenir plus d'angles d'inclinaison dans le plan d'élévation.

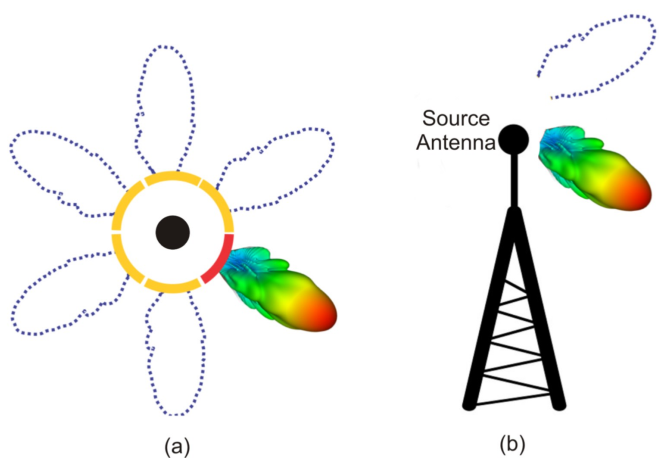

Figure 9.17 – Schéma du mécanisme de balayage du faisceau (a) Plan azimutal (b) Plan d'élévation

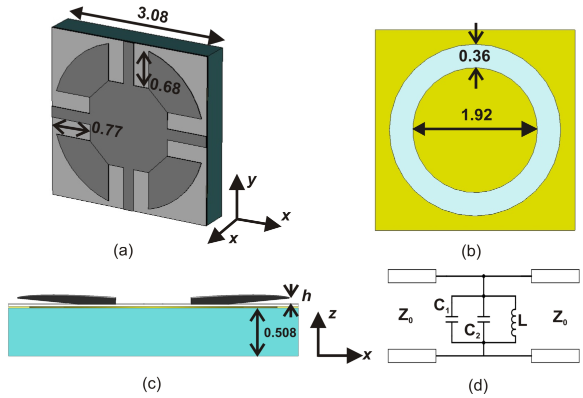

Figure 9.18 – Schéma de la SSF proposée (a) Vue en perspective (b) Couche de cuivre inférieure (c) Vue de côté

9.5.2 Conception de cellules unitaires SSF

La cellule unitaire SSF proposée est une structure à quatre couches activée en cantilever comme représenté à la Figure 9.18. La couche supérieure se compose des cantilevers actifs en forme de hache avec les lignes de connexion découpées dans un matériau en acier inoxydable. La couche de base consiste en une fente circulaire gravée sur un substrat RO6002. Les deux couches métalliques sont isolées par une fine couche de colle époxy-résine.

A partir du circuit équivalent comme montré à la Figure. 9.18 (d), la fréquence de résonance de la SSF peut être obtenue comme:

$$f_r = \frac{1}{2\pi\sqrt{L_1(C_1 + C_2)}} \tag{9.2}$$

où L_1 est l'inductance équivalente due aux couches métalliques, C_2 est la capacitance équivalente de la fente sur la couche de masse et C_1 est la capacitance de couplage entre les bras en cantilever et la couche de base, avec des valeurs optimisées comme $L_1 = 7.541$, $C_2 = 3,5\ pF$ et $C_1 = 0,25\ pF$. Le principe de fonctionnement de la SSF proposée dépend principalement de la couche en cantilever du SSF. La fente circulaire sur le plan de masse, qui est une structure de résonance, est chargée par les bras en cantilever de la couche supérieure en acier inoxydable. En ajustant la hauteur de la flexion des bras en cantilever, la capacité entre les couches supérieure et inférieure est modifiée et ainsi la fréquence de résonance de la fente circulaire peut être modifiée. Lorsque la hauteur de la poutre en cantilever est modifiée, la capacité de couplage C_1 varie, c'est-à-dire qu'elles sont inversement proportionnelles entre elles. La simulation EM de la cellule unitaire proposée est

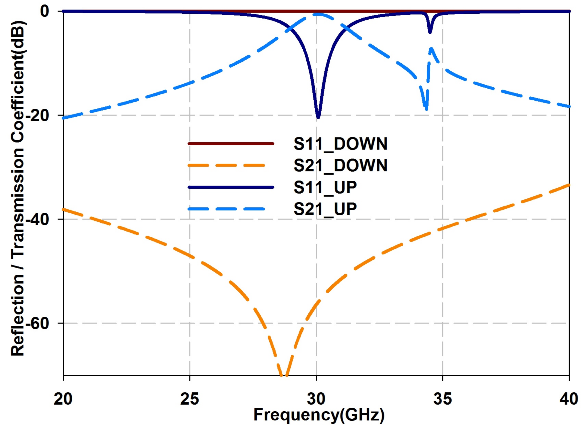

Figure 9.19 – Coefficients simulés de transmission et de réflexion d'une cellule unitaire du SSF

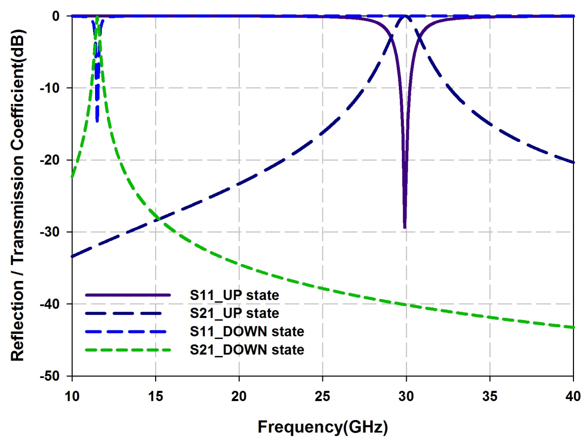

Figure 9.20 – Coefficients simulés de transmission et de réflexion d'une cellule unitaire SSF, analyse de circuit équivalent

réalisée en utilisant le logiciel CST Microwave studio, où des ports de floquet sont assignés des deux côtés de la cellule unitaire pour l'analyse. Les coefficients de transmission de la cellule unitaire sont représentés à la Figure. 9.19. Lorsque la hauteur des bras en cantilever varie, la fréquence de résonance de la cellule unitaire varie également. La hauteur optimisée des bras cantilever pour la résonance à 30 GHz est de $h = 0.1\ mm$. Ainsi, les deux états de fonctionnement de la cellule unitaire sont confirmés à $h = 0\ mm$ et $h = 0,1\ mm$ comme état BAS et HAUT, respectivement. À noter que l'isolation entre les états HAUT et BAS est supérieure à -50 dB à la fréquence de résonance. Le circuit équivalent est analysé, et les paramètres de diffusion pour les états HAUT et BAS sont représentés à la Figure. 9.20. On conclut que la valeur de la capacité de couplage C_1 de l'état HAUT à l'état BAS varie de $C_1 = 0,25\ pF$ à $C_1 = 21,8\ pF$.

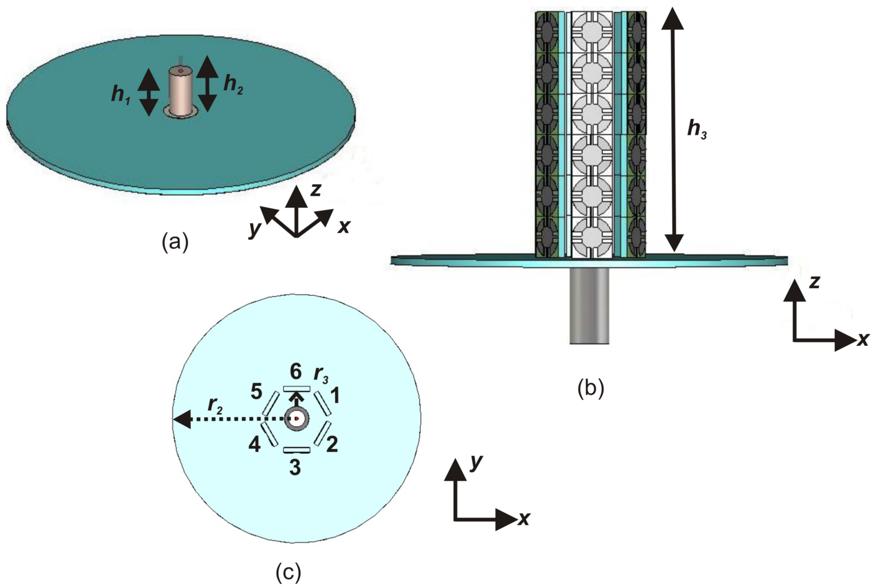

Figure 9.21 – Schéma de l'antenne de balayage de faisceau (a) AD seule, (b) AD avec SSF vue latérale (c) AD avec SSF vue de dessus

9.5.3 Conception d'antenne à commutation de faisceaux

Le schéma de l'antenne de commutation de faisceau proposée est représenté à la Figure 9.21. Elle se compose d'une source rayonnante et de panneaux SSF disposés en hexagonale autour de la source. La source rayonnante est une AD cylindrique conventionnelle avec un plan de masse circulaire et alimentée par une alimentation coaxiale. La AD agit comme une source monopolaire conventionnelle, où le mode TM_{01} a été excité par une sonde coaxiale et possédé un diagramme de rayonnement omnidirectionnel dans le plan azimutal et un diagramme directionnel dans le plan d'élévation.

En outre, les six panneaux du réseau 1×6 du SSF proposé sont disposés autour de la AD d'une manière hexagonale pour former une antenne à commutation du faisceau. Le rayon des panneaux SSF placés sur le plan de masse circulaire est optimisé pour obtenir un meilleur balayage du faisceau et est d'environ $r_3 = 0,45\lambda_0$, où λ_0 est la longueur d'onde à la fréquence de fonctionnement. Comme chaque panneau SSF est disposé de manière hexagonale, il incline un angle de 60° vers le centre. De plus, six cellules unitaires de la SSF sont utilisées verticalement, la hauteur totale de l'antenne, y compris la AD, étant de $h_3 = 18,9\ mm$.

Pour valider les résultats simulés, on a fabriqué et mesuré un prototype de l'antenne proposée, comme indiqué à la Figure 9.22. Les panneaux SSF sont gravés à l'aide de machine laser LPKF

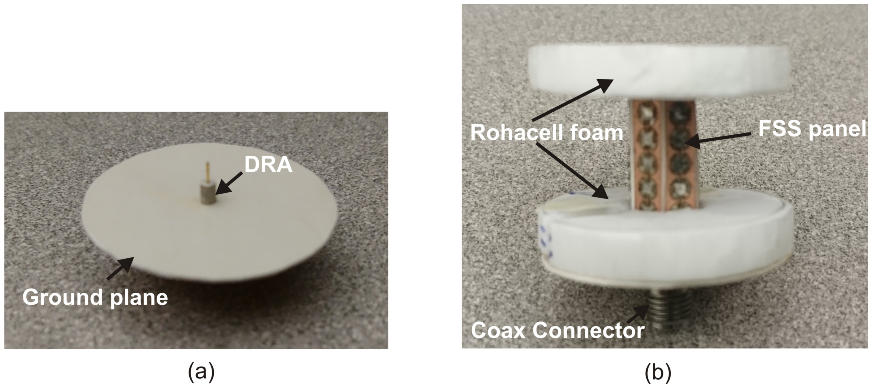

Figure 9.22 – Prototype fabriqué (a) AD seul (b) AD de commutation de faisceau

Protolaser. La couche de fond est gravée sur Rogers RT6002 d'épaisseur $t = 0,508\ mm$. De plus, la couche supérieure est gravée sur une cale en acier inoxydable de marque Précision d'une épaisseur de 0,013 mm. La flexion des bras en cantilever de cette couche est réalisée par un chauffage suffisant des bras de cantilever pour obtenir la hauteur optimisée h. La couche supérieure et la couche de base sont combinées à l'aide d'une colle époxy d'une épaisseur de 0,02 mm. Afin de prouver le concept de la SSF proposée, les panneaux d'état HAUT et BAS sont fabriqués séparément. Seulement dans la fabrication de cellules unitaires d'état HAUT, la flexion des bras en cantilever est effectuée. Mais dans la fabrication des cellules unitaires à états BAS, toute la couche supérieure est collée à la couche de base sans plier les bras.

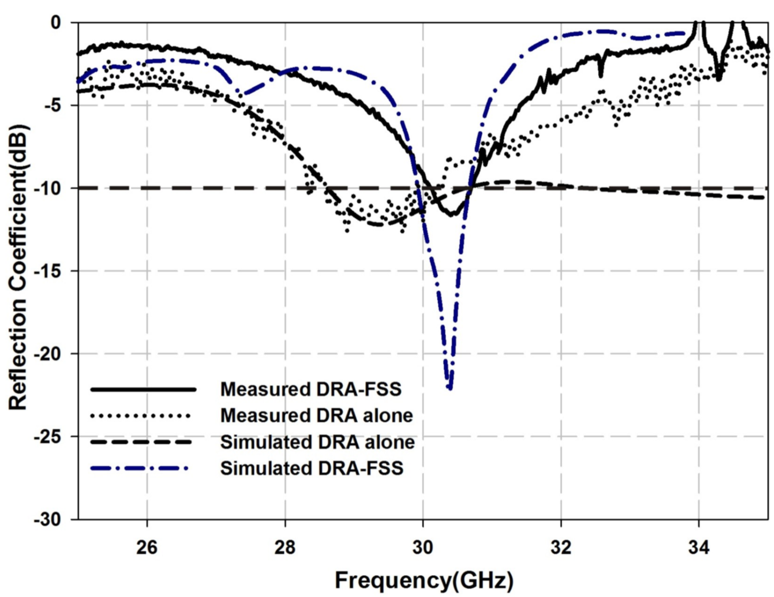

Figure 9.23 – Comparaison des coefficients de réflexion simulés et mesurés de la AD avec et sans les panneaux SSF

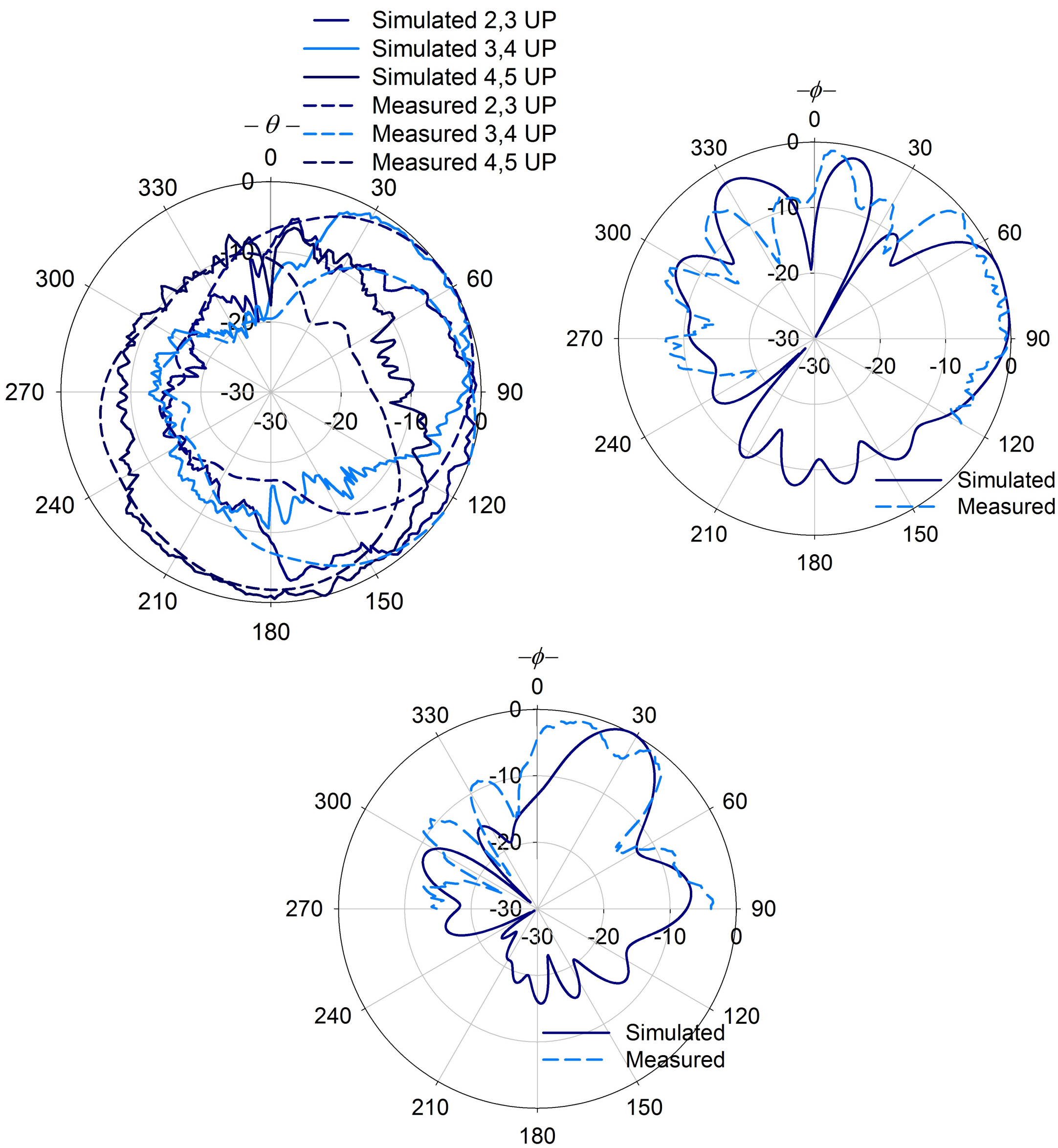

Figure 9.24 – Comparaison des diagrammes de rayonnement normalisés simulés et mesurés d'une antenne à commutation de faisceaux (a) Plan azimutal (b) Plan d'élévation(inférieur) (c) Plan d'élévation(supérieur)

Les coefficients de réflexion mesurés de la AD sans les panneaux SSF et l'antenne à balayage de faisceau sont représentés à la Figure 9.23, et comparés aux résultats simulés. De plus, le diagramme de rayonnement de l'antenne à balayage du faisceau a été mesuré pour chaque cas, et les résultats à 30 GHz sont représentés sur la Figure 9.24. Les modèles de plan d'azimut représentés à la Figure 9.24 (a), comparent les modèles mesurés aux diagrammes de rayonnement simulés à $\theta = 90°$ pour ces trois cas avec l'hémisphère inférieur dans l'état HAUT , pour obtenir un balayage avec une variation angulaire de 60°. À la Figure 9.24 (b) et (c), le plan d'élévation montre les faisceaux de commutation à $\phi = 0°$ et la comparaison des mesures avec les modèles de simulation. Il est évident que l'inclinaison de la poutre de 60° est obtenue en commutant les hémisphères inférieur et supérieur. Des largeurs de faisceau d'environ 46° et 85° sont obtenues dans le plan d'élévation et d'azimut, respectivement.

Une antenne à résonateur diélectrique à balayage de faisceau capable de balayer les faisceaux dans des plans d'élévation et d'azimut a été présentée. Les panneaux SSF reconfigurables activés en cantilever ont été utilisés comme écran actif pour le balayage de faisceau. L'antenne proposée avec le SSF a été conçue et fabriquée et mesurée à 30 GHz. Dans le plan d'élévation, on a obtenu deux angles de balayage à 30° et 90°. De même, dans le plan azimutal, six angles couvrent l'ensemble de 360°. Par rapport à la source omnidirectionnelle AD, une augmentation de gain de 6 dB a été observée. Avec ces caractéristiques, cette antenne peut être un bon candidat pour les communications sous fié en ondes millimétriques.

9.6 Conclusion

Dans cette thèse, de nouvelles surfaces sélectives en fréquence et leurs applications dans des antennes reconfigurables ont été étudiées. L'objectif principal du travail est de concevoir une nouvelle surface sélective en fréquence pour les antennes à commutation de faisceau opérant dans les bandes de fréquences à ondes millimétriques. Comme premier travail sur les SSFs en ondes millimétriques, une SSF large bande pour les applications de blindage et MIMO a été conçue. De plus, la nouvelle SSF reconfigurable activée en cantilever a été conçue. En utilisant des conceptions en cantilever, des antennes à commutation de faisceaux à plan unique et à plan double ont été conçues pour des applications en ondes millimétriques. Pour la réalisation des objectifs mentionnés, une méthodologie de conception a été suivie dans cette thèse, qui est conclue comme suit.

Dans une première étape, une étude approfondie des surfaces sélectives en fréquence pour des applications en antennes modernes a été réalisée. Cela confirme la contribution des surfaces sélectives en fréquence reconfigurables pour des applications en ondes millimétriques. Pour commencer, une SSF à large bande avec des structures à double résonance pour les applications MIMO et de blindage a été conçue. En outre, cette structure SSF a été utilisée pour la réduction de couplage mutuel dans un système d'antennes MIMO. Les résultats obtenus ont fait de deux publications [68, 9].

À l'étape suivante, nous avons introduit une structure SSF reconfigurable utilisant des commutateurs en cantilever pour des applications en antenne. Comparé à d'autres types de commutateur utilisés dans les SSF, ce commutateur montre de meilleures performances et faisabilité pour la fabrication. Pour la validation des prototypes conçus de la SSF activée en cantilever en micro-ondes et en bande d'ondes millimétriques. Les méthodes de guide d'onde et d'espace libre ont été utilisées. Les résultats obtenus ont fait l'object de trois publications présentées dans [62, 69, 70].

Ensuite, deux types d'antennes à balayage de faisceau ont été conçus en utilisant la SSF mentionnée sur une bande d'ondes millimétriques. Une antenne à résonateur diélectrique à commutation de faisceaux utilisant un panneau SSF activé en cantilever de forme hexagonale a initialement été conçue pour la commutation du faisceau dans le plan d'azimut. La SSF activée par cantilever conçue pour cette antenne a été inspirée des structures *supershape*. Pour la validation de la conception proposée de la SSF activée par cantilever, un modèle conceptuel de commutation a été utilisé. Les résultats obtenus ont démontré que le faisceau de commutation dans le plan azimutal peut couvrir tout le plan azimutal avec 60°. Les résultats obtenus ont fait l'object d'une publication présentée dans [71].

Enfin, un nouveau type d'antenne reconfigurable avec balayage à double faisceau à l'aide de la SSF en cantilever a été présenté. Parallèlement au plan azimutal, la commutation du plan d'élévation a également été réalisée. Comparée aux SSFs précédents, l'utilisation de larges poutres en cantilever a permis une miniaturisation de la cellule unitaire et donc plus de cellules unitaires ont été utilisées horizontalement pour obtenir une commutation dans le plan d'élévation. Les résultats ont démontré que la flexibilité du balayage du faisceau dans le plan d'élévation, par rapport aux prototypes précédents, à rendu l'antenne plus réalisable. Les résultats obtenus ont fait l'object d'une publication présentée dans [72].

9.7 Axes des futures recherches

Le travail de recherche effectué dans cette thèse dans le cadre du cours de doctorat ouvre une nouvelle créneau dans le domaine des structures SSFs reconfigurables et leurs applications dans le domaine des antennes. Cependant, il est important de mentionner qu'il y a beaucoup d'autres recherches à explorer dans ce domaine qui laissent la place à de futures possibilités de recherche comme expliqué dans le paragraphe suivant.

Premièrement, différentes formes de SSF peuvent être explorées avec des commutateurs à cantilever pour obtenir des SSF ayant de meilleures caractéristiques de sélectioner des larges/étroites de bandes, avec une isolation élevée des propriétés de commutation des propriétés à faibles pertes. Par exemple, il existe diverses conceptions de textit supershaped qui peuvent être explorées pour diverses structures résonantes de tableaux périodiques. La réalisation de la commutation du SSF activé par faisceau en porte-à-faux avec une tension peut être possible en utilisant d'autres méthodes de fabrication telles que la technologie LTCC, qui peut aider à concevoir un SSF activé en porte-à-faux entièrement contrôlable. De plus, une antenne à commutation de faisceaux double/triple bande utilisant des commutateurs activés en cantilever à double/triple bande peut être réalisée comme mentionné dans [26, 74], avec des meilleures performances en termes de commutation de faisceaux. D'autre part, cette technologie de commutation en cantilever peut être utilisée dans des autres composants RF tels que les déphaseurs, les amplificateurs et les coupleurs en ondes millimétriques.

References

[1] S. V. Hum and H. Y. Xiong. Analysis and design of a differentially-fed frequency agile microstrip patch antenna. *IEEE Transactions on Antennas and Propagation*, 58(10):3122–3130, Oct 2010.

[2] K. R. Boyle and P. G. Steeneken. A five-band reconfigurable PIFA for mobile phones. *IEEE Transactions on Antennas and Propagation*, 55(11):3300–3309, Nov 2007.

[3] Bharathi Anantha, Lakshminarayana Merugu, and P.V.D. Somasekhar Rao. A novel single feed frequency and polarization reconfigurable microstrip patch antenna. *AEU - International Journal of Electronics and Communications*, 72:8 – 16, 2017.

[4] L. Zhang, Q. Wu, and T. A. Denidni. Electronically radiation pattern steerable antennas using active frequency selective surfaces. *IEEE Transactions on Antennas and Propagation*, 61(12):6000–6007, 2013.

[5] Mohammad Ababil Hossain, Israfil Bahceci, and Bedri A. Cetiner. Parasitic layer based radiation pattern reconfigurable antenna for 5g communications. *IEEE Transactions on Antennas and Propagation*, pages 1–1, 2017.

[6] Ben A. Munk. *Frequency Selective Surfaces*. John Wiley & Sons, Inc., 2005.

[7] J. H. Kim, H. J. Chun, I. P. Hong, Y. J. Kim, and Y. B. Park. Analysis of fss radomes based on physical optics method and ray tracing technique. *IEEE Antennas and Wireless Propagation Letters*, 13:868–871, 2014.

[8] B. Sanz-Izquierdo and E. A. Parker. 3d printed fss arrays for long wavelength applications. In *The 8th European Conference on Antennas and Propagation (EuCAP 2014)*, pages 2382–2386, April 2014.

[9] R. Karimian, A. Kesavan, M. Nedil, and T. A. Denidni. Low-mutual-coupling 60-ghz mimo antenna system with frequency selective surface wall. *IEEE Antennas and Wireless Propagation Letters*, 16:373–376, 2017.

[10] A. J. Fenn. *Adaptive Antennas and Phased Arrays for Radar and Communication Systems*. Artech House, 2008.

[11] J. T. Bernard. *Reconfigurable Antennas*. Morgan & Claypool publication series, 2007.

[12] J. C. Langer, J. Zou, C. Liu, and J. T. Bernhard. Micromachined reconfigurable out-of-plane microstrip patch antenna using plastic deformation magnetic actuation. *IEEE Microwave and Wireless Components Letters*, 13(3):120–122, March 2003.

[13] R. F. Harrington. Reactively controlled directive arrays. *IEEE Transactions on Antennas and Propagation*, 26(3):390–395, 1978.

[14] M. Niroo-Jazi and T. A. Denidni. Electronically sweeping-beam antenna using a new cylindrical frequency-selective surface. *IEEE Transactions on Antennas and Propagation*, 61(2):666–676, 2013.

[15] M. N. Jazi and T. A. Denidni. Frequency selective surfaces and their applications for nimble-radiation pattern antennas. *IEEE Transactions on Antennas and Propagation*, 58(7):2227–2237, 2010.

[16] A. Edalati and T. A. Denidni. Frequency selective surfaces for beam-switching applications. *IEEE Transactions on Antennas and Propagation*, 61(1):195–200, 2013.

[17] A. Edalati and T. A. Denidni. High-gain reconfigurable sectoral antenna using an active cylindrical FSS structure. *IEEE Transactions on Antennas and Propagation*, 59(7):2464–2472, 2011.

[18] Li Zhouyuan, E. Ahmed, A. M. Eltawil, and B. A. Cetiner. A beam-steering reconfigurable antenna for WLAN applications. *Antennas and Propagation, IEEE Transactions on*, 63(1):24–32, 2015.

[19] M. Safari, C. Shafai, and L. Shafai. X-band tunable frequency selective surface using MEMS capacitive loads. *IEEE Transactions on Antennas and Propagation*, 63(3):1014–1021, 2015.

[20] J Chang won, L Ming-jer, G. P. Li, and F. De Flaviis. Reconfigurable scan-beam single-arm spiral antenna integrated with RF-MEMS switches. *IEEE Transactions on Antennas and Propagation*, 54(2):455–463, 2006.

[21] M. Bouslama, M. Traii, T. A. Denidni, and A. Gharsallah. Reconfigurable frequency selective surface for beam-switching applications. *IET Microwaves, Antennas and Propagation*, 11(1):69–74, 2017.

[22] L. Bin, B. Sanz-Izquierdo, E. A. Parker, and J. C. Batchelor. Cylindrical slot FSS configuration for beam-switching applications. *IEEE Transactions on Antennas and Propagation*, 63(1):166–173, 2015.

[23] S. M. Mahmood and T. A. Denidni. Pattern-reconfigurable antenna using a switchable frequency selective surface with improved bandwidth. *IEEE Antennas and Wireless Propagation Letters*, 15:1148–1151, 2016.

[24] J. Li, Q. Zeng, R. Liu, and T. A. Denidni. A compact dual-band beam-sweeping antenna based on active frequency selective surfaces. *IEEE Transactions on Antennas and Propagation*, 65(4):1542–1549, 2017.

[25] C. Gu, B. S. Izquierdo, S. Gao, J. C. Batchelor, E. A. Parker, F. Qin, G. Wei, J. Li, and J. Xu. Dual-band electronically beam-switched antenna using slot active frequency selective surface. *IEEE Transactions on Antennas and Propagation*, 65(3):1393–1398, March 2017.

[26] J. Li, Q. Zeng, R. Liu, and T. A. Denidni. A gain enhancement and flexible control of beam numbers antenna based on frequency selective surfaces. *IEEE Access*, 6:6082–6091, 2018.

[27] Ilkyu Kim and Yahya Rahmat-Samii. Electromagnetic band gap-dipole sub-array antennas creating an enhanced tilted beams for future base station. *IET Microwaves, Antennas and Propagation*, 9(4):319–327, 2015.

[28] A. Dadgarpour, B. Zarghooni, B. S. Virdee, and T. A. Denidni. One- and two-dimensional beam-switching antenna for millimeter-wave mimo applications. *IEEE Transactions on Antennas and Propagation*, 64(2):564–573, 2016.

[29] M. Mantash, A. Kesavan, and T. A. Denidni. Beam-tilting endfire antenna using a single-layer fss for 5g communication networks. *IEEE Antennas and Wireless Propagation Letters*, 17(1):29–33, 2018.

[30] Chao Gu, Steven Gao, B. Sanz-Izquierdo, Edward A. Parker, Fan Qin, Hang Xu, John C. Batchelor, Xuexia Yang, and Zhiqun Cheng. 3d-coverage beam-scanning antenna using feed array and active frequency selective surface. *IEEE Transactions on Antennas and Propagation*, 65(11):5862–5870, 2017.

[31] John L. Volakis. *Antenna Engineering Handbook,*, page (Chapter 56: Frequency Selective Surfaces). McGraw-Hill, 2008.

[32] E. A. Parker C. Antonopoulos, R. Cahill and I. M. Sturland. Multilayer frequency-selective surfaces for millimetre and submillimetre wave applications. *IEE Proc. on Mic., Ant. and Propag.*, 144(6):415–420, 1997.

[33] P. Callaghan and E. A. Parker. Tuning interactions of cascaded-frequency selective-slot arrays. *IEE Proc. on Mic., Ant. and Propag.*, 141(4):290–294, 1994.

[34] R. Luebbers and B. Munk. Some effects of dielectric loading on periodic slot arrays. *IEEE Trans. on Ant. Propag*, 26(4):536–542, 1976.

[35] Xiaoxiang H. Boyu H., Xiaochun L. and Yang Y. Wide-angle frequency selective surface with ultra-wideband response for aircraft stealth designs. *Progress In Electromagnetics Research C*, 77:167–173, 2017.

[36] M. Nauman, R. Saleem, A. K. Rashid, and M. F. Shafique. A miniaturized flexible frequency selective surface for x-band applications. *IEEE Transactions on Electromagnetic Compatibility*, 58(2):419–428, April 2016.

[37] F. Huang, C. Chiu, T. Wu, and Y. Chiou. Very closely located dual-band frequency selective surfaces via identical resonant elements. *IEEE Antennas and Wireless Propagation Letters*, 14:414–417, 2015.

[38] Ramprabhu Sivasamy, Balaji Moorthy, Malathi Kanagasabai, Jithila V. George, Livya Lawrance, and Dinesh Babu Rajendran. Polarization-independent single-layer ultra-wideband frequency-selective surface. *International Journal of Microwave and Wireless Technologies*, pages 1–5, 2015.

[39] M. L. Abdelghani, H. Attia, and T. A. Denidni. Dual- and wideband fabry–pérot resonator antenna for wlan applications. *IEEE Antennas and Wireless Propagation Letters*, 16:473–476, 2017.

[40] H. Attia, M. L. Abdelghani, and T. A. Denidni. Wideband and high-gain millimeter-wave antenna based on fss fabry–perot cavity. *IEEE Transactions on Antennas and Propagation*, 65(10):5589–5594, Oct 2017.

[41] M. Akbari, S. Gupta, M. Farahani, A. R. Sebak, and T. A. Denidni. Gain enhancement of circularly polarized dielectric resonator antenna based on fss superstrate for mmw applications. *IEEE Transactions on Antennas and Propagation*, 64(12):5542–5546, 2016.

[42] A. A. Omar and Z. Shen. Thin 3-d bandpass frequency-selective structure based on folded substrate for conformal radome applications. *IEEE Transactions on Antennas and Propagation*, 67(1):282–290, Jan 2019.

[43] D. Sievenpiper, Lijun Zhang, R. F. J. Broas, N. G. Alexopolous, and E. Yablonovitch. High-impedance electromagnetic surfaces with a forbidden frequency band. *IEEE Transactions on Microwave Theory and Techniques*, 47(11):2059–2074, Nov 1999.

[44] D. Seetharamdoo, M. Berbineau, A. C. Tarot, and K. Mahdjoubi. Evaluating the potential shielding properties of periodic metamaterial slabs. pages 1–4, June 2009.

[45] I. S. Syed, Y. Ranga, L. Matekovits, K. P. Esselle, and S. G. Hay. A single-layer frequency-selective surface for ultrawideband electromagnetic shielding. *Electromagnetic Compatibility, IEEE Transactions on*, 56(6):1404–1411, 2014.

[46] H. Y. Chen and Y. K. Chou. An emi shielding fss for ku-band applications. In *Proceedings of the 2012 IEEE International Symposium on Antennas and Propagation*, pages 1–2, July 2012.

[47] F. C. G. da Silva Segundo, A. L. P. S. Campos, and E. C. Braz. Wide band frequency selective surface for angular and polarization independent operation. *Microwave and Optical Technology Letters*, 57(1):216–219, 2015.

[48] Z P Wu, De M Cheng, W J Ma, J W Hu, Y H Yin, Y Y Hu, Y S Li, J G Yang, and Q F Xu. Electromagnetic interference shielding effectiveness of composite carbon nanotube macro-film at a high frequency range of 40 ghz to 60 ghz. *AIP Advances*, 5(6):067130, 2015.

[49] R. Sivasamy and M. Kanagasabai. A novel dual-band angular independent fss with closely spaced frequency response. *Microwave and Wireless Components Letters, IEEE*, 25(5):298–300, 2015.

[50] S. Narayan, S B. Joshi, R U. Nair, and R M Jha. Electromagnetic performance analysis of novel multi-band metamaterial fss for millimeter wave radome applications. *Comput.Mater.Continua*, 31(1):1–15, 2012.

[51] N. Liu, X. Sheng, C. Zhang, J. Fan, and D. Guo. A design method for synthesizing wideband band-stop fss via its equivalent circuit model. *IEEE Antennas and Wireless Propagation Letters*, 16:2721–2725, 2017.

[52] Maryam R. Ali A. and Hamid R. Ultra-thin tunable plasma-metasurface composites for extremely broadband electromagnetic shielding applications. *Progress In Electromagnetics Research C*, 85:91–104, 2018.

[53] Malay R. Tripathy Sarika and Daniel R. A wideband frequency selective surface reflector for 4g/x-band/ku-band. *Progress In Electromagnetics Research C*, 81:151–159, 2018.

[54] Y. E. Erdemli, K. Sertel, R. A. Gilbert, D. E. Wright, and J. L. Volakis. Frequency-selective surfaces to enhance performance of broad-band reconfigurable arrays. *IEEE Transactions on Antennas and Propagation*, 50(12):1716–1724, Dec 2002.

[55] CST, Darmstadt, Germany . CST microwave studio 2013.

[56] S. Celozzi and G. Araneo, R. Lovat. *Electromagnetic Shielding*. Wiley-IEEE Press., 2008.

[57] L. B. Wang, K. Y. See, J. W. Zhang, B. Salam, and A. C. W. Lu. Ultrathin and flexible screen-printed metasurfaces for emi shielding applications. *IEEE Transactions on Electromagnetic Compatibility*, 53(3):700–705, Aug 2011.

[58] D. Robben, S. F. Peik, T. Henning, M. Becker, and K. Froehner. Laser machined microsystems for active frequency selective surfaces. In *Microwave Symposium Digest (MTT), 2012 IEEE MTT-S International*, pages 1–3.

[59] F. Bayatpur and K. Sarabandi. Tuning performance of metamaterial-based frequency selective surfaces. *IEEE Transactions on Antennas and Propagation*, 57(2):590–592, Feb 2009.

[60] S. A. Winkler, H. Wei, M. Bozzi, and W. Ke. Polarization rotating frequency selective surface based on substrate integrated waveguide technology. *Antennas and Propagation, IEEE Transactions on*, 58(4):1202–1213, 2010.

[61] T. S. Rappaport, S. Sun, R. Mayzus, H. Zhao, Y. Azar, K. Wang, G. N. Wong, J. K. Schulz, M. Samimi, and F. Gutierrez. Millimeter wave mobile communications for 5g cellular: It will work! *IEEE Access*, 1:335–349, 2013.

[62] A. Kesavan, B. P. Chacko, and T. A. Denidni. Active frequency selective surfaces using cantilever switches for 60-GHz applications. In *Antennas and Propagation and USNC/URSI National Radio Science Meeting, 2015 IEEE International Symposium on*, pages 882–883.

[63] B. P. Chacko, G. Augustin, and T. A. Denidni. Millimeter-wave active FSS structure with catilever switches for beam-switching antenna applications. In *Antennas and Propagation and USNC/URSI National Radio Science Meeting, 2015 IEEE International Symposium on*, pages 886–887.

[64] J. Gielis. A generic geometric transformation that unifies a wide range of natural and abstract shapes. *American Journal of Botany*, 90:333–338, 2003.

[65] A. Edalati and T. A. Denidni. High-gain reconfigurable sectoral antenna using an active cylindrical fss structure. *Antennas and Propagation, IEEE Transactions on*, 59(7):2464–2472, 2011.

[66] W. Pan, C. Huang, P. Chen, M. Pu, X. Ma, and X. Luo. A beam steering horn antenna using active frequency selective surface. *IEEE Transactions on Antennas and Propagation*, 61(12):6218–6223, Dec 2013.

[67] A. Chatterjee and S. K. Parui. Frequency-dependent directive radiation of monopole-dielectric resonator antenna using a conformal frequency selective surface. *IEEE Transactions on Antennas and Propagation*, 65(5):2233–2239, May 2017.

[68] A. Kesavan, R. Karimian, and T. A. Denidni. A novel wideband frequency selective surface for millimeter-wave applications. *IEEE Antennas and Wireless Propagation Letters*, 15:1711–1714, 2016.

[69] B. P. Chacko, G. Augustin, A. Kesavan, and T. A. Denidni. Pattern-reconfigurable antenna using cantilever based-afss. In *2016 17th International Symposium on Antenna Technology and Applied Electromagnetics (ANTEM)*, pages 1–2.

[70] A. Kesavan, B. P. Chacko, and T. A. Denidni. Beam-tilting vivaldi antenna using cantilever based-frequency selective surfaces. In *2016 IEEE International Symposium on Antennas and Propagation (APSURSI)*, pages 961–962.

[71] A. Kesavan, M. Mantash, and T. A. Denidni. Beam-switching millimeter-wave antenna using cantilever based frequency selective surfaces. *IET Microwaves, Antennas Propagation*, 12(13):2019–2024, June 2018.

[72] A. Kesavan, M. Mantash, J. Zaid, and T. A. Denidni. A dual-plane beam-sweeping millimeter-wave antenna using reconfigurable frequency selective surfaces. *IEEE Antennas and Wireless Propagation Letters*, 17(10):1832–1836, Aug 2018.

[73] A. Kesavan, M. Mantash, J. Zaid, and T. A. Denidni. Millimeter-wave dual-plane beam-switching antenna based on cantilever enabled fss. In *2018 IEEE International Symposium on Antennas and Propagation USNC/URSI National Radio Science Meeting*, pages 293–294, July 2018.

[74] C. Gu, B. S. Izquierdo, S. Gao, J. C. Batchelor, E. A. Parker, F. Qin, G. Wei, J. Li, and J. Xu. Dual-band electronically beam-switched antenna using slot active frequency selective surface. *IEEE Transactions on Antennas and Propagation*, 65(3):1393–1398, 2017.